

# Numerical Investigations of Geologic CO<sub>2</sub> Sequestration Using Physics-Based and Machine Learning Modeling Strategies

Hao Wu

Dissertation submitted to the faculty of the Virginia Polytechnic  
Institute and State University in partial fulfillment of the requirements  
for the degree of

Doctor of Philosophy

In

Geosciences

Ryan M. Pollyea, Chair

Thomas J. Burbey

Benjamin C. Gill

Nicholas E. Lubbers

Madeline E. Schreiber

July 20, 2020  
Blacksburg, Virginia

Keywords: CO<sub>2</sub> sequestration, capillary pressure, relative permeability,  
reactive transport, machine learning

Copyright 2020, Hao Wu

# Numerical Investigations of Geologic CO<sub>2</sub> Sequestration Using Physics-based and Machine Learning Modeling Strategies

Hao Wu

## ABSTRACT

Carbon capture and sequestration (CCS) is an engineering-based approach for mitigating excess anthropogenic CO<sub>2</sub> emissions. Deep brine aquifers and basalt reservoirs have shown outstanding performance in CO<sub>2</sub> storage based on their global widespread distribution and large storage capacity. Capillary trapping and mineral trapping are the two dominant mechanisms controlling the distribution, migration, and transportation of CO<sub>2</sub> in deep brine aquifers and basalt reservoirs. Understanding the behavior of CO<sub>2</sub> in a storage reservoir under realistic conditions is important for risk management and storage efficiency improvement. As a result, numerical simulations have been implemented to understand the relationship between fluid properties and multi-phase fluid dynamics. However, the physics-based simulations that focus on the uncertainties of fluid flow dynamics are complicated and computationally expensive. Machine learning method provides immense potential for improving computational efficiency for subsurface simulations, particularly in the context of parametric sensitivity. This work focuses on parametric uncertainty associated with multi-phase fluid dynamics that govern geologic CO<sub>2</sub> storage. The effects of this uncertainty are interrogated through ensemble simulation methods that implement both physics-based and machine learning modeling strategies. This dissertation is a culmination of three projects: (1) a parametric analysis of capillary pressure variability effects on CO<sub>2</sub> migration, (2) a reactive transport simulation in a basalt fracture system investigating the effects of carbon mineralization on CO<sub>2</sub> migration, and (3) a parametric analysis based on machine learning methods of simultaneous effects of capillary pressure and relative permeability on CO<sub>2</sub> migration.

# Numerical Investigations of Geologic CO<sub>2</sub> Sequestration Using Physics-based and Machine Learning Modeling Strategies

Hao Wu

## GENERAL AUDIENCE ABSTRACT

Carbon capture and sequestration (CCS) has been proposed as a technological approach to mitigate the deleterious effects of anthropogenic CO<sub>2</sub> emissions. During CCS, CO<sub>2</sub> is captured from power plants and then pumped in deep geologic reservoirs to isolate it from the atmosphere. Deep sedimentary formations and fractured basalt reservoirs are two options for CO<sub>2</sub> storage. In sedimentary systems, CO<sub>2</sub> is immobilized largely by physical processes, such as capillary and solubility trapping, while in basalt reservoirs, CO<sub>2</sub> is transformed into carbonate minerals, thus rendering it fully immobilized. This research focuses on how a large range of capillary pressure variabilities and how CO<sub>2</sub>-basalt reactions affect CO<sub>2</sub> migration. Specifically, the work presented utilizes numerical simulation and machine learning methods to study the relationship between capillary trapping and buoyancy in a sandstone formation, as well as the combined effects of capillary pressure and relative permeability on CO<sub>2</sub> migration. In addition, the work also identifies a new reinforcing feedback between mineralization and relative permeability during reactive CO<sub>2</sub> flow in a basalt fracture network. In aggregate, the whole of this work presents a new, multi-dimensional perspective on the multi-phase fluid dynamics that govern CCS efficacy in a range of geologic formations.

# Dedication

*I could not have done this without the support of my wonderful parents. Their encouragement and support over the last seven years have been unparalleled and unyielded. They cheered my every achievement and they encouraged my every frustration. Mom and dad, I could not do this without you two.*

*I've really enjoyed my time here at Virginia Tech working towards my Ph.D. and it is all because of the people that have helped and supported me. This Ph.D. journey is definitely a highlight of my life.*

# Acknowledgments

First, I would like to thank my advisor Ryan Pollyea for his guidance, encouragement, and support from the very beginning. It is because of his advising and mentorship during my graduate career that made all of this possible. Thank you to my committee members Tom Burbey, Maddy Schreiber, Ben Gill, and Nick Lubbers for giving your time and expertise. Also, I would like to thank my mentor from Los Alamos National Lab, Nick Lubbers and Hari Visvanathan, for mentorship during my internship and the following support for my research. In addition, I want to show my appreciation to two passed away Professors Bob Lowell, and Don Rimstidt for their special support during my Ph.D. career and honor the memory of them. I'd like to thank the Virginia Tech Geosciences Department for graduate student support through teaching and research assistantships throughout my Ph.D.

This work received financial support from the Virginia Tech Geosciences Department, the Graduate Student Assembly at Virginia Tech, and the U.S. Department of Energy.

# Contents

List of Figures .....	viii
List of Tables .....	x
1 Introduction .....	1
2 A parametric analysis of capillary pressure effect .....	6
2.1 Introduction .....	6
2.2 Conceptual Model and Methods .....	11
2.3 Results .....	16
2.4 Discussion .....	17
2.4.1 Carbon Dioxide Plume Geometry .....	17
2.4.2 Vertical CO <sub>2</sub> Flow .....	19
2.4.3 Buoyancy versus Capillary Force .....	21
2.4.3.1 Quantifying Buoyancy Characteristics .....	21
2.4.3.2 Balance of Buoyancy and Capillarity .....	22
2.4.3.3 Effects of Parametric Variability .....	24
2.5 Conclusion .....	26
3 Modeling CO <sub>2</sub> -Water-Basalt Reactions in a Basalt Fracture Network .....	28
3.1 Introduction .....	28
3.2 Fluid-Rock Geochemical Reactions for CO <sub>2</sub> -Water-Basalt .....	32
3.3 Methods .....	33
3.3.1 Conceptual Model .....	33
3.3.2 Domain and Boundary Conditions .....	35
3.3.3 Reactive Transport .....	38
3.3.4 Permeability Alteration .....	40
3.4 Results and Discussion .....	42
3.4.1 Mineral Precipitation and Fracture Permeability Change .....	42

3.4.2 Spatial and Temporal Fracture Permeability Alteration .....	47
3.4.3 Mass Balance .....	50
3.5 Conclusion .....	53
4 Machine Learning Applied to Parametric Analysis of CO <sub>2</sub> Migration .....	55
4.1 Introduction .....	55
4.2 Methods .....	60
4.2.1 Physical Model.....	61
4.2.2 Artificial Neuron Networks (ANN).....	65
4.3 Results & Discussion .....	70
4.3.1 Overall Efficiency .....	70
4.3.2 Parametric Analysis of 3-D Parameter Space .....	75
4.3.3 Applications of ML Methods in CCS .....	79
4.5 Conclusion .....	80
5 Conclusion .....	82
Bibliography .....	84
Appendices .....	101
Appendix A .....	102
Appendix B .....	104

# List of Figures

- 2.1 Experimental capillary pressure measurements
- 2.2 Two-dimensional symmetric model domain
- 2.3 Capillary pressure parameters
- 2.4 Relative permeability ( $k_{rel}$ ) model
- 2.5 Gas phase CO<sub>2</sub> saturation after 10 years injection
- 2.6 Vertical to horizontal flow ratio (VHF) of supercritical CO<sub>2</sub>
- 2.7 Log  $\omega$  for five parameter combinations
- 2.8 Response surface for  $\bar{\omega}$  for 189 simulations
  
- 3.1 Monte Carlo simulation results of CO<sub>2</sub> saturation
- 3.2 Conceptual model of gas-phase CO<sub>2</sub> flow in a branching fracture
- 3.3 Research domain of a basalt fracture system
- 3.4 Different types of mineral precipitation inside the fracture system
- 3.5 CO<sub>2</sub> saturation and volume fraction of mineral precipitation
- 3.6 Permeability change within the fracture
- 3.7 CO<sub>2</sub> saturation and gas-phase CO<sub>2</sub> Darcy velocity along the fracture
- 3.8 Time series of fracture permeability change
  
- 4.1 Reservoir domain
- 4.2 Artificial Neuron Network structure
- 4.3 Workflow of Artificial Neuron Network model
- 4.4 Parameters distribution
- 4.5 Prediction results for CO<sub>2</sub> saturation and pressure perturbation

4.6 Evaluation of prediction results across the reservoir

4.7 3-D parameter space and isosurface of 1% CO<sub>2</sub> saturation

4.8 3-D parameter space and isosurface of 0.5 MPa pressure perturbation

A.1 Volume fraction of mineral precipitation

B.1 Prediction results for CO<sub>2</sub> saturation

B.2 Prediction results for pressure perturbation

# List of Tables

2.1 Bulk reservoir properties

3.1 Bulk reservoir properties

3.2 Parameters for rate equation

3.3 Minerals precipitation

3.4 Mass balance of different phases of CO<sub>2</sub>

4.1 Bulk reservoir properties

# Chapter 1

## Introduction

Anthropogenic CO<sub>2</sub> emissions have been implicated in increasing global temperatures, the result of which is causing numerous environmental issues, such as sea level rise. The emission of CO<sub>2</sub> due to fossil fuel combustion is the dominant cause of high atmospheric CO<sub>2</sub> concentration during the 21<sup>st</sup> century (Metz et al., 2005). As the global economy continues growing, the fossil fuel combustion is continuously increasing as well, e.g., the number of fossil-fueled power plants for electricity generation is increasing. As a result, the concentration of carbon dioxide in the atmosphere reached 860 GtC (Gigatonnes of carbon) in 2017 (Le Quéré et al., 2018; Dlugokencky and Tans, 2018). The reduction of CO<sub>2</sub> emission is an essential goal that has to be achieved on the basis of legal and regulatory issues, environmental impacts, and safety issues (Metz et al., 2005). One of the promising technological solutions is carbon capture and sequestration (CCS), which is the process of capturing CO<sub>2</sub> from point source generator and then injecting it into deep geological formations (> 800 m) for long-term storage (Bennion and Bachu, 2005; Metz et al., 2005; Matter and Kelemen, 2009). The injected CO<sub>2</sub> in deep geological reservoirs located at depth > 800 m exists in supercritical phase, which maximizes CO<sub>2</sub> density to increasing the transport and storage efficiency (Bachu 2000; van der Meer 1992). The efficiency of a CCS project depends on whether or not the injected CO<sub>2</sub> remains isolated within the storage reservoir over timescales exceeding 10<sup>4</sup> years (Shaffer, 2010; Metz et al., 2005).

Deep brine aquifers, depleted oil/gas reservoirs, and coal beds have been recognized as the CO<sub>2</sub> storage reservoirs, while deep brine aquifers have been extensively studied as they have widespread global distributions and large storage capacity (Metz et al., 2005; Shi et al., 2011; Krause et al., 2011; Michael et al., 2010; Iglauer et al., 2011). Within the storage reservoir, four different mechanisms are known to isolate CO<sub>2</sub>: structural trapping, capillary trapping, solubility trapping, and mineral trapping (Iglauer et al., 2011; Benson and Cole, 2008; Nicot, 2008). Structural trapping characterizes the mechanism that the overlying cap rock of the storage reservoir prevents the upward CO<sub>2</sub> flow driven by buoyance due to its low permeability (Benson and Cole, 2008; Hesse et al., 2008). Capillary trapping and solubility trapping are the mechanisms in deep brine aquifers to keep CO<sub>2</sub> trapped due to capillary pressure and CO<sub>2</sub> dissolution into the aqueous phase, respectively (Hesse et al., 2008; Hunt et al., 1988; Mito et al., 2008), while mineral trapping yields the potential for permanent CO<sub>2</sub> isolation resulting from the geochemical reactions between the CO<sub>2</sub>, formation fluids (i.e., brine), and the reservoir rock. During mineral trapping, chemical reactions result in the precipitation of the thermodynamically stable carbonate minerals (Mito et al., 2008; Bachu et al., 1994). For each trapping mechanism, the efficacy is strongly controlled by the physical reservoir properties and geological conditions, such as the fracture geometry, buoyancy, capillary pressure, and relative permeability. At the same time, the reservoir properties are affected by the injected CO<sub>2</sub>, as the precipitation of carbonate minerals of mineral trapping alters the porosity and permeability of storage formations. As a result, understanding the behavior of CO<sub>2</sub> in a storage reservoir under realistic conditions is important for risk management and storage efficiency estimation.

Numerous modeling studies have been completed to characterize the interactions between fluid properties and multi-phase fluid dynamics during CCS project assessment (Ferrand and Celia, 1992; Chaouche et al., 1994; Ataie-Ashtiani et al., 2002; Arns et al.,

2003). However, the physics-based simulations focus on uncertainties on CO<sub>2</sub> migration that are complicated and computationally expensive (Mudunuru et al., 2020). In recent years, machine learning (ML) has provided immense potential at efficient data analyses for high-fidelity, multi-dimensional datasets (Karpatne et al., 2019; Lary et al., 2016; Rouet-Leduc et al., 2017), and the application of ML indicates the good performance in improving computational efficiency for subsurface simulations (Maniar et al., 2018; Srinivasan et al., 2019). More importantly, the application of ML opens up huge opportunities for making highly accurate predictions of fluid migration under unknown physical conditions (Poulton, 2002).

This dissertation focuses on understanding how capillary trapping and mineral trapping mechanisms affect CO<sub>2</sub> injection at different scales within both sandstone and fractured basalt reservoirs. In addition, numerical modeling studies coupled with machine learning methods are utilized for analyzing the migration, transportation, and distribution of CO<sub>2</sub> to answer the following questions: (1) how does the wide range of laboratory-scale capillary pressure measurements affect CO<sub>2</sub> migration and plume geometry while considering the balance of buoyancy and capillary forces? (2) How does the relationship between fluid relative permeability effects and CO<sub>2</sub> mineralization affects the physics fluid migration system and fracture permeability alteration? And (3) How do feedbacks between the capillary pressure and relative permeability affect CO<sub>2</sub> migration and fluid pressure propagation during industrial-scale CCS operations? Answering these questions is essential to understanding the CO<sub>2</sub> trapping mechanisms required for successful CCS projects.

The first question is addressed in Chapter 2: How does the wide range of laboratory-scale capillary pressure measurements in sandstone core samples affect reservoir-scale CO<sub>2</sub> migration? To answer this question, an ensemble of simulations of 189 CO<sub>2</sub> injection models was developed for unique combinations of the parameters that control the van Genuchten capillary pressure model. The ensemble results are analyzed by developing a new dimensionless number,  $\omega$ , which

is a modified Bond number that defines the relationship between buoyancy pressure and capillary pressure. When  $\omega > 1$ , buoyancy governs the system and CO<sub>2</sub> plume geometry is governed by upward flow. In contrast, when  $\omega < 1$ , then buoyancy is smaller than capillary force and lateral flow governs CO<sub>2</sub> plume geometry. The results show that the  $\omega$  ratio is an easily implemented screening tool for qualitative assessment of CO<sub>2</sub> distribution characteristics.

Chapter 3 focuses on understanding the feedbacks between multi-phase fluid flow and geochemical mineralization reactions in basalt fractures. A reactive transport model was developed to simulate CO<sub>2</sub> infiltrating a meter-scale, synthetic basalt fracture network from below, e.g., CO<sub>2</sub> leakage from a basalt reservoir into an overlying, low-permeability flow interior. In this study, fracture permeability is coupled with changes of porosity due to mineral precipitation alteration and several different models are tested for increasingly nonlinear changes to permeability reduction. Results show that carbonate and clay minerals precipitate at branching fractures, where relative permeability effects decrease CO<sub>2</sub> mobility, thus increasing fluid residence time. Analyzing the carbon mass balance shows that stronger porosity-permeability coupling may cause basalt fracture networks to be self-sealing CO<sub>2</sub> storage reservoirs.

Chapter 4 analyzes simultaneous effects of capillary pressure and relative permeability in the context of CO<sub>2</sub> plume geometry and well head pressure propagation. For this study, artificial neural networks (ANN), one of widely used machine learning methods, is applied to capture features of CO<sub>2</sub> saturation and fluid pressure propagation on the basis of 460 physics-based simulations describing different combinations of parameters from capillary pressure and relative permeability models. In addition, the CO<sub>2</sub> saturation and pressure migration under unknown capillary pressure and relative permeability conditions are predicted. The results demonstrate that the trained ANN model accelerates the CO<sub>2</sub> saturation and fluid pressure distribution prediction by at least 25,000%. Results are analyzed on the basis of response surface maps to understand systematic variations of fluid migration across a complete 3-D parameter space comprising capillary entry pressure ( $P_o$ ), phase interference ( $\lambda$ ), and residual CO<sub>2</sub> saturation ( $S_{gr}$ ). This

## Chapter 1 Introduction

analysis shows that entry pressure ( $P_o$ ) is the dominant parameter controlling CO<sub>2</sub> plume geometry and pressure accumulation. Small  $P_o$  encourages fluid migration and large  $P_o$  inhibits fluid migration. Meanwhile, the effects of  $\lambda$  and  $S_{gr}$  increase with increasing  $P_o$ : (1) large  $\lambda$  and small  $S_{gr}$  encourage the migration of CO<sub>2</sub> saturation; and (2) high  $S_{gr}$  encourages the migration of pressure to a large extent comparing to  $\lambda$ .

Understanding the fluid migration mechanisms is critical for estimating CO<sub>2</sub> storage efficiency and developing effective risk management strategies because leakage from CO<sub>2</sub> storage reservoir may cause serious environmental impacts. Quantifying the migration, transportation, and distribution of injected CO<sub>2</sub> is necessary for industrial-scale CO<sub>2</sub> injection siting process. The studies presented here combine classical physic-based numerical simulation strategies with recent advances in machine learning emulation to identify the controls on multi-phase fluid dynamics in higher dimensional parameter space. These studies provide important new insights that constrain the role of capillary and mineral trapping mechanisms during industrial-scale CCS, while demonstrating the tremendous computational efficiency that may be attained by training machine learning emulators on the basis of multi-physics numerical simulations.

## Chapter 2

# A parametric analysis of capillary pressure effect

## 2.1 Introduction

Carbon capture and sequestration (CCS) is being considered as a technological approach to mitigate the adverse effects of excessive atmospheric CO<sub>2</sub>, which has been implicated in rising global temperatures and other serious environmental issues (Bennion and Bachu, 2005; Egermann et al., 2006; Szulczewski et al., 2012; Michael et al., 2010; Metz et al., 2005). During CCS, the CO<sub>2</sub> produced at point source generators (e.g., gas- or coal-fired power plants, ethanol factories) is captured and injected into deep geologic reservoirs to prevent atmospheric release. Deep brine aquifers have been recognized as suitable CCS reservoirs on the basis of (1) widespread worldwide distribution (Bennion and Bachu, 2005; Shi et al., 2011; Krause et al., 2011) and (2) much larger CO<sub>2</sub> storage capacity in comparison to depleted oil/gas reservoirs, and coal beds (Michael et al., 2010; Iglauer et al., 2011), which need to be fully depleted for maximum storage capacity (Bennion and Bachu, 2005; Metz et al., 2005).

The success of a CCS project depends on whether or not the injected CO<sub>2</sub> remains isolated in the disposal reservoir over timescales beyond 10<sup>4</sup> years (Metz et al., 2005; Shaffer, 2010). Within sedimentary basins, a typical CCS reservoir morphology is characterized by a high-permeability sandstone or carbonate aquifer that is sealed from above by a low permeability cap

rock, such as shale (Benson and Cole, 2008). In this configuration, the brine aquifer is the target reservoir for CO<sub>2</sub> injection and storage, and the overlying cap rock serves as a barrier to prevent CO<sub>2</sub> leakage. Within a layered sedimentary basin, there are four types of CO<sub>2</sub>-trapping mechanisms, which are based on different physical processes and, as a result, occur over differing time scales. The four CO<sub>2</sub> trapping mechanisms, in order of increasing temporal efficacy, are: (1) structural trapping, (2) capillary trapping (residual trapping), (3) dissolution trapping (solubility trapping), and (4) mineral trapping (Iglauer et al, 2011; Benson and Cole, 2008; Nicot, 2008). Structural trapping is the mechanism by which the cap rock inhibits the vertical flow of buoyancy-driven CO<sub>2</sub>, thus trapping CO<sub>2</sub> within the disposal reservoir (Benson and Cole, 2008; Hesse et al., 2008). Capillary trapping (or residual phase trapping) is a process in which drainage and subsequent imbibition results in immobilized CO<sub>2</sub> due to capillary effects (Hesse et al., 2008; Hunt et al., 1988). Solubility trapping is the process by which CO<sub>2</sub> dissolves in brine, thus increasing the aqueous phase density and causing the CO<sub>2</sub> to sink within the reservoir (Hesse et al., 2008; Mito et al., 2008). Mineral trapping is the optimal trapping mechanism during which CO<sub>2</sub> acidifies the formation brine, causing mineral grain dissolution and precipitation of carbonate mineral phases, which results in permanent CO<sub>2</sub> isolation (Mito et al., 2008; Bachu et al., 1994).

In the context of CO<sub>2</sub> sequestration, there are two fluid mass components, brine and CO<sub>2</sub>. The CO<sub>2</sub> mass component is typically injected at depths greater than 800 m, where it exists as a supercritical phase fluid and is thus kinetically favorable for transportation (van der Meer, 1992). This supercritical CO<sub>2</sub> (scCO<sub>2</sub>) phase is commonly called the “gas phase” because it has been shown that scCO<sub>2</sub> is typically the non-wetting phase in a CO<sub>2</sub>-brine system. In contrast, the brine mass component is the “liquid phase”, which is the wetting phase in the CO<sub>2</sub>-brine fluid system (Pini and Benson, 2013). The fraction of CO<sub>2</sub> dissolved in brine is referred to as aqueous phase CO<sub>2</sub> (aqCO<sub>2</sub>). It is also worth noting that water vapor can dissolve in scCO<sub>2</sub>; however, the solubility of water in CO<sub>2</sub> is much lower than the solubility of CO<sub>2</sub> in water (Pruess and García, 2002). As CO<sub>2</sub> has lower solubility in brine than in pure water (Enick and Klara, 1990), the two fluid

components, CO<sub>2</sub> and brine, are generally treated as immiscible fluids in the porous medium. In a pore space, at the boundary between these two fluids, interfacial tension exists because there is a pressure difference (capillary pressure) across the boundary (Brown, 1951), thus the CO<sub>2</sub>-brine system is referred to as a capillary system. During the process of CO<sub>2</sub> injection and subsequent trapping in the reservoir, capillary pressure ( $P_{cap}$ ), relative permeability ( $k_{rel}$ ), and gravity forces (including buoyancy) significantly affect the mobility of each mass component, and the distribution of different phases (Bennion and Bachu, 2005; Krause et al., 2011; Brown, 1951; Pini et al., 2012). As a result, interactions between relative permeability, capillary pressure, and phase mobility are relevant for assessing the storage efficacy of CO<sub>2</sub> sequestration projects.

Due to large differences between density of the injected CO<sub>2</sub> and the formation brine, CO<sub>2</sub> is buoyant and there is potential for leakage to shallower depths and/or atmospheric release (Bachu, 2003; Krevor et al., 2011; Esposito and Benson, 2011). To understand how multi-phase reservoir properties affect CO<sub>2</sub> mobility in porous geologic media, numerous laboratory and simulation studies have been completed to quantify how variations in water saturation affect both relative permeability and capillary pressure characteristics (Ferrand and Celia, 1992; Chaouche et al., 1994; Ataie-Ashtiani et al., 2002; Arns et al., 2003). For example, Pollyea (2016) shows how relative permeability uncertainty affects injection pressure accumulation and CO<sub>2</sub> plume geometry, and Juanes et al. (2006) concludes that relative permeability hysteresis is required to assess the immobilized amount of CO<sub>2</sub> accurately through capillary trapping. Similarly, Han et al. (2010) found that heterogeneous permeability fields with greater anisotropy potentially maximize residual CO<sub>2</sub> trapping.

To assess the efficacy of geologic CO<sub>2</sub> sequestration prior to the construction of a large-scale project, reservoir-scale numerical simulations are commonly used to understand the risk profile and performance attributes of CO<sub>2</sub> sequestration sites better (Pruess and García, 2002). To implement numerical simulation for site-scale performance or risk assessment, rock properties must be known or estimated for every location in the reservoir; however, there are frequently

insufficient data available at the reservoir scale. As a result, data obtained from laboratory experiments on core samples are commonly used to represent reservoir properties at much larger scales (Yu et al., 1998). In the context of CCS modeling, capillary pressure drainage curves are an important system attribute that is typically measured at laboratory scales and then directly incorporated into numerical models. For example, André et al. (2014) use a laboratory-measured gas-water capillary pressure curve to simulate the near-well field for determine the optimal CO<sub>2</sub> injection rate. These results show that capillary forces play an important role during the desiccation process near injection wells and a sufficiently high gas injection rate can overcome the capillary forces. In addition, Berg et al. (2013) and Roels et al. (2016) observed the important impact of capillary forces on salt precipitation near injection well, which results in potential well clogging risk. However, at the same time, much research has proven that heterogeneity at sub-core scale affects capillary pressure-saturation curves, which can significantly affect simulated CO<sub>2</sub> saturation profiles (Shi et al., 2011; Chaouche et al., 1994; Ataie-Ashtiani et al., 2002; Perrin et al., 2009). One implication of sub-core heterogeneity is that experimentally derived capillary pressure-saturation models exhibit a wide range of both entry pressure and curvature for the same rock type. For example, capillary pressure measurements for sandstone core samples show as much as two to three orders of magnitude difference for a given wetting phase saturation (Pini et al., 2012; André, 2014; Berg et al., 2013; Roels et al., 2016; Bachu and Bennion, 2008; Oh et al., 2013). Specifically, these studies indicate that capillary pressure can range from 60 kPa to 8,000 kPa, and entry pressure can range from 1 kPa to 200 kPa, and this variability increases as the wetting phase saturation decreases (Fig. 2.1).

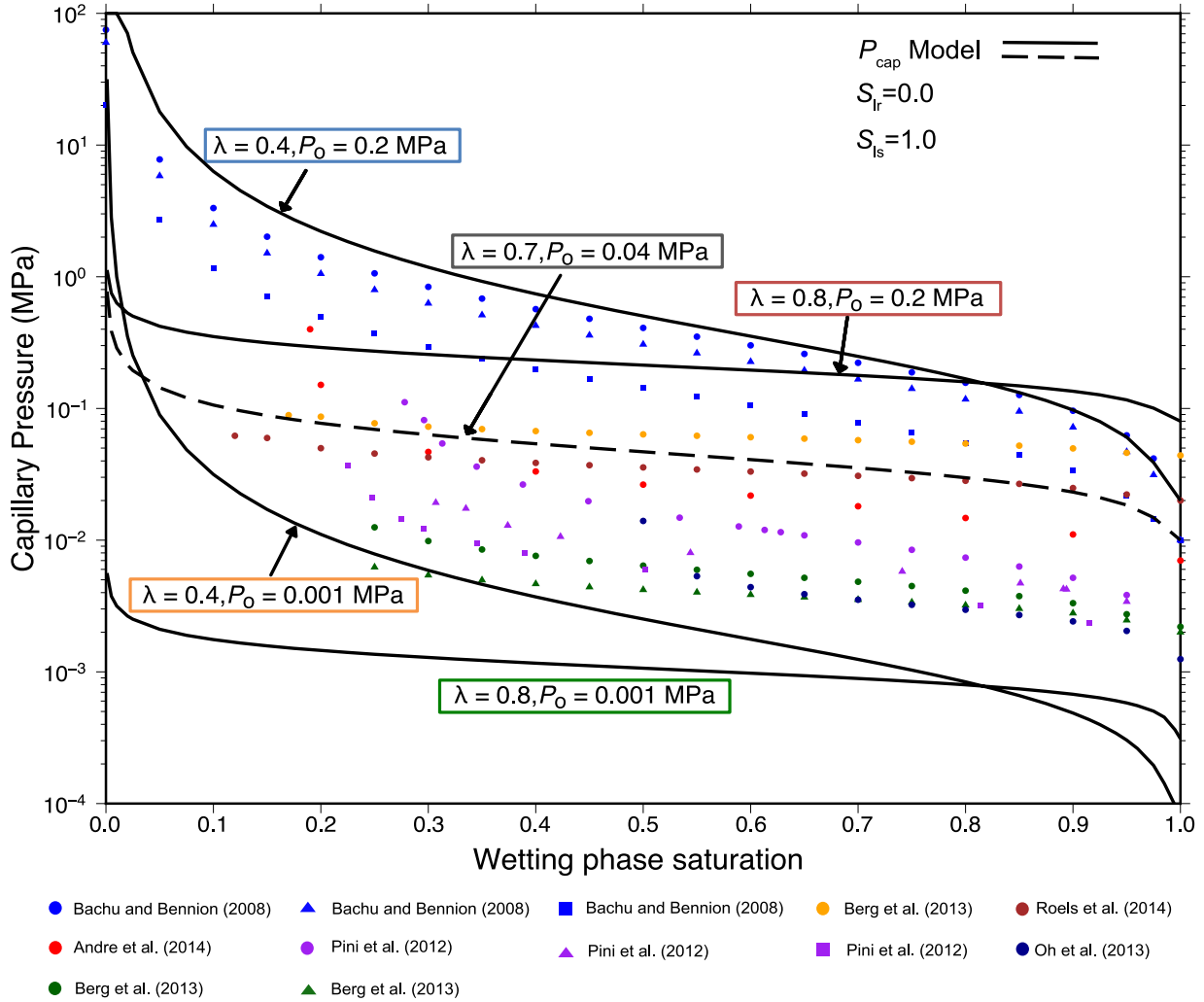


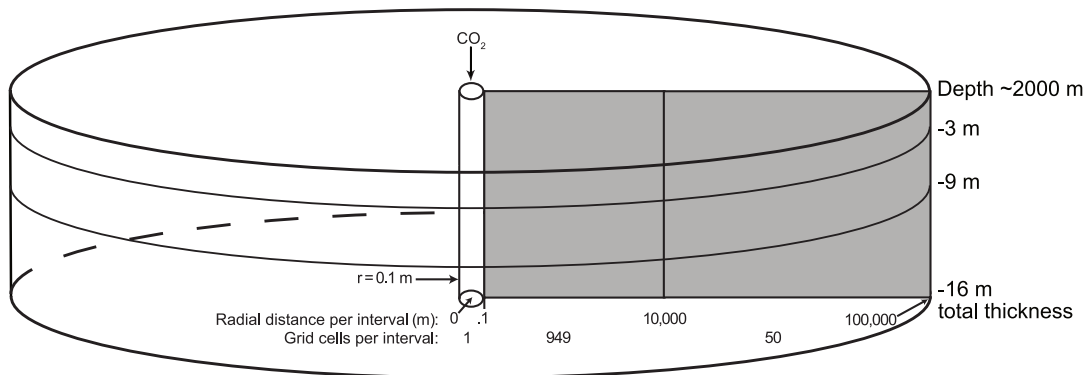
Figure 2.1: Experimental capillary pressure measurements of sandstone samples in the literature and range of capillary pressure curves used in this study. Black solid lines represent van Genuchten capillary pressure models (Eq. 1 and 2) that bound the range of capillary pressure measurements, while the dashed line represent an intermediate case. Each van Genuchten model is specified with unique  $\lambda$  and  $P_0$  parameter combinations, and the remaining parameters ( $S_{ls}$ ,  $S_{lr}$ ) are identical (Table 2.1).

The objective of this study is to discover how this substantial variability in experimental capillary pressure measurements affects the  $scCO_2$  movement and shape of plume in a sandstone reservoir during  $CO_2$  injection. In doing so, a numerical modeling experiment is utilized to quantify the effects of variability in capillary pressure models during  $CO_2$  injections with an emphasis on the drainage phase of the process. Results from this study provide a better understanding of the mechanisms for the movement of  $CO_2$  in the subsurface, which can benefit

the efficiency of numerical models used to understand the risk profile and performance attributes of CO<sub>2</sub> sequestration projects.

## 2.2 Conceptual Model and Methods

For this study, a numerical modeling experiment is implemented to understand how capillary pressure variability affects gas and aqueous phase partitioning and plume geometry during CO<sub>2</sub> injections in a sandstone reservoir. The conceptual model comprises a synthetic homogeneous sandstone reservoir with 16 m thickness and 100 km lateral extent (Fig. 2.2). The model domain is discretized as a 2-D radially symmetric cylinder with constant 2 m grid cell thickness. The injection well is modeled as the innermost column of grid cells with radii of 0.1 m. Beyond the injection well, 949 grid cells are discretized with logarithmically increasing increments ( $\Delta r$ ) from 0.1 m to 10,000 m, and 50 additional grid cells are discretized with logarithmically increasing  $\Delta r$  between 10,000 m and 100,000 m to represent a semi-infinite far field dimension. This 100 km lateral dimension is designed to ameliorate pressure feedbacks from the far-field boundary. As a result, upper, lower, and far-field boundaries are specified as adiabatic (no flux) boundaries, and the innermost boundary is specified with a Neumann condition to represent a constant rate of CO<sub>2</sub> injection. Initial conditions represent a disposal reservoir at 2,000 m depth (20 MPa fluid pressure) and temperature of 75 °C, thus injected CO<sub>2</sub> will exist in the supercritical phase (Szulczewski et al., 2012; Michael et al., 2010; Bachu et al., 1994; Bachu, 2003). Porosity and permeability parameters in this study are specified using the measurements from Berg et al. (2013), and the complete list of system parameters are presented in Table 2.1.



not to scale

Figure 2.2: 2-D symmetric model domain used in this study. The injection well is modeled as a single column of grid cells with 0.1 m radii located in the domain center. The next 949 grid cell radii increase logarithmically to 10,000 m, after which 50 grid cells increasing logarithmically to 100,000 m. The sandstone reservoir thickness is 16 m and all the grid cells with a constant 2 m thickness. Supercritical  $\text{CO}_2$  injection rate through injection well is 8.0 kg/s (252,461 MT/yr) and injection time is 10 years.

In 2016, the total U.S. energy-related  $\text{CO}_2$  emissions were 5,171 million metric tons (MER, 2018). In this study,  $\text{scCO}_2$  is injected into the reservoir for 10 years with a constant rate 8.0 kg/s, which is equivalent to 252,461 metric tons per year (MT/yr). This injection rate is distributed evenly (1.0 kg/s) within each of the eight grid cells comprising the injection well, and I assume the  $\text{CO}_2$  is injected at reservoir temperature and pressure to focus analysis on the effects of capillary pressure uncertainty. The amount of  $\text{CO}_2$  injected in this study is equivalent to the annual emissions from a 140 MWh natural gas fired power plant (EIA, 2018).

Table 2.1: Bulk reservoir properties used in this model

<i>Reservoir properties</i>			
Property	Symbol	Value	Units
Fluid Pressure	$P_f$	20	MPa
Temperature	T	75	°C
Salinity	$C_{NaCl}$	10,000	ppm
Permeability	$k$	$4 \times 10^{-13}$	$m^2$
Porosity	$\phi$	0.2	-
Density	$\rho_r$	2038	$kg\ m^{-3}$
Specific heat	$C_p$	1000	$J\ (kg\ K)^{-1}$
Thermal conductivity	$\kappa_r$	1.6	$W\ (m\ K)^{-1}$

<i>Relative permeability model</i>			
Property	Symbol	Value	Units
van Genuchten fitting	$\lambda$	0.457	-
Residual liquid saturation	$S_{lr}$	0.3	-
Saturated liquid saturation	$S_{ls}$	1.0	-
Residual gas saturation	$S_{gr}$	0.25	-

Capillary pressure-saturation curves have been measured experimentally in rock cores from numerous CCS sites worldwide. A literature review of these experimental CO<sub>2</sub>-brine capillary pressure ( $P_{cap}$ ) measurements reveals highly variable  $P_{cap}$ -saturation curves for the typical sandstone reservoir rocks (Fig. 2.1). The aim of this study is to quantify the effects of this  $P_{cap}$  variability on CO<sub>2</sub> movement and plume development during a 10-year injection period at reservoir scale.

For this study, capillary pressure effects are accounted for in multi-phase CO<sub>2</sub>-brine flow using the van Genuchten model, which relates capillary pressure across the CO<sub>2</sub>-brine interface as a function of wetting phase saturation (van Genuchten, 1980; Pruess et al., 1999). In this formulation, capillary pressure is calculated as:

$$P_{cap} = -P_o \left( [S^*]^{-\frac{1}{\lambda}} - 1 \right)^{1-\lambda}, \quad (1)$$

where,  $P_o$  is the entry pressure, which characterizes the pressure required for the gas phase to first enter the pore network,  $\lambda$  is related to the van Genuchten fitting parameter, which controls the curvature of the model, and  $S^*$  is the effective wetting phase saturation which defined as

$$S^* = \frac{S_l - S_{lr}}{S_{ls} - S_{lr}}. \quad (2)$$

For Equation 2,  $S_l$  is wetting phase saturation,  $S_{lr}$  is the residual wetting phase saturation, and  $S_{ls}$  is the saturated wetting phase saturation. The wetting phase in porous media becomes immobile if the liquid saturation reaches  $S_{lr}$ , while  $S_{ls}$  is the saturation when the wetting phase is fully mobile. The effective wetting phase saturation rescales the wetting phase saturation from 0 to 1 over the range of saturation states in which mass components are mobile.

Four van Genuchten models of capillary pressure can effectively bound the variability of experimental measurements acquired from the literature (Fig. 2.1, solid black lines). These experimental data are from various sandstone core samples acquired from various geologic formations, including Cardium (porosity ( $\phi$ ) = 0.15), Berea ( $0.20 \leq \phi \leq 0.22$ ), Arqov ( $\phi = 0.11$ ), Vosges ( $\phi = 0.22$ ), and Bentheimer ( $\phi = 0.21$ ). These capillary pressure models are characterized by two parameters ( $\lambda$  and  $P_o$ ) of van Genuchten model, and the full range of experimental variability is accounted for when  $\lambda$  ranges from 0.4 to 0.8 and  $P_o$  ranges from 1 kPa to 200 kPa. A parameter table defining these capillary pressure models is developed by varying  $\lambda$  and  $P_o$  to fully bound the range of experimental measurements (Fig. 2.3). The discretization for the variabilities of parameters are arbitrarily selected and this results in 189 parameter combinations for  $\lambda$  and  $P_o$ . As a result,  $S_{lr}$  and  $S_{ls}$  are 0.0 and

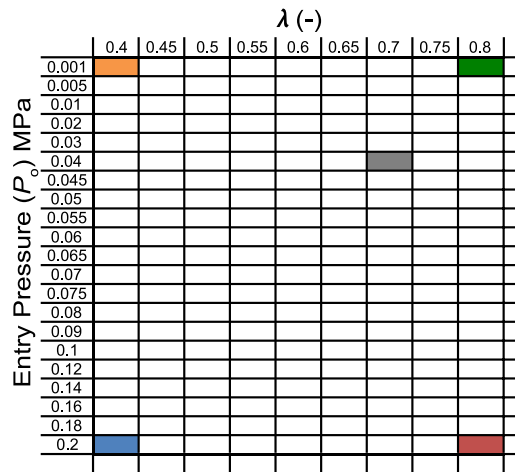


Figure 2.3: Capillary pressure parameters used in this study. The  $\lambda$  parameter controls curvature in the van Genuchten model, and entry pressure ( $P_0$ ) represents the pressure drop across the interface. Individual simulations are performed for 189 unique combinations of  $\lambda$  and  $P_0$ . The five color cases denote parameter combinations for the van Genuchten models that represent the four end-member cases and one intermediate case for the experimental capillary pressure-saturation measurements (note that colors correspond with shading in Figure 2.1).

0.999, respectively, and remain constant. The maximum capillary pressure is determined as 50 MPa based on the experimental measurements. The relative permeability model is also an important factor controlling the multi-phase CO<sub>2</sub>-brine flow (Pollyea, 2016), but in this study the influence of capillary pressure is isolated by maintaining the same relative permeability model for each simulation. Relative permeability parameters are listed in Table 2.1 and the generic relative permeability curves are illustrated in Figure 2.4.

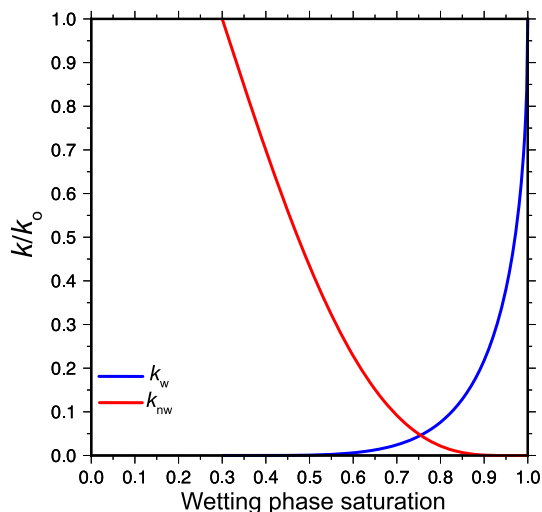


Figure 2.4: Relative permeability ( $k_{rel}$ ) model used for this study. Parameters presented in Table 2.1.

The code selection for this study is TOUGH3 (Jung et al., 2017), which is compiled with the fluid property module, ECO2N (Pruess, 2005). The ECO2N fluid property module is designed for problems involving geologic carbon sequestration, and is capable of simulating mixtures of water, NaCl, and  $\text{CO}_2$  on the basis of equilibrium solubility constraints (Pruess, 2005). Each combination of parameters ( $\lambda$  and  $P_o$ ) represents one simulation (each grid cell in Fig. 2.3), and a total 189 simulations are completed over the parameter space.

## 2.3 Results

The model scenario simulates 10 years of  $\text{CO}_2$  injection, and a total of 189 simulations were completed for the  $\lambda$ ,  $P_o$  parameter combination shown in Figure 2.3. The simulation results show the response of  $\text{CO}_2$  movement and plume development as functions of  $\lambda$  and  $P_o$  during the injection period. To understand the effects of capillary pressure variability, simulation results are analyzed for four  $\lambda$ ,  $P_o$  parameter combination bounding the parameter space (Fig. 2.1, solid lines), and one  $\lambda$ ,  $P_o$  parameter combination representing an intermediate case (Fig. 2.1, dashed line).

The gas (supercritical) phase CO<sub>2</sub> saturation for these five cases are shown in Figure 2.5. Capillary pressure strongly influences vertical CO<sub>2</sub> flow, so the ratio of vertical to horizontal mass flow rates is shown for gas phase CO<sub>2</sub> in Figure 2.6. These figures illustrate that the capillary pressure model strongly affects CO<sub>2</sub> plume geometry. To evaluate the competing effects of capillary pressure and buoyancy pressure at grid-cell scale, I calculate a modified Bond number ( $\omega$ ) to represent the ratio of buoyancy pressure to capillary pressure within each grid cell for each of the model scenarios (Fig. 2.7). To understand how  $\omega$  varies across the complete parameter space, Figure 2.8 presents the average  $\omega$  ratio calculated from all grid cells with non-zero CO<sub>2</sub> saturation for each run in the complete ensemble of 189 simulations (i.e.,  $\lambda$  and  $P_o$  combinations). All the figures show the results after 10 years of injection.

## 2.4 Discussion

### 2.4.1 Carbon Dioxide Plume Geometry

Simulation results show that capillary pressure strongly controls the spatial distribution of gas phase CO<sub>2</sub> as it flows away from the injection well into the storage reservoir (Fig. 2.5). Interestingly, for low entry pressure ( $P_o = 1$  kPa) CO<sub>2</sub> plume geometry is remarkably similar regardless of  $\lambda$  (Fig. 2.5A, B). Specifically, the CO<sub>2</sub> plume develops a cone shape with uniform CO<sub>2</sub> saturation levels ranging between 0.5 and 0.7 within the plume core and a small zone of decreasing CO<sub>2</sub> saturation at the plume edge. As a result, the overall plume geometry is generally governed by near vertical CO<sub>2</sub> flow within the lower half of the reservoir, while spreading causes lateral flow in the upper half of the reservoir. Moreover, as the CO<sub>2</sub> injection well encompasses the full thickness of the reservoir, the vertical flow in the lower half and the lateral flow in the upper half leads to the step shape at the edge of the plume. This suggests that, when entry pressure is low, buoyancy effects are the dominant control on CO<sub>2</sub> distribution. For high entry pressure cases

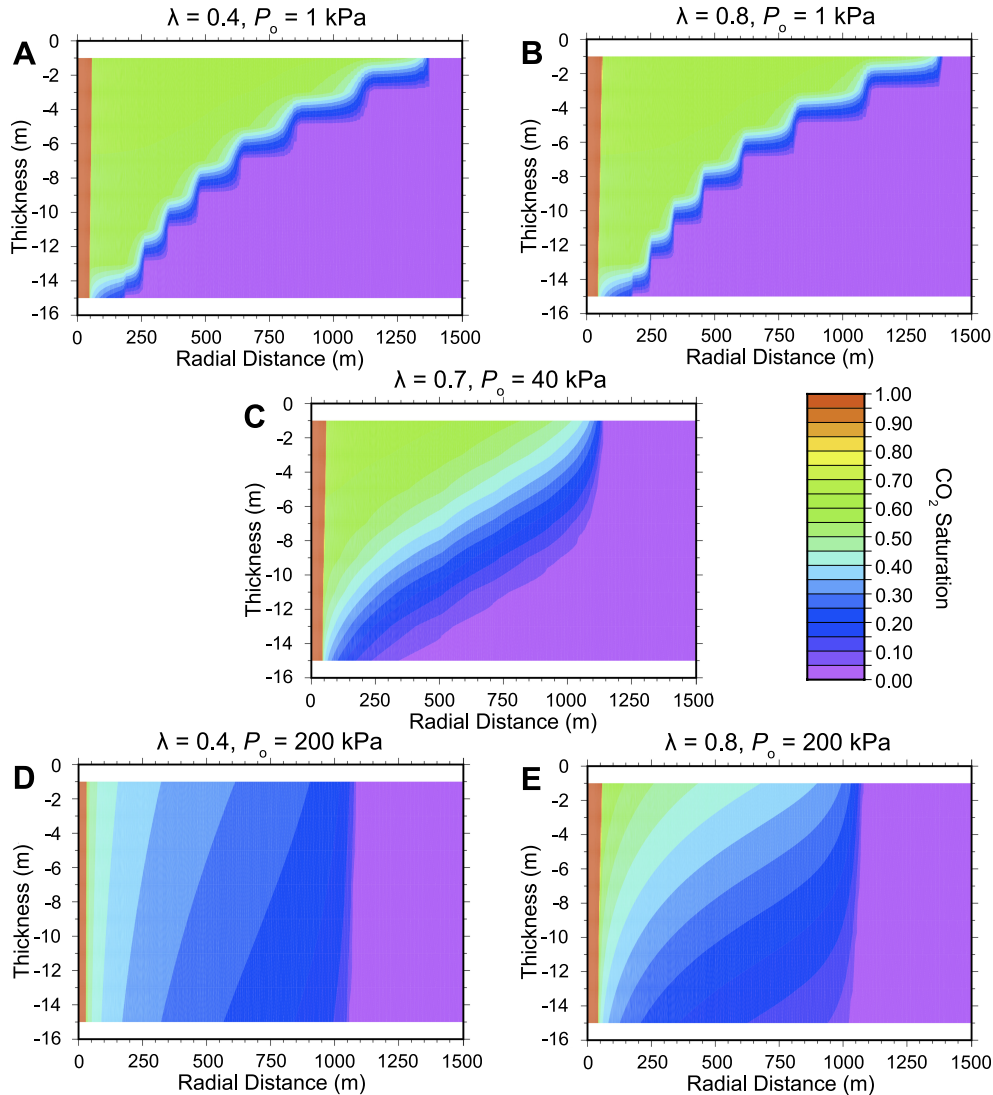


Figure 2.5: Gas phase CO<sub>2</sub> saturation after 10 years of constant rate CO<sub>2</sub> injection at 8.0 kg/s (252,461 MT/yr). A-E are the results for unique  $\lambda, P_o$  parameter combinations highlighted in Figure 2.3.

( $P_o = 200 \text{ kPa}$ ), CO<sub>2</sub> plume geometry is characterized by lower overall CO<sub>2</sub> saturation levels that occupy a larger vertical extent within the reservoir (Fig. 2.5D, E). Interestingly, the influence of  $\lambda$  becomes pronounced with increasing  $P_o$ . In the context of the  $P_{cap}$ -saturation curve (Fig. 2.1), the  $\lambda$  parameter governs curvature, so that low  $\lambda$  results in higher  $P_{cap}$  for the same entry pressure. As a result, the combination of low  $\lambda$  and high  $P_o$  is highly restrictive to buoyancy forces, and lateral flow governs the plume geometry for this scenario. In aggregate, these results indicate that

$P_o$  is the primary control on plume geometry, while  $\lambda$  is influential only for high  $P_o$ . Moreover, the effects of  $P_o$  on CO<sub>2</sub> plume migration are that low  $P_o$  favors buoyancy (vertical flow), while high  $P_o$  inhibits vertical CO<sub>2</sub> flow. As a result,  $P_o$  is shown here to have a significant effect on the physical trapping characteristics of a clastic reservoir, which is a balance between buoyancy and capillary force.

## 2.4.2 Vertical CO<sub>2</sub> Flow

The previous discussion of CO<sub>2</sub> saturation profiles for five  $\lambda$ ,  $P_o$  combinations (Fig. 2.3) illustrates that buoyancy governs the upward movement of CO<sub>2</sub> in the reservoir, and previous investigators have shown results similar to Figure 2.5 (Esposito and Benson, 2011; André et al., 2014; Carpita et al., 2006). To characterize this behavior in the context of variability in the  $P_{cap}$ -saturation model, the ratio of vertical-to-horizontal gas phase CO<sub>2</sub> flux (VHF) is calculated for two depth transects through each domain (Fig. 2.2 and 2.6). In this chapter, VHF is used for discussion but not the absolute vertical flux, which is too small for quantitative comparison. The red line represents the result at depth ~2,003 m, which is 3 m beneath the top of the reservoir (Fig. 2.2) and the black line is for ~2,009 m (9 m beneath the reservoir top). The results reflect the degree of vertical flux at the upper part and the center of the reservoir.

Similarly, when entry pressure is low, the effects of increasing  $\lambda$  cause modest increases in the VHF ratio, suggesting that  $\lambda$  plays a minor role in vertical CO<sub>2</sub> flow (Fig. 2.6A, B). In addition, Figure 2.6A and 2.6B shows that the VHF ratio at -9m depth within the reservoir is larger than that at -3m depth, indicating that the vertical component of CO<sub>2</sub> flow is stronger at deeper depths within the reservoir and this effect also increases modestly with increasing  $\lambda$ . Alternatively, for high entry pressure cases ( $\lambda = 0.7$ ,  $P_o = 40$  kPa and  $\lambda = 0.8$ ,  $P_o = 200$  kPa), the VHF for both depths approaches nil except when there is some downward gas phase CO<sub>2</sub> flux at the edge of the plume (Fig. 2.6C, E). The downward flux at -9 m is larger in comparison to the downward flux

at -3 m. Specifically, for the case with high entry pressure and small  $\lambda$  ( $\lambda = 0.4$ ,  $P_o = 200$  kPa), the vertical

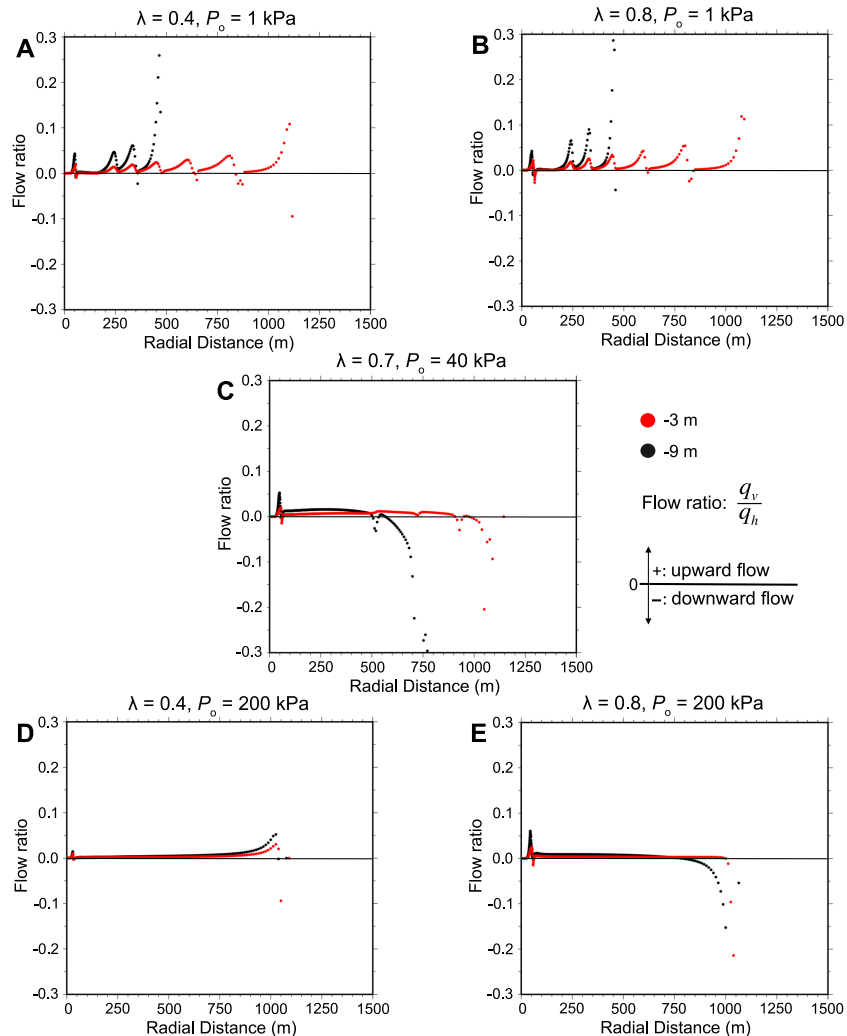


Figure 2.6: Vertical to horizontal flow ratio (VHF) of supercritical CO<sub>2</sub> for the five  $\lambda$ ,  $P_o$  parameter combinations highlighted in Figure 2.3. VHF is a ratio of vertical flow rate (kg/s) and horizontal flow rate (kg/s). Red and black dots represent depths -3 m and -9 m, respectively. If flow ratio is positive, gas phase flows upward. If flow ratio is negative, gas phase flows downward. I further note that oscillations in the VHF profiles result from (1) rapidly upward flow that occurs at grid cells bounding the plume, particularly within low  $P_o$  cases, and (2) lower buoyancy force in the grid cells just beyond the plume where CO<sub>2</sub> dissolution increases brine density.

gas phase CO<sub>2</sub> movement also only happens at the edge of the plume but in the upward direction (Fig. 2.6D). However, the scale of this vertical movement is negligible. For each case, around 50 m away from the injection well, which is also the edge of the fully saturated CO<sub>2</sub> zone, there is an

unexpected fluctuation of vertical movement. This results from a large drop in saturation across the interface between the fully drained zone and CO<sub>2</sub> plume.

## 2.4.3 Buoyancy versus Capillary Force

To better understand the mechanism of upwardly mobile CO<sub>2</sub> flow, I interrogate the buoyancy characteristics of the CO<sub>2</sub>-brine capillary system in the context of variability in capillary pressure-saturation models.

### 2.4.3.1 Quantifying Buoyancy Characteristics

The displacement of wetting phase fluids (drainage) during CO<sub>2</sub> flow within porous media is thoroughly discussed in the work of Lenormand et al. (1988) and Lenormand (1990). Specifically, the behavior of non-wetting phase invasion is described by a set of dimensionless numbers: capillary number (Ca), viscosity number (M), and Bond number (Bo), the latter defining the importance of gravitational forces compared to surface tension forces. As geometry of a porous network in simulation is different from that of experimental samples, Løvoll et al. (2005) redefined the Bond number:

$$Bo = \frac{\Delta\rho g l \bar{r}}{2\gamma}, \quad (3)$$

where,  $\Delta\rho$  is the density difference between immiscible fluids,  $g$  is gravitational acceleration,  $l$  is the tube length,  $\bar{r}$  is the average tube radius over the system, and  $\gamma$  is the surface tension.

For this study, I augment the Bond number to account for variable phase saturation and demonstrate its relationship of buoyancy and capillarity.

The direction of buoyancy is always upward because the formation brine is more dense than free-phase CO<sub>2</sub>. In contrast, the capillary force is the resisting force for inhibiting upward CO<sub>2</sub> from invading into the pore network. These two forces, which work in opposite directions, are

responsible for the movement of vertical CO<sub>2</sub> flow. In this study, I introduce the parameter  $\omega$ , which like Bo is the ratio of buoyancy pressure to capillary pressure; however,  $\omega$  is developed in terms of the relative fraction of non-wetting CO<sub>2</sub> in the pore network and allows a direct quantitative assessment of the capillary system on the basis of numerical simulation results. Specifically,  $\omega$  is the ratio of (1) buoyancy pressure attributable to the density differential between the CO<sub>2</sub> and brine and scaled by CO<sub>2</sub> saturation and, (2) capillary pressure as quantified during simulation by Equation 1. The parameter  $\omega$  is described qualitatively as,

$$\omega = \frac{\text{buoyancy pressure}}{\text{capillary pressure}}, \quad (4)$$

and defined mathematically as,

$$\omega = \frac{(\rho_w - \rho_{nw})gbS_{nw}}{P_{cap}}, \quad (5)$$

where,  $\rho_w$  and  $\rho_{nw}$  are brine and CO<sub>2</sub> density, respectively,  $g$  is gravitational acceleration,  $b$  is grid cells thickness (2 m),  $S_{nw}$  is gas phase CO<sub>2</sub> saturation, and  $P_{cap}$  is capillary pressure, which is calculated within each model grid cell on the basis of the capillary pressure-saturation model (Eq. 1), and  $S_w$  is brine saturation where,  $S_{nw} + S_w = 1$ . When buoyancy pressure is larger than capillary pressure, then  $\omega > 1$ , and upward CO<sub>2</sub> flow is favored. In contrast, when buoyancy pressure is smaller than capillary pressure, then  $\omega < 1$ , and capillary pressure governs the capillary system and upward CO<sub>2</sub> movement is inhibited.

### 2.4.3.2 Balance of Buoyancy and Capillarity

To evaluate the relationship between buoyancy and capillary force within simulations described by highly variable  $P_{cap}$ -saturation curves, the  $\omega$  value is calculated for each grid cell and plotted in log scale (Fig. 2.7). In Figure 2.7, the red shading indicates that  $\log \omega > 0$ , resulting

in the scenario where buoyancy is the dominating force and gas phase  $\text{CO}_2$  moves upward. Conversely, the blue shading in Figure 2.7 indicates that  $\log \omega < 0$ , which represents a system governed by capillarity in which upward flow is inhibited.

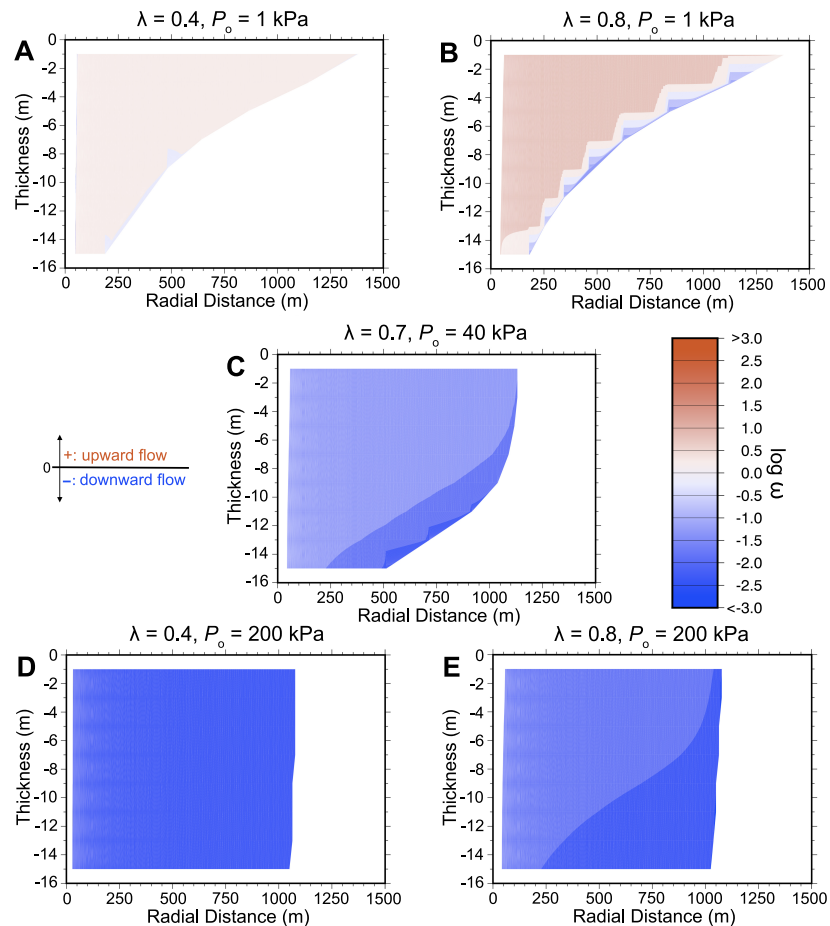


Figure 2.7: Log  $\omega$  for the five  $\lambda, P_0$  parameter combinations highlighted in Figure 2.3. Red indicates  $\log \omega > 0$ , which is the buoyancy driven region; while blue indicates  $\log \omega < 0$ , which is the capillary force driven region.

In Figure 2.7, the buoyancy-dominated scenarios ( $\log \omega > 0$ ) are apparent for simulations characterized by low entry pressure ( $P_0 \approx 1 \text{ kPa}$ ). In contrast, the capillary force-dominated scenarios ( $\log \omega < 0$ ) are presented in the simulations with medium to large entry pressure ( $P_0 \approx 40 - 200 \text{ kPa}$ ). Additionally, capillarity appears to govern the lateral plume boundaries for the two model scenarios defined by low  $P_0 = 1 \text{ kPa}$  simulations. For the two  $P_0 = 1 \text{ kPa}$  simulations, capillary

pressure is smaller, and this results in the buoyancy dominated upward CO<sub>2</sub> movements (Fig. 2.7A, B). However, for the other three simulations with medium to high entry pressure, capillary pressure is larger than buoyancy pressure so that the log-scale  $\omega$  value is negative (Fig. 2.7C-E). As a result, in these cases, upward CO<sub>2</sub> movements are diminished.

At the edge of the CO<sub>2</sub> plume, for low entry pressure cases, there is a situation in which capillary force is larger than buoyancy (Fig. 2.7B, blue shading). This results from comparatively high water saturation at the edge of the plume where pore drainage is in the early stages, thus capillary pressure is larger than buoyancy pressure. This occurs because low CO<sub>2</sub> saturation does not exert sufficient buoyancy to overcome the capillary pressure. As the injection of CO<sub>2</sub> continues, there is more CO<sub>2</sub> invading into pores and buoyancy increases which leads to the CO<sub>2</sub> upward flow.

### 2.4.3.3 Effects of Parametric Variability

The modeling results indicate that  $\omega$  is an effective parameter to examine the potential for upwardly mobile gas phase CO<sub>2</sub> flow. To evaluate how  $\omega$  varies across the complete ensemble of 189 parameter combinations ( $\lambda$  and  $P_o$ ) simulated for this study (Fig. 2.3), I calculate an average  $\omega$  value for each simulation and plot the results as a response surface in  $\lambda$ - $P_o$  space (Fig. 2.8). From top-right to bottom-left of Figure 2.8, the curvature of the response surface shows systematic change from buoyancy to capillarity control on the overall multiphase fluid system behavior. Specifically, the  $\partial\omega/\partial P_o$  gradient is approximately two times greater than the  $\partial\omega/\partial\lambda$  gradient, which indicates that entry pressure is the primary control on whether the CO<sub>2</sub>-brine system is characterized by buoyancy or capillarity. In addition, the  $\lambda$ - $P_o$  parameter threshold at which  $\bar{\omega}$  is equal to one ( $\log \bar{\omega} = 0$ ) represents the  $\lambda$ - $P_o$  parameter combinations that determine whether the capillary system is governed by buoyancy or capillarity.

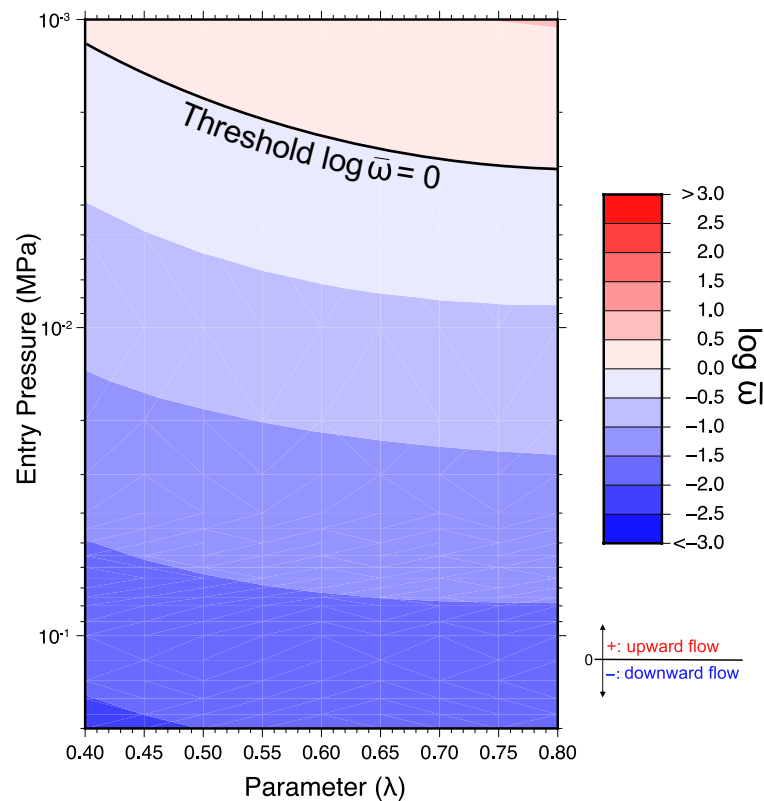


Figure 2.8: Response surface for  $\bar{\omega}$  calculated for the complete ensemble of 189 simulations (Figure 2.3). Red shading indicates  $\log \bar{\omega} > 0$ , which is a buoyancy dominated reservoir; while blue indicates  $\log \bar{\omega} < 0$ , which is a capillary force dominated reservoir.

The conclusion obtained from average  $\bar{\omega}$  response surface is consistent with the conclusion from vertical gas phase flux analysis, which is that  $P_o$  strongly governs the vertical  $\text{CO}_2$  flow and  $\lambda$  only with minimal influence on  $\text{CO}_2$  vertical flow. Low entry pressure encourages vertical  $\text{CO}_2$  flow and represents a buoyancy-dominated situation. In the low entry pressure cases, vertical flow is favored which results in lateral spreading of free phase  $\text{CO}_2$  at the top of the storage reservoir. In contrast, large entry pressure inhibits vertical  $\text{CO}_2$  flow and indicates capillary force exhibits a stronger control on  $\text{CO}_2$  distribution. For medium to large entry pressures, simulation results show that horizontal  $\text{CO}_2$  flow is favored, which results in a more compact plume with  $\text{CO}_2$  distribution vertically throughout the reservoir.

## 2.5 Conclusion

Experimental measurements of capillary pressure ( $P_{\text{cap}}$ ) in the CO<sub>2</sub>-brine-sandstone system vary significantly in both  $P_{\text{cap}}$  magnitude and curvature over the full range of wetting phase saturation. To understand the implications of this variability in the context of industrial scale CO<sub>2</sub> injection operations, this study implements a numerical modeling experiment to quantify CO<sub>2</sub> flow characteristics over the range of measured  $P_{\text{cap}}$ -saturation curves acquired from experiments on sandstone cores. For this study, I use the van Genuchten capillary pressure model to bound an ensemble of experimental measurements extant in the literature and simulate CO<sub>2</sub> injections into a synthetic sandstone reservoir when the parameters ( $\lambda$  and  $P_o$ ) controlling the  $P_{\text{cap}}$ -saturation curve are systematically varied over the parameter space. Using results after 10 years of constant rate CO<sub>2</sub> injection, this study yields insights into the competing roles of capillarity and buoyancy as CO<sub>2</sub> invades porous sandstone at reservoir scales. For the given model scenario, the primary conclusions of this study are summarized below:

1. In the van Genuchten  $P_{\text{cap}}$ -saturation model, entry pressure ( $P_o$ ) controls the barrier to CO<sub>2</sub> invasion in a fully saturated pore network, while  $\lambda$  governs the rate of capillary pressure rise during drainage. Results from this study indicate that  $P_o$  is the first-order control on plume geometry, while  $\lambda$  exerts second-order effects only in the scenarios characterized by high  $P_o$ .
2. Entry pressure governs vertical CO<sub>2</sub> flow and the CO<sub>2</sub> distribution appears minimally impacted by the selection of  $\lambda$ . For low entry pressure, the upward CO<sub>2</sub> flow is encouraged. However, for high entry pressure, the upward CO<sub>2</sub> flow is inhibited.
3. Buoyancy and capillary force govern the spatial distribution of CO<sub>2</sub> within a disposal reservoir, and I illustrate how these competing effects can be readily summarized in simulation results using the  $\omega$  ratio, which is a modified Bond number and relates buoyancy pressure to capillary pressure. At the scale of individual simulations, the  $\omega$  ratio

## Chapter 2 A parametric analysis of capillary pressure effects

illustrates locations within the CO<sub>2</sub> plume in which buoyancy or capillarity will govern free phase CO<sub>2</sub> flow. Similarly, the average  $\omega$  across an ensemble of simulations is shown to be an effective metric for response surface analysis indicating which  $\lambda$ ,  $P_o$  parameter combinations result in capillarity or buoyancy dominant CO<sub>2</sub> reservoirs.

In conclusion, the results of this study yield important insights into the implications of capillary pressure uncertainty at reservoir scale. Although the modeling experiment implements a highly simplified representation of the reservoir scale CO<sub>2</sub>-brine system, this approach reveals the fundamental physics that become manifest as the  $\lambda$ ,  $P_o$  parameter space is systematically varied. Consequently, the result of this study may prove useful towards understanding how more complex, heterogeneous CO<sub>2</sub>-brine-sandstone systems respond to industrial-scale carbon sequestration operations.

## Chapter 3

# Modeling CO<sub>2</sub>-Water-Basalt Reactions in a Basalt Fracture Network

## 3.1 Introduction

Carbon capture and sequestration (CCS) has been proposed as a technically feasible strategy for reducing anthropogenic CO<sub>2</sub> emissions in the energy sector (Bennion and Bachu, 2005; Metz et al., 2005). Sedimentary basins are the most common geologic environment for CCS operations, but permanent mineral trapping in such environments occurs over time scales exceeding 10<sup>2</sup> – 10<sup>3</sup> years (Bachu et al., 1994; Mito et al., 2008; Benson and Cole, 2008). In contrast, basalt formations have been shown to accommodate mineral trapping of injected CO<sub>2</sub> over much shorter timescales, e.g., 10<sup>0</sup> – 10<sup>1</sup> years (Goldberg et al., 2008; Schaef et al., 2010; Rosenbauer et al., 2012; Gislason et al., 2010). During CCS in basalt reservoirs, CO<sub>2</sub> dissolution in formation water releases H<sup>+</sup> to drive mineral dissolution of olivine and pyroxene, which releases divalent cations (Ca<sup>2+</sup>, Mg<sup>2+</sup>, Fe<sup>2+</sup>) that react with bicarbonate to form secondary mineral phases, e.g., calcite, magnesite, siderite (Knauss et al., 1993; Wang and Giammar, 2013). Basalts contain up to 25% combined molar concentration of Ca, Mg, and Fe (McGrail et al., 2006), and the release of these cations from basalt dissolution is as much as two orders of magnitude larger when compared to more silica-rich rocks, such as sandstone (Wolff-Boenisch et al., 2006).

Mafic and ultramafic rocks are widespread on the Earth's surface (Oelkers et al., 2008). For example, Columbia River Basalt Group (CRBG) covers more than 164,000 km<sup>2</sup> of Washington, Oregon, and Idaho (McGrail et al., 2006; Reidel et al., 2002), and India's Deccan Volcanic Province (DVP), which is one of the largest terrestrial flood basalt formations, covers ~500,000 km<sup>2</sup> in west-central India (Eldholm and Coffin, 2000; Tiwari et al., 2001; McGrail et al., 2006). The large volume of continental basalt provinces offers tremendous CO<sub>2</sub> storage capacity in locations that have not traditionally been considered viable for CCS. Moreover, CCS in continental basalt reservoirs may provide an opportunity for mitigating the increasing CO<sub>2</sub> emissions in some developing countries (Szulczewski et al., 2012). For example, coal-fueled power plants are the major source of electricity generation in India, and the number of coal-fueled power plants is still growing, as adding 12 – 40 GW per year of coal-fueled plants capacity from 2015 to 2025 (Shearer et al., 2017). Total annual CO<sub>2</sub> emission in India was estimated as 2.24 billion tones (Mt) in 2017, which contributed ~7% to global CO<sub>2</sub> emissions, and the number will continuously grow based on the rapidly developing economy (Le Quéré et al., 2018; Holloway et al., 2009).

Given the opportunity for expanding CCS technology into basalt formations, there is currently considerable interest in the processes that govern mineral trapping in basalt reservoirs (Goldberg et al., 2008; Schaef et al., 2010; Rosenbauer et al., 2012; Gislason et al., 2010). Mineral trapping in basalt considers two steps: basalt dissolution and carbonate mineralization (McGrail et al., 2006). Hövelmann et al. (2012) presented experimental results showing that carbonate alteration products formed after 7 days of olivine sample exposure to CO<sub>2</sub> and water at 150°C. In addition, Xiong et al. (2017b) used X-ray  $\mu$ CT segmentation to show that secondary alteration products filled the flood basalt fractures up to 15 volume percent after 40 weeks of exposure to aqueous phase CO<sub>2</sub>. These experimental results illustrate that the timescale for mineral trapping in basalt reservoirs is orders of magnitude faster than the reactions in sandstone aquifers (Benson and Cole, 2008).

Two pilot-scale CO<sub>2</sub> injection tests have shown that mineral trapping in basalt reservoirs is feasible at the field scale. The CarbFix Project at Hellisheidi geothermal power plant in southwest Iceland injected 230 tons of aqueous CO<sub>2</sub> in 2012, and subsequent mass balance and tracer tests found that 95% of the injected CO<sub>2</sub> was mineralized within two years (Matter et al., 2016). Additionally, the Wallula Basalt Sequestration Pilot Project located in southeastern Washington, USA, injected ~1,000 metric tons of supercritical CO<sub>2</sub> in 2013. Analyses of post-injection sidewall cores found that carbon mineralization was widespread within the injection zone (McGrail et al., 2017). These two CO<sub>2</sub> injection projects have successfully demonstrated the feasibility of mineral trapping in basalt reservoirs; however, feedbacks between multi-phase fluid flow and geochemical mineralization reactions in basalt fractures remain poorly understood.

To understand the feasibility of industrial-scale CCS operations in basalt reservoirs, a number of recent modeling studies show that free-phase CO<sub>2</sub> may become physically trapped over the timescales required to allow for permanent CO<sub>2</sub> isolation through basalt fracture heterogeneity (Jayne et al., 2019a; Jayne et al., 2019b; Pollyea et al, 2014; Pollyea and Fairley, 2012). However, these studies are based on site-scale reservoir characteristics and neglect geochemical reactions, which precludes more detailed analyses of long-term mineral trapping characteristics in basalt formations. In contrast, Aradóttir et al. (2012) utilized reactive transport simulation to show that geologic conditions at the CarbFix site are conducive to mineral trapping, but this study neglected the complex fracture heterogeneity associated with basalt reservoirs. Moreover, the CarbFix project injects aqueous phase CO<sub>2</sub>, so feedbacks between multi-phase fluid processes and CO<sub>2</sub> mineralization did not need consideration.

Several recent studies yield insights into the nature of free-phase CO<sub>2</sub> infiltrating a basalt fracture network. At the outcrop scale, Gierzynski and Pollyea (2017) simulated supercritical CO<sub>2</sub> migrating vertically from a high-permeability basalt reservoir into the overlying low-permeability basalt flow interior. Using stochastic simulation methods comprising the same fracture network with spatially random permeability distributions, this study found that free-phase CO<sub>2</sub> tends to

accumulate at the fracture intersections (Fig. 3.1). Specifically, Gierzynski and Pollyea (2017) show that relative permeability effects decrease CO<sub>2</sub> mobility when a single fracture branches into one or more diverging fractures (Fig. 3.1). While this study did not consider fluid-rock geochemical reactions and CO<sub>2</sub> mineralization, a number of core-scale experiments show that carbonate minerals are likely to form in diffusion-dominated areas, where flow rates decrease (Adeoye et al., 2017; Luhmann et al., 2017b; Xiong et al., 2017a). For example, batch reactor experiments show that that carbon mineralization focuses on the dead-end of fractures, where advection is less dominant (Adeoye et al., 2017). In addition, both Luhmann et al. (2017a) and Andreani et al. (2009) found that mineral precipitation alters basalt fracture permeability in diffusion-controlled regions of a fracture. This relationship implies that carbon mineralization in basalt fractures may be self-reinforcing feedback in which fracture intersections initially decrease flow rates by relative permeability effects, thus encouraging mineral precipitation. These secondary alteration products decrease bulk fracture permeability, which further decreases flow rates, increases fluid residence time, and enhances mineralization. In the context of CCS, this feedback cycle suggests that basalt fracture networks may be self-sealing systems.

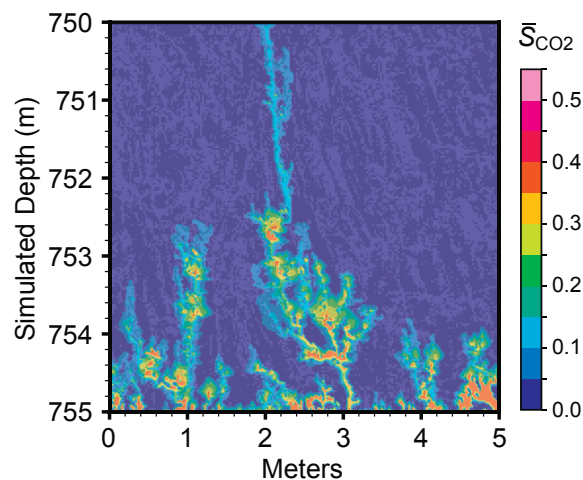
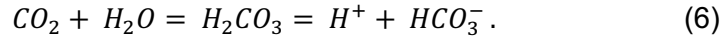


Figure 3.1: Monte Carlo simulation results from Gierzynski and Pollyea (2017) showing mean (N=50) CO<sub>2</sub> saturation after 10 years when CO<sub>2</sub> infiltrates the fracture network from below with 0.5 MPa of overpressure. This study shows that CO<sub>2</sub> tends to accumulate at fracture intersections because CO<sub>2</sub> mobility is inhibited due to relative permeability effects.

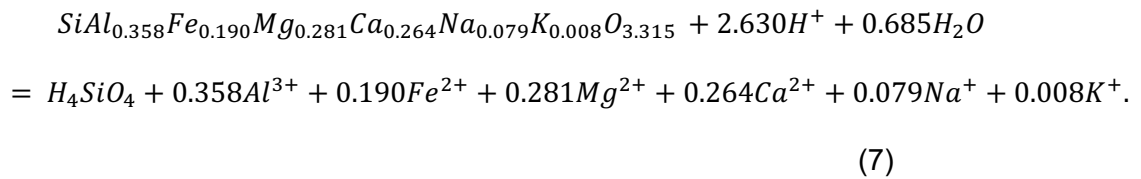
This study uses reactive transport modeling to test the aforementioned mineralization feedback. I model CO<sub>2</sub> infiltration into a synthetic basalt fracture and compare a case without porosity-permeability coupling (the nonlinear relationship of permeability change inside fracture due to porosity variation) to four cases with increasingly non-linear couplings. Results show that even weak porosity-permeability coupling dramatically increases CO<sub>2</sub> mineralization potential, while the stronger cases effectively seal the fracture network.

## 3.2 Fluid-Rock Geochemical Reactions for CO<sub>2</sub>-Water-Basalt

When free-phase CO<sub>2</sub> is injected into basalt reservoirs, the carbon mineralization process is characterized by a series of geochemical reactions. The first step is CO<sub>2</sub> dissolution into the aqueous phase, which dissociates carbonic acid into hydrogen and bicarbonate ions,



This reaction releases H<sup>+</sup> ion into solution, which decreases pH and drives basalt dissolution. The generalized dissolution reaction for Icelandic basalt is given by Oelkers and Gislason (2001) and Gudbrandsson et al. (2011) as,



This reaction consumes H<sup>+</sup> ion and releases divalent cations (Mg<sup>2+</sup>, Ca<sup>2+</sup>, Fe<sup>2+</sup>) into solution, which then react with the available bicarbonate ion to produce carbonate mineral species,



In addition to carbonate mineral phases, the Al and Si released during basalt dissolution react to form clay minerals (e.g., montmorillonite and illite). As secondary mineral alteration progresses, additional H<sup>+</sup> ion is released, which further drives basalt dissolution (Gysi and Stefánsson, 2012).

## 3.3 Methods

### 3.3.1 Conceptual Model

This study builds off the work of Gierzynski and Pollyea (2017), who developed a Monte Carlo numerical simulation of CO<sub>2</sub> leakage from a basalt disposal reservoir into the fracture network of an overlying basalt flow interior. The fracture geometry for their study was obtained from ground-based LiDAR scans of a flood basalt outcrop, and results show that the free-phase CO<sub>2</sub> accumulates at fracture intersections before diverging into branching fractures (Fig. 3.1). This phenomenon occurs because relative permeability effects decrease CO<sub>2</sub> mobility when a single flow path diverges into two or more branching fractures (Fig. 3.2). For example, Bertels (2001) found that relative permeability in a basalt fracture is highly interfering, thus small changes in non-wetting phase saturation cause significant changes in both wetting- and non-wetting phase permeability. As a consequence, CO<sub>2</sub> mobility in a basalt fracture is inhibited when a single flow path splits into one or more branching flow paths because the CO<sub>2</sub> saturation in each branch is substantially lower than that in the main trunk (Fig. 3.2). The implication of this relative permeability effect is that fluid residence time may increase at branching fractures, thus encouraging carbon mineralization reactions. However, Gierzynski and Pollyea (2017) focused solely on non-reactive multi-phase flow processes, so feedbacks between phase mobility, geochemical fluid-rock reactions, and permeability alteration remain an open question.

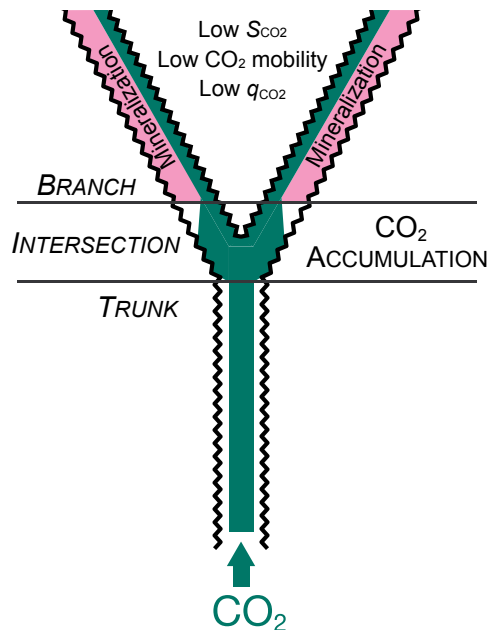


Figure 3.2: Conceptual model of gas-phase CO<sub>2</sub> flow in a branching fracture. The CO<sub>2</sub> mobility will decrease as a conductive fracture (trunk) diverges into two or more branching fracture.

These feedbacks are interrogated in the present study by simulating CO<sub>2</sub> infiltrating a synthetic basalt fracture that diverges into two branching fractures (Fig. 3.2). I implement reactive transport simulation to consider the competing effects of buoyancy (Wu et al., 2018) and permeability alteration that occurs as fracture porosity is reduced by precipitation of secondary mineral phases. In doing so, I evaluate feedbacks between carbon mineralization, porosity-permeability coupling, and CO<sub>2</sub> mobility, particularly in the context of their relationship to CCS efficacy in basalt formations. In addition, I test four porosity-permeability coupling models with non-linearly increasing coupling strength to evaluate the potential for a basalt fracture network to self-seal.

### 3.3.2 Domain and Boundary Conditions

The model domain for this study is based on generalized fracture geometry from Gierzynski and Pollyea (2017) that shows CO<sub>2</sub> tends to accumulate at fracture intersection when a single fracture splits into one or more branches (Fig. 3.1). The model domain for this study is a 2-D synthetic basalt fracture that rises 1.5 m from the base and branches at 45° (Fig. 3.3). The complete model domain is 2.5 m × 2.5 m with 10,000 grid cells that are discretized 0.025 m × 0.025 m. The fracture domain is modeled as a porous media equivalent with permeability of  $5.8 \times 10^{-16} \text{ m}^2$ , which represents mean basalt fracture permeability at depths ~750 m depth (Gierzynski and Pollyea, 2017). The van Genuchten (1980) relative permeability model is specified using parameters shown in Table 3.1, which result in highly interfering relative permeability effects. Unfractured basalt (matrix) permeability is specified as  $10^{-20} \text{ m}^2$  on the basis of literature values ranging between  $10^{-17}$  and  $10^{-24} \text{ m}^2$  (Bertels et al., 2001; Nara et al., 2011; Walker et al., 2013a, b).

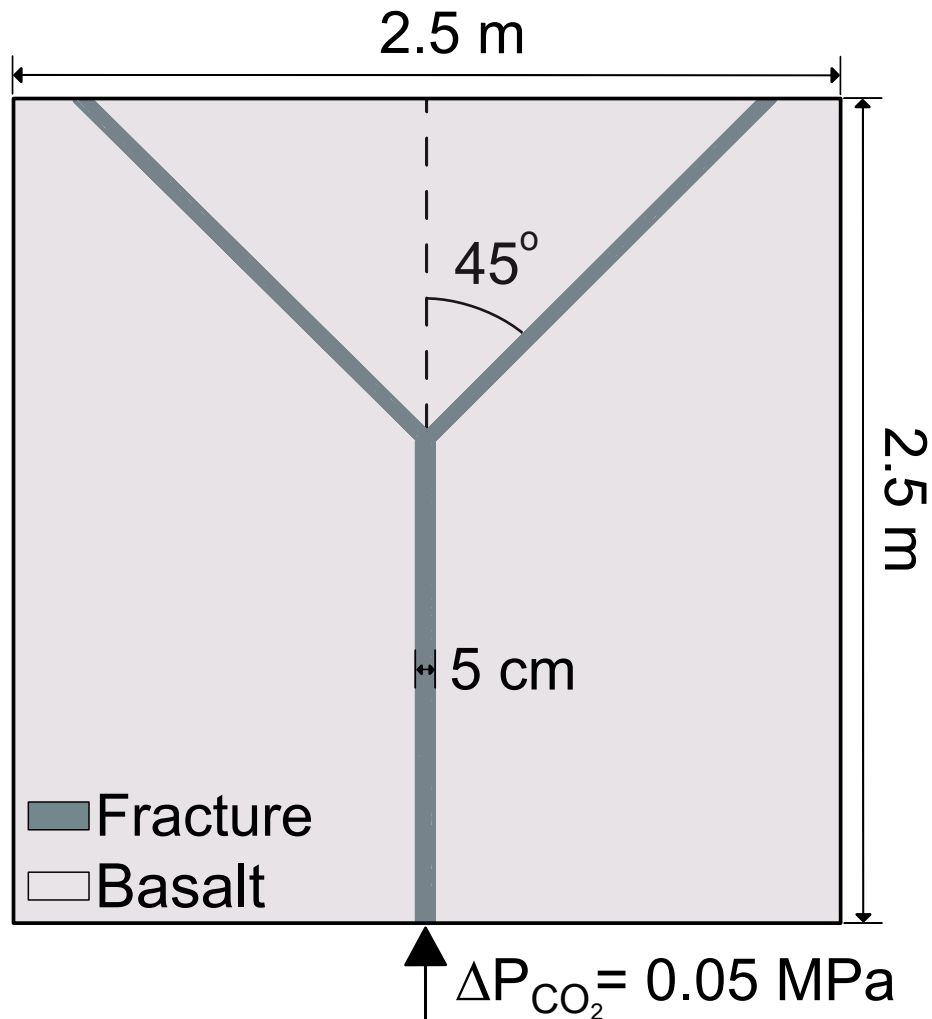


Figure 3.3: Model domain of this study is a 2.5 m × 2.5 m basalt fracture system with 10,000 grid cells that are discretized 0.025 m × 0.025 m, and one single fracture exists in the middle. The aperture of this fracture is 5 cm, and it diverges into two branching fractures at the height 2/5 of the model. The branching fractures diverging angle is 90° and basal boundary presents the CO<sub>2</sub> leakage condition by specifying a Dirichlet condition as fully saturated with CO<sub>2</sub> at 0.05 MPa over pressure.

The model scenario considers free-phase CO<sub>2</sub> migrating upwards from a disposal reservoir into the overlying basalt flow interior, i.e., reservoir leakage. To facilitate this scenario, initial conditions are specified as 7.5 MPa and 33°C, which corresponds with a depth of ~750 m, and free-phase CO<sub>2</sub> enters the fracture from below with 0.05 MPa of overpressure. Lateral boundaries are adiabatic (no flux) and the top boundary is open (Dirichlet) to allow mass and heat

in or out of the system. The remaining hydraulic and thermal properties are shown in Table 3.1. The code selection for this study is TOUGHREACT v3.2-OMP, which couples the governing equations for multi-phase and multi-component CO<sub>2</sub>-water-NaCl fluid flow, heat flow, and fluid-rock geochemical reactions, and secondary mineral alteration (Xu et al., 2014). I also consider the effects of dynamically changing porosity from basalt dissolution and secondary mineral precipitation, and, in doing so, this study reproduces the model scenario for five unique porosity-permeability relations.

Table 3.1. Bulk reservoir properties used in this model

<i>Reservoir properties</i>			
Property	Symbol	Value	Units
Fluid Pressure	$P_f$	75	MPa
Temperature	T	33	°C
Salinity	$C_{NaCl}$	10,000	ppm
Permeability (basalt)	$k_b$	$10^{-20}$	m <sup>2</sup>
Permeability (fracture)	$k_f$	$5.78 \times 10^{-16}$	m <sup>2</sup>
Porosity (basalt)	$\phi_b$	0.05	-
Porosity (fracture)	$\phi_f$	0.10	-
Density	$\rho_r$	2950	kg m <sup>-3</sup>
Specific heat	$C_p$	840	J (kg K) <sup>-1</sup>
Thermal conductivity	$\kappa_r$	2.11	W (m K) <sup>-1</sup>

<i>Relative permeability model</i>			
Property	Symbol	Value	Units
van Genuchten fitting parameter	$\lambda$	0.457	-
Residual liquid saturation	$S_{lr}$	0.3	-
Saturated liquid saturation	$S_{ls}$	1.0	-
Residual gas saturation	$S_{gr}$	0.25	-

### 3.3.3 Reactive Transport

During CCS in basalt reservoirs, CO<sub>2</sub> dissolution in water drives carbon mineralization via fluid-rock geochemical reactions in two steps: (i) basalt dissolution and (ii) mineral precipitation. In the context of Equation 7, the rate of basalt dissolution is equivalent to the rate of silica release ( $J_{si}$ ),

$$J_{si} = k a_{H^+}^n = (A e^{-1000 E_a / RT}) a_{H^+}^n, \quad (9)$$

where  $k$  is the rate constant (mol m<sup>-2</sup> sec<sup>-1</sup>),  $a_{H^+}$  is the hydrogen ion activity,  $n$  is the reaction order,  $A$  is the pre-exponential for the Arrhenius equation (mol m<sup>-2</sup> sec<sup>-1</sup>),  $E_a$  is activation energy (kJ mol<sup>-1</sup>),  $R$  is the gas constant (J mol<sup>-1</sup> K<sup>-1</sup>), and  $T$  is the temperature (K). Equation 9 shows that basalt dissolution is controlled primarily by temperature and pH (Gudbrandsson et al., 2011), and this study implements rate equations developed by Pollyea and Rimstidt (2017). These rate equations are based on the formulation used in Palandri and Kharaka (2004), which considers the overall dissolution rate to be the sum of independent parallel reactions that are affected only by temperature and pH. In this formulation, the rate constant ( $k$ ) is given as,

$$k = k_{25}^{nu} \exp \left[ \frac{-E_a^{nu}}{R} \left( \frac{1}{T} - \frac{1}{298.15} \right) \right] + k_{25}^H \exp \left[ \frac{-E_a^H}{R} \left( \frac{1}{T} - \frac{1}{298.15} \right) \right] a_{H^+}^{n_H} \\ + k_{25}^{OH} \exp \left[ \frac{-E_a^{OH}}{R} \left( \frac{1}{T} - \frac{1}{298.15} \right) \right] a_{OH}^{n_{OH}} \quad (10)$$

where subscript 25 denotes the reaction rate at 25 °C, superscript  $nu$  denotes the reaction rate for pure water at near neutral pH, and the superscripts  $H$  and  $OH$  denote the reaction rates at high and low pH, respectively. Pollyea and Rimstidt (2017) fit the linearized version of Equation 9 to whole-rock basalt dissolution data from the literature (Gudbrandsson et al., 2011) and found that the rate of crystalline basalt dissolution (Eq. 7) reaches a minimum at pH 6 without an apparent near-neutral rate plateau, thus the first term on the right side of Equation 10 goes to zero. The remaining terms in Equation 10 were parameterized by Pollyea and Rimstidt (2017) for modeling whole-rock basalt dissolution (Eq. 7) in TOUGHREACT v3.2-OMP. These rate

equations are valid for the pH and temperature range: 2 < pH < 12 and 0 °C < T < 100 °C with the corresponding parameters listed in Table 3.2.

Table 3.2. Parameters for rate equation

	$\log k_{25^\circ}$	$E_a$	n	R
pH < 6	-6.15	40.1	-0.680	8.314 (J/mol K)
pH > 6	-11.83	32.9	0.286	8.314 (J/mol K)

The second step of CO<sub>2</sub>-water-basalt reactions is mineral precipitation. The alteration products for this study include carbonate phases (calcite, magnesite, siderite), clay (montmorillonite, illite), and amorphous silica (Table 3.3). Because basalt dissolution is known to be the limiting step in carbon mineralization, I model the precipitation of these secondary alteration products on the basis of local equilibrium. The thermodynamic database utilized for these reactions is based on Thermodemm v.1.10 (Blanc et al., 2012) and modified by Pollyea and Rimstidt (2017) to include solubility constants for whole-rock basalt dissolution (Eq. 7).

Table 3.3. Minerals in this model

Minerals
Crystal Basalt
Calcite
Magnesite
Siderite
Montmorillonite (MgCa)
Illite(FeII)
Amorphous silica

### 3.3.4 Permeability Alteration

Dissolution and precipitation reactions alter the pore space of the fracture network, which in turn affects its effective porosity and permeability. Among the principal open questions in basalt sequestration is how permeability is affected by the rapid precipitation of secondary mineral phases. For a parallel-plate fracture, uniformly distributed mineral precipitation decreases permeability ( $k$ ) as the product of initial permeability ( $k_i$ ) and the cube of the ratio of porosity ( $\phi$ ) to initial porosity ( $\phi_i$ ),

$$k = k_i \left(\frac{\phi}{\phi_i}\right)^3. \quad (11)$$

This porosity-permeability relationship is commonly known as the *cubic law* (Fig. 3.4A); however, Schaef et al. (2011) found calcite precipitation in the CO<sub>2</sub>-water-basalt system forms a variety of discrete round nodules that suggests uniform scaling of the fracture wall is unlikely (Fig. 3.4B). Similarly, Xiong et al. (2017b) discovered that carbonate minerals are distributed unevenly along a basalt fracture. In addition, they found that some carbonate precipitates bridged the fracture due to the large size (Fig. 3.4C). These results suggest that the parallel-plate cubic law may underestimate the degree to which permeability is affected by carbon mineralization reactions. For example, the formation of nodules protruding from the fracture wall may cause substantially lower fracture permeability for relatively small changes in porosity. And for the extreme case in which alteration products form a discrete bridge across a fracture, the permeability may approach nil, thus sealing the fracture, for very low porosity changes (Fig. 3.4C). To account for these phenomena, I invoke a modification of the Verma and Pruess (1988) porosity-permeability model that frees the exponent of the cubic law to facilitate stronger porosity-permeability coupling,

$$k = k_i \left(\frac{\phi}{\phi_i}\right)^n. \quad (12)$$

For this study, I simulate reactive CO<sub>2</sub> flow for five individual simulations such that the exponent  $n$  in Equation 12 is 0, 3, 6, 9, and 15. The case where  $n$  equals 0 corresponds with no

porosity-permeability coupling; the case for  $n = 3$  is the well-known cubic law; and the cases for  $n$  equals 6, 9, and 15 represent systematically stronger porosity-permeability couplings. As a result, the simulations consider permeability to be a dependent variable that changes dynamically on the basis of initial porosity and changes caused by the molar volume of dissolving basalt and precipitating alteration products.

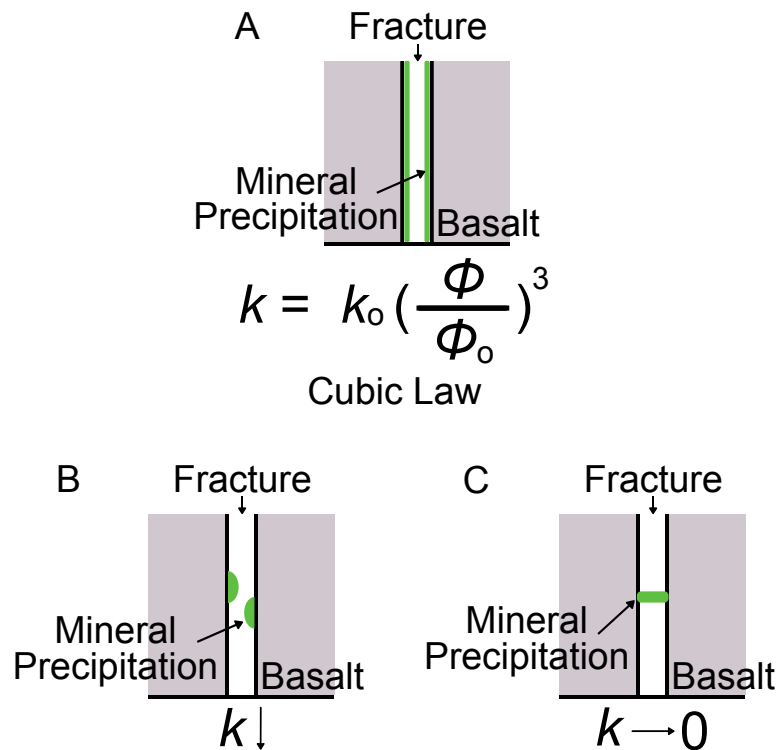


Figure 3.4: Different types of mineral precipitation inside a fracture system. Figure A presents the situation of evenly parallel distribution of minerals precipitation along the wall of the fracture and, the ratio of the permeability decrease is a cube of the porosity change, which is characterized by *cubic law*. In figure B the mineral precipitation forms a variety of discrete round nodules along the fracture wall and, the fracture permeability decreases largely compared to the cubic law case. Figure C illustrates the situation that mineral precipitation bridges the fracture and causes extremely fracture permeability decrease with minimal porosity changes.

## 3.4 Results and Discussion

Simulation results are presented with respect to the strength of the porosity-permeability ( $\phi$ - $k$ ) coupling, i.e., the  $n$  exponent in Equation 12. Figure 3.5 presents the results of CO<sub>2</sub> saturation and volume fraction of two minerals, calcite and montmorillonite, in the fracture after 10 years of CO<sub>2</sub> leakage at 0.05 MPa overpressure. Figure 3.6 illustrates the permeability change in the fracture as a result of CO<sub>2</sub>-water-basalt reactions after 10 years. The temporal change of free-phase CO<sub>2</sub> mobility is presented as Darcy flux in Figure 3.7 for different positions within the fracture, and the corresponding temporal change in permeability is shown in Figure 3.8.

### 3.4.1 Mineral Precipitation and Fracture Permeability Change

Results from this study show that secondary mineral precipitation is widespread in each simulation, and I find that calcite and montmorillonite are the most abundant mineral phases on the basis of equilibrium solubility constraints (Fig. 3.5), but magnesite, siderite, illite, and amorphous silica also form in lower abundance (Appendix Fig. A.1). These results are generally congruent with Matter et al. (2016), which shows that the calcite was the most abundant alteration product during carbon mineralization at the CarbFix pilot project in Iceland because of the small solubility product of calcite among the carbonate minerals and the large content of Ca<sup>2+</sup> released from basalt dissolution. I note here that ankerite was the dominant alteration product at the Wallula test site.

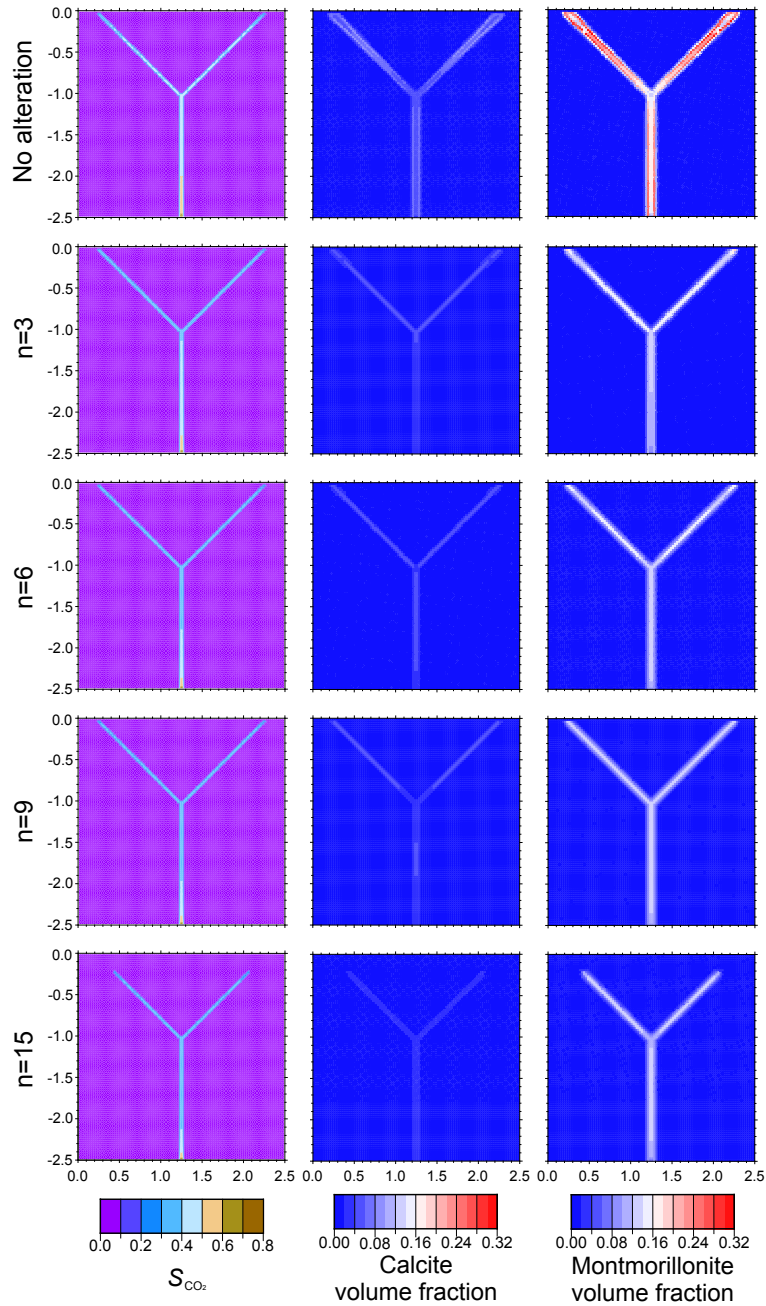


Figure 3.5: Simulation results after 10 years of CO<sub>2</sub> leakage at 0.05 MPa overpressure. Left column shows CO<sub>2</sub> saturation. Middle and right columns show the volume fraction of calcite and montmorillonite, respectively, that precipitate during the simulation. Each row corresponds with the strength of porosity-permeability coupling as described by the  $n$  exponent in Equation 12.

Simulation results for each model scenario show that free-phase CO<sub>2</sub> generally reaches saturation levels of  $\sim 0.8$  at the fracture base but varies substantially in the fracture branches depending on the strength of the  $\phi$ - $k$  coupling. In particular, the scenario without  $\phi$ - $k$  coupling

shows that CO<sub>2</sub> saturation in the fracture branches reaches ~0.4 after 10 years (Fig. 3.5, upper left panel). In contrast, the cases that dynamically alter permeability as a function of porosity (Eq. 12) show that CO<sub>2</sub> saturation is systematically lower as the strength of porosity-permeability coupling increases. I also find that all CO<sub>2</sub> remains in the fracture after 10 years of leakage for the case in which  $n$  equals 15 (Fig. 3.5, lower left panel). In general, these behaviors demonstrate that vertical CO<sub>2</sub> migration is highly sensitive to the strength of the porosity-permeability relationship.

These results also find that the relationship between CO<sub>2</sub> saturation in the fracture and secondary mineral abundance varies inversely with the strength of the  $\phi$ - $k$  coupling. When there is no permeability alteration, the volume fractions of montmorillonite and calcite reach ~0.3 and 0.1, respectively. This occurs because the absence of permeability alteration maintains higher CO<sub>2</sub> flow rates, which facilitates an equilibrium supply of hydrogen ion to drive basalt dissolution and mineral precipitation. In contrast, the volume fraction of calcite and montmorillonite decreases substantially as the  $\phi$ - $k$  coupling becomes stronger because less CO<sub>2</sub> is allowed into the system, which provides less hydrogen ion to drive basalt dissolution.

In the context of fracture geometry, mineralization is most prevalent in the fracture branches for all  $\phi$ - $k$  coupling scenarios, while considerably very less precipitation occurs at fracture intersections. For example, precipitation of calcite is most abundant in the fracture branches for the  $n=0$  case; however, it is also apparent that calcite is abundant within matrix grid cells that are adjacent to the fracture. When permeability alteration is simulated, calcite abundance decreases as the strength of the porosity-permeability coupling increases (Fig. 3.5). These results generally support the hypothesis that the mineral precipitation focuses downgradient from fracture intersections.

To evaluate the degree to which mineralization alters fracture permeability, Figure 3.6 illustrates the change in bulk the fracture permeability as a function of the strength of the  $\phi$ - $k$  coupling. Note that the scenario for  $n=0$  is not shown in Figure 3.6 because there is no

permeability alteration. For the parallel-plate ( $n=3$ ) scenario, permeability decreases by a factor of  $\sim 1 \times 10^{-5}$  along the fracture walls; however, the conductive portion of the fracture maintains its original permeability. This permeability alteration pattern matches the mineralization patterns illustrated in Figure 3.5. As the strength of the  $\phi$ - $k$  coupling increases, permeability exhibits substantial reductions. And for the case where  $n=15$ , permeability decreases by a factor of  $\sim 1 \times 10^{-10}$  along the fracture walls and  $\sim 1 \times 10^{-5}$  in along conductive portion of the fracture. Interestingly, these results also show that permeability alteration is generally lower at fracture intersections for all cases where  $n>0$ . This phenomenon occurs because relative permeability effects cause the free-phase CO<sub>2</sub> to accumulate at fracture intersections, which inhibits basalt dissolution, and thus mineral precipitation.

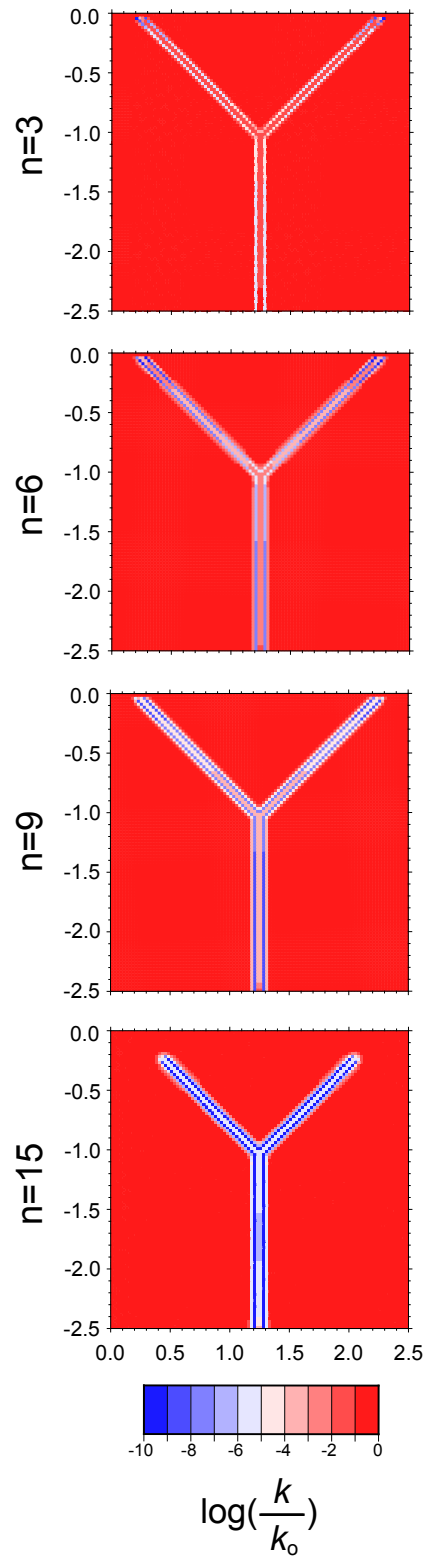


Figure 3.6: Change in permeability within the fracture for each porosity-permeability model after 10 years of CO<sub>2</sub> leakage at 0.05 Mpa overpressure. For each panel,  $n$  corresponds with the strength-of-coupling exponent in Equation 12.

The results presented herein Figure 3.6 illustrate that permeability decrease focuses along the wall of fracture regardless of the permeability alteration exponent. Stockmann et al. (2008) developed batch experiments of diopside dissolution in acid water and observed the calcite precipitation formed at the diopside surface. However, experimental results indicate that secondary mineral surface precipitation blocks the reactive surface area and decreases the dissolution rate (Hövelmann et al., 2012; Andreani et al., 2009). In this study, the disadvantage of this behavior is that the dissolution rate of basalt reduces with time because as the mineral precipitation occurs along the fracture wall, the surface area for basalt dissolution decreases, resulting in fewer cations and anions in the solution for mineral precipitation (Wells et al., 2017).

While the results for model scenarios with  $\phi$ - $k$  coupling strength of  $n=3$ , 6, and 9 show similar permeability alteration patterns, the model scenario with  $n=15$  is unique because the permeability alteration pattern is uniform throughout the fracture system. This phenomenon occurs because permeability decreases substantially as mineral alteration products begin to form. As a consequence, CO<sub>2</sub> mobility decreases dramatically, and the permeability alteration pattern appears to migrate contemporaneously with CO<sub>2</sub> migration through the fracture. This phenomenon is apparent by comparing the permeability alteration pattern in Figure 3.6 (bottom panel) with the CO<sub>2</sub> saturation pattern in Figure 3.5 (bottom left). Moreover, the results show that no CO<sub>2</sub> has left the model through the upper boundary after 10 years of simulation, which suggests that strong  $\phi$ - $k$  coupling may result in a self-sealing fracture network.

### 3.4.2 Spatial and Temporal Fracture Permeability Alteration

In order to evaluate the relationship between CO<sub>2</sub> mobility and permeability alteration in the basalt-water-CO<sub>2</sub> system, Figure 3.7 presents time-series CO<sub>2</sub> saturation and Darcy flux for six positions within the fracture. For discussion, these locations are referred to as base, trunk,

intersection, low, middle, and high branch. The base location is the bottom of the fracture, where CO<sub>2</sub> enters into the system, so time series results from this location can be interpreted as the leakage signal into the fracture network from the underlying reservoir.

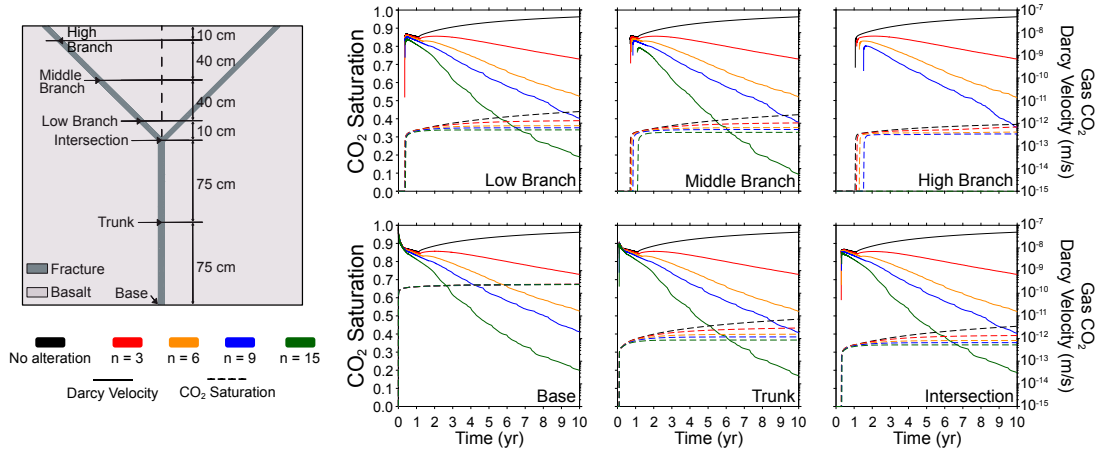


Figure 3.7: Left figure presents the six control positions along the fracture. Right figure presents the CO<sub>2</sub> saturation and gas-phase CO<sub>2</sub> Darcy velocity at different positions with different permeability alteration exponents.

From a temporal perspective, the overall pattern is that CO<sub>2</sub> mobility (as measured by Darcy flux) decreases systematically over time for all model scenarios that account for permeability alteration by  $\phi$ - $k$  coupling; however, the CO<sub>2</sub> mobility increases over time for the model without  $\phi$ - $k$  coupling (Fig. 3.7). For this latter model scenario ( $n=0$ ), the phenomenon in which CO<sub>2</sub> mobility initially decreases and then increases through time (Fig. 3.7, black curves) caused by relative permeability effects. When CO<sub>2</sub> initially enters the fracture, the relative permeability available to CO<sub>2</sub> is low because basalt fractures are known to exhibit highly interfering relative permeability behavior (Bertels, 2001). This causes the CO<sub>2</sub> mobility to remain low; however, relative permeability increases over time as more CO<sub>2</sub> enters the fracture, the result of which increases CO<sub>2</sub> mobility over time. This phenomenon is also apparent for the cubic  $\phi$ - $k$

coupling scenario (n=3), but bulk permeability loss from mineralization overwhelms the relative permeability effects in less than a year (Fig. 3.7, red curves). At the other end of this spectrum, the strongest  $\phi$ -k scenario (n=15) shows that CO<sub>2</sub> mobility decreases up to six orders of magnitude over the 10-year model scenario.

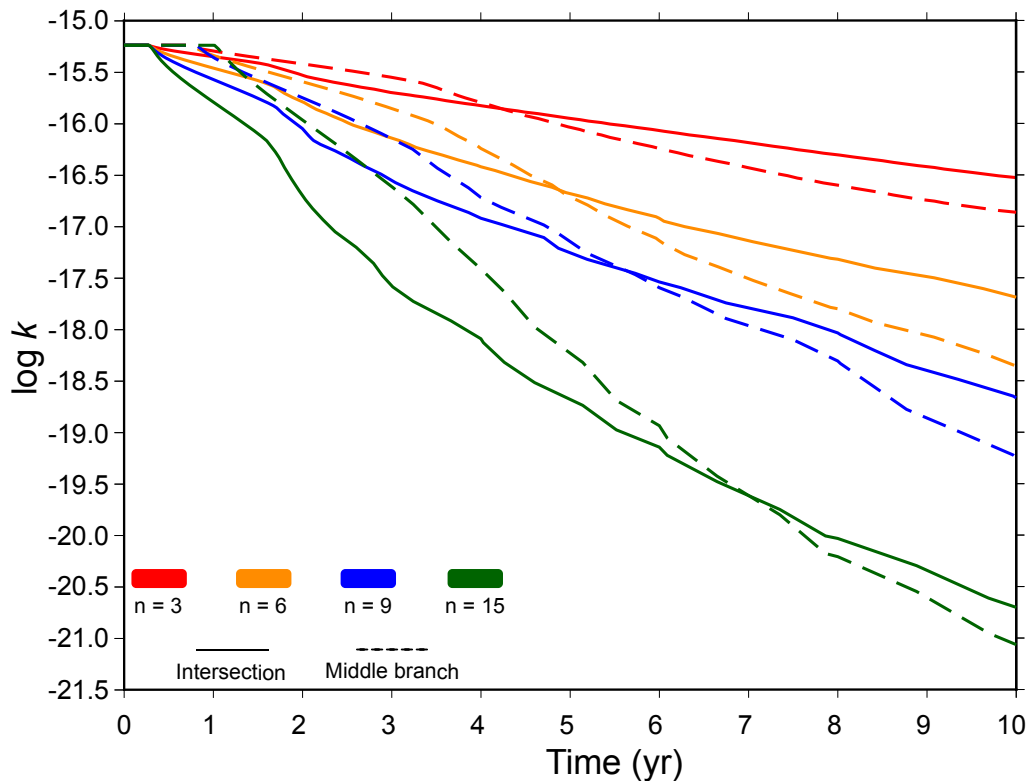


Figure 3.8: Time series of fracture permeability change at fracture intersection and middle branch with different permeability alteration exponents.

Considering CO<sub>2</sub> mobility at various positions within the fracture network shows little variation within each scenario, except for the strongest  $\phi$ -k coupling (n=15). The scenarios with little spatial variation in CO<sub>2</sub> mobility along the fracture are congruent with the well-known phenomenon that fracture flow is controlled by the smallest opening available for flow. However, the n=15 scenario shows up to an order of magnitude variation in CO<sub>2</sub> mobility throughout the flow path. For this scenario, the CO<sub>2</sub> mobility decreases systematically in the downgradient

direction of flow and goes to nil at the high branch monitoring location because CO<sub>2</sub> has not reached this location after 10 years. This flow rate reduction behavior occurs because mineral precipitation, and this permeability alteration, focus in the middle branch regions of the fracture system. This phenomenon occurs with the weaker  $\phi$ - $k$  coupling scenarios, but it is substantially less pronounced.

For this modeling study, decreasing CO<sub>2</sub> mobility is driven primarily by permeability alteration in the fracture. The temporal change in permeability is shown in Figure 3.8 at the fracture intersection and middle branch for each model scenario with  $\phi$ - $k$  coupling. The range of permeability alteration ranges from ~2 orders of magnitude for the parallel-plate ( $n=3$ ) model and more than 5 orders magnitude for the  $n=15$  scenario. For each of these model scenarios, permeability reduction occurs first at the fracture intersection because this location receives the first exposure to CO<sub>2</sub> (Fig. 3.8, solid lines). However, once mineralization occurs in the middle branch, the resulting permeability alteration takes place at a faster rate, and within 10 years, the overall permeability loss in the middle branch exceeds permeability losses at the intersection, for all model scenarios. This tendency for permeability alteration to eventually focus in the middle branch occurs because the CO<sub>2</sub> mass is halved when flowing into the fracture branches from the main trunk. As a consequence, the relative permeability is lower in the branches, which slows the mobility of both free-phase CO<sub>2</sub> and the aqueous phase. This increases residence time for the aqueous phase and encourages mineral alteration in the fracture branch. These relative permeability effects also encourage CO<sub>2</sub> to accumulate at the fracture intersection, which inhibits fluid-rock interaction.

### 3.4.3 Mass Balance

Geologic CO<sub>2</sub> sequestration in basalt formations is predicated on rapid CO<sub>2</sub> mineralization (McGrail et al., 2006). At the CarbFix site in Iceland, pilot-scale injections of aqueous phase CO<sub>2</sub>

found that more than 95% of the injected carbon mass was mineralized within in less than two years (Matter et al., 2016). These latter calculations were based on mass balance calculations between dissolved organic carbon and <sup>14</sup>C tracer, which found substantial reductions in both along the flow path within the target reservoir. For this to occur, the most plausible mechanism is the formation of carbonate minerals. Although similar testing was not performed at the Wallula site in Washington State, USA, where free-phase CO<sub>2</sub> was injected at ~750 m depth, analysis of post-injection sidewall cores from the borehole found that carbonate minerals (primarily ankerite) were widespread (McGrail et al., 2017). To assess the relationship between permeability alteration and mineralization potential in the present, I consider the mass balance of carbon and its distribution among the solid, aqueous, and gas phases.

The models developed here assume no carbon prior to CO<sub>2</sub> infiltration, thus balancing the carbon mass provides a straightforward assessment of the carbon storage potential as a function of the  $\phi$ - $k$  coupling strength. In this model, CO<sub>2</sub> enters the fracture from below as a supercritical fluid, and, as it rises, may also exist in the aqueous phase CO<sub>2</sub> (i.e., CO<sub>2</sub> dissolved in water) and/or carbonate mineral phases, the latter of which are calcite, magnesite, and siderite. In addition, CO<sub>2</sub> may leave the model through the upper boundary; however, the TOUGHREACT code treats Dirichlet boundaries as grid cells with semi-infinite volume. As a result, the total carbon mass in the upper boundary cells represents CO<sub>2</sub> leakage out of the fracture. The carbon balance for each model scenario is presented in Table 3.4.

Table 3.4. Distribution of different phases of CO<sub>2</sub> and carbon mineralization ratios with different permeability alteration exponents

	n = 0	n = 3	n = 6	n = 9	n = 15
	C	C	C	C	C
	(mole)	(mole)	(mole)	(mole)	(mole)
Mineral	62.5	30.5	31.6	31.8	27.2
Aqueous	4.51	2.04	2.16	2.21	2.09
Gas	1.53	0.54	0.44	0.44	0.43
Boundary <sup>†</sup>	40.91	4.57	1.20	0.4	-
Total	109.45	37.65	35.40	34.85	29.72
Mineralization Ratio	57%	81%	89%	91%	91%

<sup>†</sup> Sum of gas and aqueous phase carbon (as CO<sub>2</sub>) that passed through the model domain into the upper boundary.

The mass balance calculations in Table 3.4 shows the molar abundance of carbon for each permeability alteration scenario, along with the mineralization ratio, which is the ratio of moles of carbon transformed into carbonate minerals to moles of carbon introduced into the fracture. These calculations show two distinct patterns. First, the model scenario with no permeability comprises a mineralization ratio of 57% after 10 years of CO<sub>2</sub> flow into the fracture. In contrast, the model scenarios with permeability alteration mineralize 81% to 91% of the total CO<sub>2</sub> mass, which is generally congruent with the 95% mineralization rate reported for the CarbFix project (Matter et al., 2016). The discrepancy is likely a result of the models considering free-phase CO<sub>2</sub>, which is buoyant in comparison to reservoir fluids; whereas, aqueous phase CO<sub>2</sub> injections at CarbFix result in a higher density fluid that will tend to sink. For the model scenarios that simulate permeability alteration, the underlying pattern is that stronger  $\phi$ - $k$  coupling leads to (i) systematically higher mineralization ratios and (ii) systematically lower CO<sub>2</sub> mass. The reason that higher  $\phi$ - $k$  coupling strength leads to lower CO<sub>2</sub> entering the fracture is because the model scenario is based on a hypothetical scenario in which a free-phase CO<sub>2</sub> plume is juxtaposed

below low-permeability basalt flow interior with 0.5 MPa overpressure. For a fixed overpressure, the rate of CO<sub>2</sub> flow entering the fracture is a function of permeability, which decreases faster for stronger  $\phi$ - $k$  coupling and permits less CO<sub>2</sub> to enter the overlying confining unit.

Perhaps the most significant result to come from this study is that the total CO<sub>2</sub> mass entering the fracture varies by ~26% across all model scenarios with  $\phi$ - $k$  coupling (Table 3.4). In contrast, the total CO<sub>2</sub> mass entering the fracture varies by ~190% between the model scenario without permeability alteration ( $n=0$ ) and the model scenario with weak  $\phi$ - $k$  coupling ( $n=3$ ). This broad disparity demonstrates that permeability alteration plays a fundamental role in calculations to estimate CO<sub>2</sub> storage potential and leakage potential in mafic reservoirs. And while empirical models of fracture-controlled permeability alteration in natural geologic systems remain elusive, the general  $\phi$ - $k$  coupling model implemented for this study (Verma & Pruess, 1988) demonstrates that errors in the  $\phi$ - $k$  coupling model are likely to be much lower than errors introduced by omitting geochemical permeability alteration.

### 3.5 Conclusion

Geologic carbon storage in basalt reservoirs is a promising strategy for expanding the geographic footprint of carbon capture and sequestration technology. Although recent basalt CCS projects in Iceland and Washington State, USA have shown rapid mineralization at field scales, there remains substantial uncertainty in the dynamics of carbon mineralization at the scale of an individual fracture. Recent research shows that relative permeability effects may cause free-phase CO<sub>2</sub> to accumulate at fracture intersections (Gierzynski & Pollyea, 2017); however, the relationship between this phenomenon and CO<sub>2</sub> mineralization have yet to be explored. Following the outcrop-scale study by Gierzynski and Pollyea (2017), the current study tests the hypotheses that: (1) secondary mineral precipitation focuses on the branching fracture and (2) such mineralization decreases permeability in a manner that may result in a self-sealing fracture

network. These hypotheses are tested using reactive transport simulation of CO<sub>2</sub> infiltrating a meter-scale, synthetic basalt fracture system from below when permeability is coupled to porosity, and porosity varies dynamically as a function of molar volume changes due to mineralization and precipitation. Conclusions from this study are summarized as:

1. Carbonate and clay minerals focus at the branching fractures, where the system is dominated by diffusion. The larger permeability alteration exponent, the less mineral precipitation that occurs within the fracture. Moreover, fracture permeability reduction is caused by mineral precipitation mostly along the fracture wall.
2. Vertical gas-phase CO<sub>2</sub> migration is inhibited by mineral precipitation, which causes fracture permeability to decrease. When modeling CO<sub>2</sub> storage in a basalt reservoir, permeability alteration is critically important to account for on the basis for quantifying the amount of CO<sub>2</sub> that is sequestered and leaked.
3. For strong  $\phi$ - $k$  coupling, the large carbon mineralization ratio proves the fracture system may be self-sealing due to secondary mineral precipitation. Errors in the different  $\phi$ - $k$  coupling models are comparatively small compared to errors introduced by permeability alteration neglect.

This study provides a better understanding of mineral precipitation within fractures and illustrates the important effect of fracture permeability alteration to CO<sub>2</sub> migration. In addition, the mineral precipitation prevents the gas phase CO<sub>2</sub> leakage through the fracture zone. Permeability alteration should be considered when modeling the CO<sub>2</sub> sequestration in basalt reservoirs.

# Chapter 4

## Machine Learning Applied to Parametric Analysis of CO<sub>2</sub> Migration

### 4.1 Introduction

Anthropogenic CO<sub>2</sub> emissions are strongly implicated in increasing global temperatures, and carbon capture and sequestration (CCS) is considered as an engineering-based approach designed to reduce the total mass of atmospheric CO<sub>2</sub> released from point source generators (Metz et al., 2005; Michael et al., 2010; Sharma, 2011; Viebahn et al., 2014; Viebahn et al., 2015). Many potential geological formations have been proposed for anthropogenic CO<sub>2</sub> emission storage (Bennion and Bachu, 2005; Dai et al., 2013; Herzog et al., 1991). Among them, deep brine aquifers are of special interest because of their widespread worldwide distribution (Shi et al., 2011) and large storage capacity (Iglauer et al., 2011). A successful CCS project is dependent on whether or not the injected CO<sub>2</sub> can be stored in the reservoir safely over a long-time period (Metz et al., 2005; Shaffer, 2010).

During CO<sub>2</sub> injection and trapping processes, uncertainties associated with reservoir properties and geologic conditions affect the distribution and migration of CO<sub>2</sub>. For example, reservoir PTX (pressure, temperature, composition) conditions affect the thermodynamics of CO<sub>2</sub> dissolution (Jayne et al., 2019b; Bennion and Bachu, 2005), which in turn affects the saturation state that governs CO<sub>2</sub> plume geometry through capillary pressure (Wu et al., 2018) and relative

permeability (Pollyea, 2016; Pini et al., 2012) effects. In natural geologic systems, these phenomena are subject to substantial uncertainty, which affects not only the migration of CO<sub>2</sub> but also the fluid pressure perturbation (Pawar et al., 2017). As a result, the interactions between PTX-dependent fluid properties and multi-phase fluid dynamics require careful consideration during CCS projects assessment. To understand the mechanisms affecting CO<sub>2</sub> migration, numerous laboratory and modeling studies have been done to quantitatively characterize CO<sub>2</sub> behavior under different reservoir conditions (Ferrand and Celia, 1992; Chaouche et al., 1994; Ataie-Ashtiani et al., 2002; Arns et al., 2003). Wu et al. (2018) discovered the effect of substantial variability of capillary pressure measurements on supercritical CO<sub>2</sub> (scCO<sub>2</sub>) migration, and how this variability influences CO<sub>2</sub> plume geometry in a sandstone reservoir. In Pollyea (2016), the uncertainty of relative permeability effects was quantified in a basalt reservoir by performing numerical CO<sub>2</sub> injection simulations, and the results showed that the injection pressure accumulation and CO<sub>2</sub> plume geometry are affected by relative permeability as well. In addition, Jayne et al. (2019b) found that thermodynamic changes during CO<sub>2</sub> migration may cause a warming front of up to 4°C within the reservoir due to CO<sub>2</sub> dissolution, and that these thermodynamic changes can be used as a thermal monitor for predicting CO<sub>2</sub> breakthrough.

The migration of CO<sub>2</sub> and fluid pressure in geologic formations may cause leakage through abandoned wells and structural features, e.g., faults and fractures. As a result, the leakage of CO<sub>2</sub> not only reduces the storage efficiency but may also contaminate groundwater resources in shallow aquifers (Pawar et al., 2017). In order to assess the efficiency of CCS projects prior to the construction, it is essential to estimate the risk profile and evaluate reservoir performance (Pruess and García, 2002). The National Risk Assessment Partnership (NRAP), a U.S. Department of Energy initiative, has been pursuing research on leakage risk and reservoir performance for carbon sequestration. Many studies focus on the monitoring of CO<sub>2</sub> saturation and pressure propagation within the reservoir during injection for leakage risk estimation. More

importantly, fluid pressure and CO<sub>2</sub> saturation results can be used as inputs for the leakage estimation model to predict rates and volumes of CO<sub>2</sub> leakage (Bromhal et al., 2014). For example, Zhang et al. (2018) modeled the potential of fluid migration detection based on CO<sub>2</sub> saturation and pressure monitoring in the overlying seal layer, in which exists a high permeability zone. The results showed that pressure response resulting from CO<sub>2</sub> migration was detected up to 1650 m from the centroid of the high permeability zone in the sealing layer. In addition, the results from Jayne et al. (2019a) generated 50 stochastic permeability distributions in the basalt reservoir for CO<sub>2</sub> migration simulations. The results suggested that uncertainty in reservoir-scale permeability greatly impacts the accumulation and distribution of CO<sub>2</sub>. Besides CO<sub>2</sub> saturation and pressure detection, Yang et al. (2017) focused on groundwater pH as an index to monitor leakage detection because groundwater pH decreases due to CO<sub>2</sub> dissolution. The computed results showed that the probability of leakage detection is over 90% when the change in pH > 0.7.

Even though many laboratory and numerical studies have been done to study the migration mechanisms of CO<sub>2</sub> and pressure in the reservoirs, there are some disadvantages to these two methods. First, laboratory experiments are completed on core-scale rock samples, and upscaling laboratory results to field scale models arises uncertainties (Yu et al., 1998; André et al., 2014; Shi et al., 2011). In addition, even though some numerical studies present the effect of reservoir uncertainties on CO<sub>2</sub> migration, the physics-based simulations are complicated and computationally expensive (Mudunuru et al., 2020). Some studies have shown that reservoir-scale simulations require days to months of computer time (Bromhal et al., 2014; DeVries et al., 2017).

In recent years, machine learning (ML) has become an important tool for efficiently analyzing large amounts of data in a variety of fields. As high-fidelity data sets become increasingly available for applications in many areas, ML methods are becoming an important tool for analyzing these “big data” problems (Karpatne et al., 2019; Lary et al., 2016; Rouet-Leduc et al., 2017). For example, Karpatne et al. (2016) used different ML methods, such as multitask

learning and multi-instance learning, to estimate the amount of forest cover across four states in Brazil. These ML techniques showed good results in terms of the forest area. Similarly, Marjanović et al. (2011), tested the support vector machines (SVM) method for high-performance landslide susceptibility mapping processes. The SVM method outperformed decision trees and logistic regression methods in evaluation measurements, and it provided an application of machine learning method in landslide risk assessment. Among the most beneficial uses of ML methods is to reduce the computational cost of analyzing complex parameter spaces. For example, Smith et al. (2017) have applied neural networks to small organic molecules that span an immense space, so that the resulting models can predict the results of computationally intensive quantum-mechanical calculations at a much lower computational cost. For computational cost reduction in risk monitoring during CCS, Chen et al. (2018) utilized the ML algorithm called multivariate adaptive regression splines to derive reduced order models from physics-based numerical simulations of CO<sub>2</sub> injection in a saline aquifer. These reduced order models provide new insights for effective monitoring approaches about CO<sub>2</sub> leakage with substantially less computational overhead than traditional multi-physics numerical simulations.

The success of ML application in the geosciences is an outgrowth of the big data revolution that is transforming geosciences from a data-poor field to one with a wide variety of high-fidelity, multi-dimensional datasets (Bergen et al., 2019). The growing data availability opens up exciting new opportunities for the application of machine learning methods to problems in geosciences (Karpatne et al., 2019). The application of ML has shown outstanding performance in improving computational efficiency for subsurface simulations (Maniar et al., 2018; Srinivasan et al., 2019). For example, Valera et al. (2018) developed an alternative network reduction approach for fluid flow in a 3-D fracture-controlled fluid system by applying the ML method, and the computational time decreased from hours to seconds. This latter study belies the tremendous advantage in the application of ML methods, which its ability to rapidly process patterns of large-scale and/or high-

dimensional datasets, while efficiently capturing complex relationships between data and identifying previously inaccessible research targets. Importantly, this process also decreases personnel costs and offers time improving performance and reproducibility in comparison to human analysts (Bergen et al., 2019; Maniar et al., 2018). In subsurface fluid-flow reservoir simulations, the primary goal of ML applications is to make highly accurate predictions of fluid migration, while improving computational efficiency. In doing so, the purpose of ML methods is to find a set of weights that can map all input properties to their corresponding output variables, thus allowing for rapid predictions across all possible combinations of input parameters (Poulton, 2002). This process is also characterized as supervised learning, which is widely applied to physics-based problems (Srinivasan et al., 2019).

One widely used ML method is the artificial neural networks (ANN) algorithm, loosely based on simple models of neurons in the brain (Bishop, 1995). ANN algorithms, consisting of a set of neurons, aim to find a representation that maps input parameters to output variables (Bergen et al., 2019). ANN are widely used for capturing features of image data from large datasets and have shown excellent performance for reducing the dimensionality of data (Hinton and Salakhutdinov, 2006). ANN is suitable for processing data characterized by substantial variability by scaling features in the same range to avoid emphasizing on the peak values. As a result, ANN has become popular in the geosciences applications for modeling nonlinear relationships (Bergen et al., 2019). For example, Beucher et al. (2013) described the application of ANN for acid sulfate (AS) soil mapping to classify AS soil and non-AS soil sites. In addition, DeVries et al. (2017) accelerated the calculation of viscoelastic earthquake cycle activity by more than 50,000% applying extended ANN approach.

Monitoring the fluid flow migration mechanisms of CCS projects is critical to ensure CO<sub>2</sub> storage safety and efficiency. Physics-based, multi-phase flow models that account for thermodynamics of the CO<sub>2</sub>-brine system are frequently applied to understand the site-scale behavior of CCS projects. For example, Wu et al. (2018) and Pollyea (2016) used response

surface methods to gain insights into the effects of uncertainty in capillary pressure and relative permeability models, respectively, during industrial-scale CO<sub>2</sub> injections. However, in storage reservoirs, numerous physical properties affect CO<sub>2</sub> migration simultaneously. As a result, it is important to build a comprehensive understanding of the CO<sub>2</sub> migration mechanism under more realistic conditions. However, simulations that quantify realistic conditions of the fluid migration mechanism are computationally expensive and time consuming, requiring thousands of hours of computing time on a high-performance computing cluster. Recently, the application of ML has shown outstanding performance to speed up these simulations by capturing fundamental attributes, such as fluid pressure accumulation and CO<sub>2</sub> distribution. The objective of this study is to simultaneously constrain the effects of uncertainty in both capillary pressure and relative permeability models to scCO<sub>2</sub> plume shape and pressure perturbation during industrial-scale CCS in a generic sandstone reservoir. In doing so, deep ANN model of supervised ML is applied to capture the features of CO<sub>2</sub> saturation and pressure distribution profiles. The ML training process is based on 460 physics-based simulations describing different combinations of capillary pressure and relative permeability parameters. Afterward, the CO<sub>2</sub> saturation and pressure migration under unknown capillary pressure and relative permeability conditions are predicted. This study provides a better understanding of the increased computational efficiency of computational simulations of CO<sub>2</sub> sequestration achieved by ML application. In addition, the prediction results provide fundamental supports for future improvement in the siting process of CCS field reservoir applications.

## 4.2 Methods

Physics-based, multi-phase flow models are commonly used to understand the site-scale reservoir behavior of CCS projects, particularly in the context of risk management and CO<sub>2</sub>

storage efficiency. Among the principal challenges of reservoir-scale CCS models are representing multi-phase flow and transport properties, e.g., relative permeability and capillary pressure, which are often measured at lab scales. In reservoir-scale CCS models, relative permeability and capillary pressure effects are generally implemented using generic constitutive relationships that are parameterized functions of wetting phase saturation. To understand the relationship between parametrized constitutive equations and CCS reservoir performance, this study develops an ANN model to quantify the effects of parametric variability in the constitutive models governing both relative permeability and capillary pressure. The ANN model is developed using a physics-based simulation ensemble that tests a random sample of a three-dimensional parameter space. The physics-based simulation ensemble comprises 460 individual simulations each parameterized by random sampling the three-dimensional parameter space. The remainder of the section details the methodology for both the physics-based simulation ensemble and the ANN emulator.

### 4.2.1 Physical Model

The conceptual model is a hypothetical sandstone reservoir that is (i) regionally confined by low permeability caprock, e.g., shale, and (ii) occurs at depth ~2000 m, with 16 m thickness and 100 km lateral extent (Fig. 4.1). This model domain is a 3-D cylindrical volume, which is discretized as a 2-D system due to axial asymmetry. The injection well is completed in the center of the model domain with a radius of 0.1 m. Beyond the injection well, the model domain is discretized in the radial direction with 949 grid cells that increase logarithmically to a radial extent of 10,000 m. To simulate a semi-infinite far-field, the radial dimension is further discretized between 10,000 m and 100,000 m with 50 additional grid cells to ameliorate non-physical pressure feedbacks from the lateral boundary. Vertical grid discretization is 1 m. The upper and lower boundaries are specified as adiabatic (no flow) because CCS reservoirs are generally

confined by low permeability shale formations. The centrally located injection well is a Neumann type boundary, where CO<sub>2</sub> is being injected through injection well at a constant rate of 8.0 kg/s for ten years. Initial conditions are specified as fully saturated in the wetting phase, with fluid pressure of 20 MPa, and temperature of 75°C. These conditions reflect a disposal reservoir at ~2 km depth, where injected CO<sub>2</sub> exists as a supercritical phase fluid (scCO<sub>2</sub>). The hydraulic parameters are listed in Table 4.1.

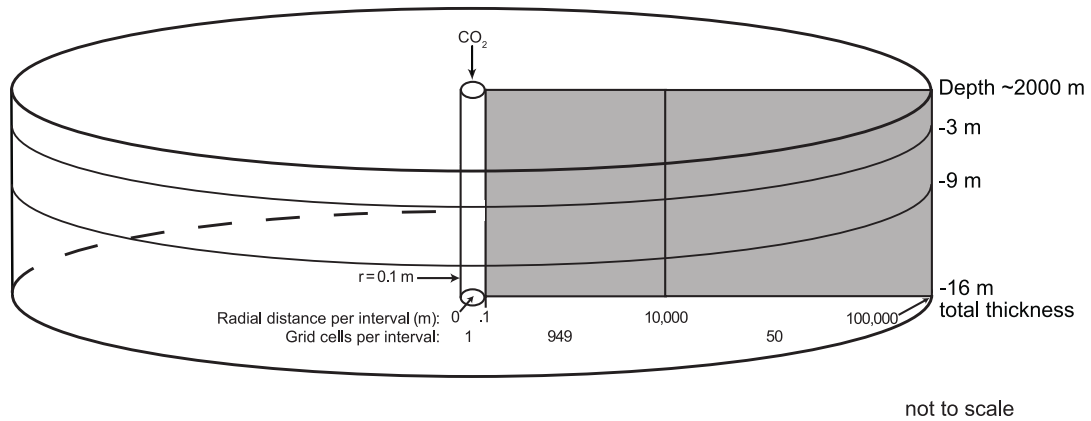


Figure 4.1: Two-dimensional symmetric model domain used in this study. The injection well is completed in the domain center with 0.1m radius, and the next 949 grid cells with logarithmically increasing to 10,000 m, after which 50 grid cells increasing logarithmically to 100,000 m. The thickness of this domain is 16 m with a constant 1 m grid cell interval. Supercritical CO<sub>2</sub> is being injected through the injection well at a rate of 8.0 kg/s (252,461 MT/year) for 10 years.

In this study, the effects of capillary pressure and relative permeability on CO<sub>2</sub> migration mechanisms in storage reservoirs are modeled using characteristic curves, i.e., constitutive models. Capillary pressure effects are calculated using the constitutive relation originally developed by van Genuchten (1980), models capillary pressure as a function of effective wetting phase saturation ( $S^*$ ) through the equation:

$$P_{cap} = -P_o([S^*]^{-\frac{1}{\lambda}} - 1)^{1-\lambda}. \quad (13)$$

In Equation 13,  $P_o$  is the entry pressure, which characterizes the pressure drop when gas phase first enters the pore network,  $\lambda$  is a fitting parameter (commonly called the phase interference

Table 4.1: Bulk reservoir properties used in this model

<i>Reservoir properties</i>			
Property	Symbol	Value	Units
Fluid Pressure	$P_f$	20	MPa
Temperature	T	75	°C
Salinity	$C_{NaCl}$	10,000	ppm
Permeability	$k$	$4 \times 10^{-13}$	m <sup>2</sup>
Porosity	$\phi$	0.2	-
Density	$\rho_r$	2038	kg m <sup>-3</sup>
Specific heat	$C_p$	1000	J (kg K) <sup>-1</sup>
Thermal conductivity	$\kappa_r$	1.6	W (m K) <sup>-1</sup>

parameter), which controls the curvature of the model, and  $S^*$  is the effective wetting phase saturation, which is calculated as:

$$S^* = \frac{S_l - S_{lr}}{S_{ls} - S_{lr}}. \quad (14)$$

In Equation 14,  $S_l$  is wetting phase saturation,  $S_{lr}$  is the residual wetting phase saturation, and  $S_{ls}$  is the saturated wetting phase saturation. These end member saturations represent conditions when (i) the wetting-phase is fully mobile ( $S_{ls}$ ) and (ii) the wetting phase is immobile ( $S_{lr}$ ). For this study,  $S_{ls}$  and  $S_{lr}$  are unity and 0.3, respectively.

Wetting phase relative permeability is calculated with the van Genuchten-Mualem model (van Genuchten, 1980), and it is given as:

$$k_w = \sqrt{S^*} [1 - (1 - S^{*\lambda})^\lambda]^2, \quad (15)$$

where  $\lambda$  is van Genuchten fitting parameter, and  $S^*$  is the effective wetting phase saturation (Eq. 14). Non-wetting phase relative permeability is calculated with Corey curve (Corey, 1954) as:

$$k_{nw} = (1 - \hat{S})^2 (1 - \hat{S}^2), \quad (16)$$

where  $\hat{S}$  is effective non-wetting phase saturation, and is represented as:

$$\hat{S} = \frac{S_l - S_{lr}}{1 - S_{lr} - S_{gr}}. \quad (17)$$

In Equation 17,  $S_l$ , and  $S_{lr}$  are wetting phase saturation and residual wetting phase saturation (Eq. 14), and  $S_{gr}$  is residual non-wetting phase saturation when fully immobile. In this formulation for relative permeability,  $S_{gr}$  governs curvature of the non-wetting phase relative permeability model (Eq. 16) and  $\lambda$  controls the curvature of the wetting-phase relative permeability model (Eq. 15).

As shown in the study of Pollyea (2016) and Wu et al. (2018),  $P_o$ ,  $\lambda$ , and  $S_{gr}$  are important parameters controlling the geometry of CO<sub>2</sub> plume and the accumulation of pressure during the CO<sub>2</sub> injection period; however, these parameters are subject to substantial uncertainty at the reservoir-site scale. Thus, the focus of this study is to quantify the role of these three parameters' effect on CO<sub>2</sub> migration and pressure distribution. The ranges for  $P_o$ ,  $\lambda$ , and  $S_{gr}$  are 0.4 – 0.8, 1 kPa – 200 kPa, and 0.1 – 0.4, respectively (Pini et al., 2012; André et al., 2014; Berg et al., 2013; Roels et al., 2016; Bachu and Bennion, 2008; Oh et al, 2013; Bennion and Bachu, 2005, 2006; Benson et al., 2006; Bertels et al., 2001). In this study,  $\lambda$  is the same parameter in capillary pressure and relative permeability model. Different capillary pressure and relative permeability models are defined by different parameter combinations of  $P_o$ ,  $\lambda$ , and  $S_{gr}$ .

To explain the effects of capillary pressure and relative permeability, a simulation ensemble is produced for unique combinations of  $P_o$ ,  $\lambda$ , and  $S_{gr}$  (from  $P_{cap}$  and  $k_{rel}$  model). The simulation ensemble is then analyzed to quantify the variability in both CO<sub>2</sub> migration and fluid pressure perturbation during CO<sub>2</sub> injections in a sandstone reservoir. A total of 460 different parameter combinations are randomly selected from the 3-D parameter space (Fig. 4.2), and simulations are completed using TOUGH3 (Jung et al., 2017), compiled with the fluid property module, ECO2N (Pruess and Spycher, 2007). The TOUGH3/ECO2N simulation code models

nonisothermal mixtures of CO<sub>2</sub>, brine, and water using the multi-phase formulation for Darcy's Law with phase partitioning on the basis of local equilibrium. Results from the physics-based simulation ensemble are utilized to train the ANN model, which is designed to provide estimates of both CO<sub>2</sub> plume geometry and fluid pressure propagation for unsampled portions of the 3-D parameter space.

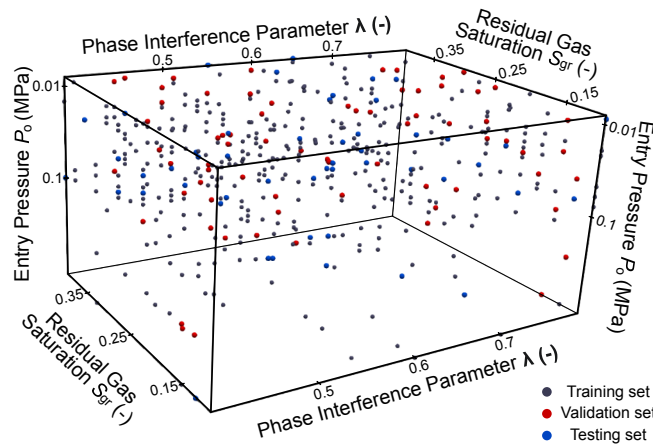


Figure 4.2: 3-D parameter combination distribution for datasets. Phase interference parameter  $\lambda$  governs curvature of van Genuchten model, while entry Pressure  $P_0$  characterizes the pressure drop across the interface, and Residual gas saturation  $S_{gr}$  is the residual gas phase (CO<sub>2</sub>) saturation. 460 of different parameter combinations are randomly distributed in the parameter space, which consists of three sub-datasets. The amount of data for training, validation, and testing dataset are 340, 70, and 50, respectively.

## 4.2.2 Artificial Neuron Networks (ANN)

The ANN algorithm is widely used in geosciences to analyze large datasets (i.e., “big data” problems) and it has been tested to be highly effective for capturing features of image data with large variabilities. The structure of ANN is loosely based on biological neurons of human brains and the neurons aim to find the relationships between input features and output variables. The basic unit of a neural network is the neuron, which is used to represent identical but independent parameters. In the context, each neuron is a unique algorithm, which takes a certain number of inputs and calculates a single output in terms of a specific function (Valentine and Woodhouse,

2010). Layers in ANN are characterized as different combinations of a specified number of neurons, where the calculated information is transferred between different layers, and ANN are composed of several different layers.

Each neuron is an algorithm, which maps the relationship between inputs and outputs. The importance of different inputs is governed by a set of weights, and the output is calculated according to a specified activation function based on a weighted sum of all the inputs. This process is described by Equation 18:

$$a = f\left(\sum_i^N \omega_i x_i + b_i\right), \quad (18)$$

where  $x$ ,  $a$ ,  $\omega$ , and  $b$  represent input, output, weight, and bias, respectively,  $f$  is the specific activation function, and  $N$  is the total number of inputs. Typically,  $\omega$  and  $b$  are unique to each neuron. The structure of ANN is described as many interconnected neurons organized as parallel layers (Fig. 4.3). For this study, the first layer corresponds to the input layer comprising five neurons, which are three parameters ( $P_o$ ,  $\lambda$ ,  $S_{gr}$ ) and spatial two coordinates (lateral and vertical) of each location. The last layer of one neuron is the output layer that corresponds to the prediction of the neuron network, which, for this study is either CO<sub>2</sub> saturation (sat) or pressure change ( $\Delta P$ ). The interior layers are referred to as “hidden layers” to transfer inputs and outputs (DeVries et al., 2017).

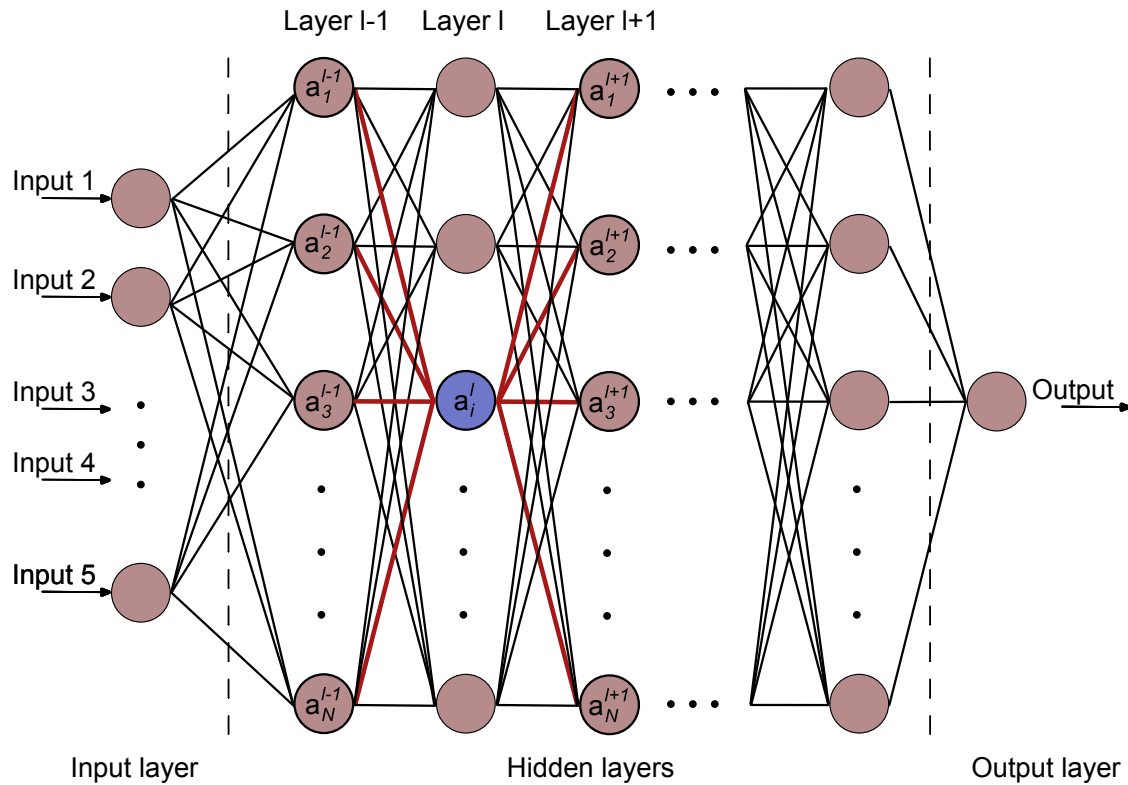


Figure 4.3: Structure and setup of an example of artificial neural networks (ANN). ANN consist of input layer, output layer, and hidden layers. Inside ANN, neurons representing weights take a weighted linear combination of the previous layer values and calculate a single value for the next layer applying a specific function. In this study, five neurons in the input layer correspond to five input parameters, and one neuron of the output layer represents the CO<sub>2</sub> saturation or pressure output.

Inside ANN, neurons, representing weights, take a weighted linear combination of the previous layer values and calculate a single value for the next layer by applying a specific function (Fig. 4.3). More specifically,  $a_1^{l-1}, a_2^{l-1}, \dots, a_N^{l-1}$  are outputs of  $l - 1$  layer. For neuron  $i$  in layer  $l$ ,  $a_i^l = f(\sum w_i a_i^{l-1} + b_i)$  is calculated by taking values from the previous layer as input, and it outputs a single value to every neuron in layer  $l + 1$  (Nielsen, 2015). The activation function of the last layer applied for CO<sub>2</sub> saturation is sigmoid, while a linear function is applied for pressure perturbation. As the value transfer is in a single forward direction, the network is characterized as

a feedforward network. Meanwhile, when dealing with different data, researchers should also take the structure of the network into account, which is identified by the number of neurons per layer and the number of hidden layers. In this study, separate deep ANN structures are utilized in training CO<sub>2</sub> saturation and pressure: for pressure perturbation training, 40 neurons per layer and 3 hidden layers are used, while for CO<sub>2</sub> saturation training, a deeper structure of 60 neurons per layer and 4 hidden layers is applied. These values were found via hyperparameter search on the validation data, exploring layer widths of 20, 40, and 60 neurons and depths of 2, 3, 4 layers.

The workflow of ANN consists of two phases: network training and final performance estimate (Fig. 4.4). These two phases require datasets for training, validation, and testing. The aggregate of these three datasets constitute the full dataset required for developing the ANN emulator. Each dataset consists of two parts: five input parameters and the physics-based simulation results from TOUGH3 codes. The training dataset is used for capturing features of simulation results, and the ML model calculates predictions based on the captured features. For evaluation, a cost function, the mean squared error (MSE), is applied to compare the physics-based results and the results predicted by the ANN. The ANN model is trained by minimizing the cost function by gradient descent over batches of the dataset. The training phase processes many epochs, which is one complete presentation of the data set to be learned by ANN model (epoch can be understood as training step), to capture features of physics-based results. During training, each epoch consists of exposing the network to a batch of samples to produce the predicted values and the cost function, then computing the gradient of network parameters (weights and biases), where the ADAM (adaptive moment estimation) variant of gradient descent is applied (Kingma and Ba, 2015). Afterward, these computed parameters are updated with respect to that gradient through the whole network. At the same time, during each epoch, the validation dataset is used to evaluate the model after the training of the training set, especially to avoid overfitting

on the training set, and this process improves the efficiency of prediction. Overfitting suggests a setback during training, in which the ML model is emphasizing or memorizing some certain parts

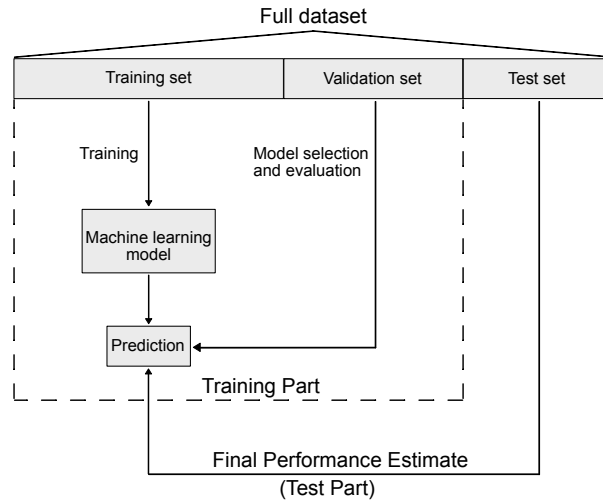


Figure 4.4: Workflow of artificial neuron networks (ANN). There are two phases of ANN: training phase and test phase, and the full dataset consists of training set, validation set, and testing set throughout the two phases. The training set is applied to the machine learning model for features capture, and parameters of the machine learning model are updated through evaluation. The validation set is applied for model selection and evaluation. During phase two, the testing set is used for prediction performance evaluation.

of the dataset, resulting in no further training improvement and the decrease of training efficiency. In addition, to avoid overfitting, the early stopping is performed, in which the prediction of validation dataset is evaluated for improvement after every epoch, and the model stops training after 200 epochs if no further improvement. After the whole training process, the performance of prediction through the trained ML model is tested based on the testing dataset in the final performance estimate step.

To explore the combined effects of capillary pressure and relative permeability, a 3-D parameter space comprising  $P_o$ ,  $\lambda$ , and  $S_{gr}$  is created to identify systematic changes in CO<sub>2</sub> plume geometry and fluid pressure propagation on the basis of these three reservoir properties (Fig. 4.2). Each point in this parameter space represents a unique combination  $P_o$ ,  $\lambda$ , and  $S_{gr}$ . The full

dataset for ANN training, validation and testing comprises CO<sub>2</sub> saturation and fluid pressure results from the physics-based numerical simulations of 460 randomly selected parameter combinations. The full dataset is segmented in 340 for ANN training, 70 for ANN validation, and 50 for ANN testing. The ANN emulator is developed using the Pytorch deep learning ML libraries (Paszke et al., 2019).

## 4.3 Results & Discussion

### 4.3.1 Overall Efficiency

The ANN training process captures features of physics-based simulation results, and then stops when no further improvement of the cost function is achieved. Once the training process is finished, prediction for the whole testing dataset is made based on the best ML model through training. The results and analyses of the prediction of the testing dataset are shown in Figure 4.5 and Figure 4.6.

In Figure 4.5, four different parameters combinations of capillary pressure and relative permeability models ( $P_o$ ,  $\lambda$ , and  $S_{gr}$ ) are represented to analyze the efficiency of ANN model prediction for CO<sub>2</sub> saturation and pressure perturbation. Another ten different parameter combinations of the testing dataset are shown in Appendix Figures B.1 and B.2 for CO<sub>2</sub> saturation and pressure, respectively. From left to right, the figures demonstrate the physics-based simulation results, ANN prediction results, and the difference between them. The broad similarity between the physical and predicted images implies that the ANN model captures the salient features of physics-based model.

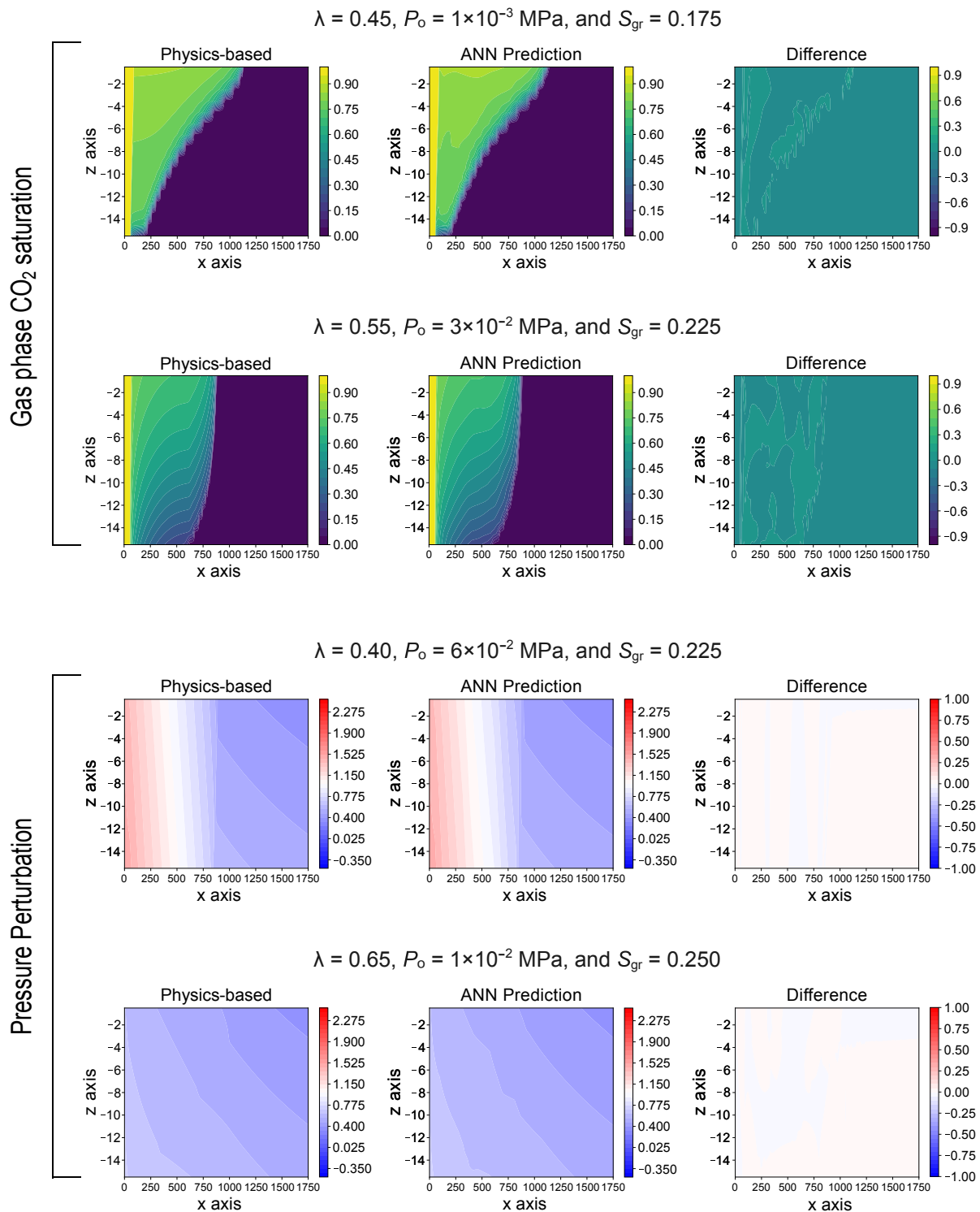


Figure 4.5: ANN Prediction results analyses of four different capillary pressure and relative permeability parameter combinations for CO<sub>2</sub> saturation and fluid pressure perturbation. From left to right, the figures demonstrate the physics-based simulation results, ANN prediction results, and the difference between them.

Figure 4.6 shows the complete evaluation of prediction results for CO<sub>2</sub> saturation and pressure accumulation across the reservoir for all 50 simulation results in the testing dataset. Figure 4.6A, D illustrate the ANN results in comparison with physics-based results for each grid cell of the reservoir domain for the whole testing dataset, which is a 50-simulation ensemble. For this analysis, the dots are colored by the number of grid cells that correspond with the physics-ANN comparison. Note that the red diagonal denotes a perfect match, where physics-based results values are equal to ANN predicted values. The generally efficacy of the ANN emulator is apparent as counts exceeding  $10^4$  along the diagonal. As with the individual analysis presented in Figure 4.5, the aggregate analysis of ANN prediction shows that pressure perturbation (Fig. 4.6D) outperforms that for CO<sub>2</sub> saturation (Fig. 4.6A), as the pressure results precisely falling on the diagonal red line, whereas a number of the counted grid cells in the CO<sub>2</sub> saturation prediction scenario fall off the diagonal owing to the two steep edges on the CO<sub>2</sub> plume (Fig. 4.6A). The first steep edge is a large saturation drop around the injection well, across a fully saturated area (left yellow column in physics-based images of CO<sub>2</sub> saturation in Fig. 4.5). On top of this full saturation edge, the edge of the CO<sub>2</sub> plume also shows a steep saturation drop, ranging from non-zero to zero values. A similar situation was observed by Zhang et al., (2018), who found that a steep saturation drop at the edge of CO<sub>2</sub> plume from  $\sim 0.1$  to 0 at a short distance of 200 m. This systematic disparity occurs because the ANN model trends to smooth sharp gradients with more continuous changes. This phenomenon is a result of the CO<sub>2</sub> saturation requiring a deeper network to capture the boundary features in comparison to the fluid pressure. In addition, two peaks of the counted grid cell distribution are located in two corners where the saturation is 0% (bottom left of Fig. 4.6A) and 100% (top right of Fig. 4.6A), with a large number of grid cells falling in the area of 0% (no CO<sub>2</sub> saturation in the far-field) and 100% saturation (fully saturated around the injection well) area.

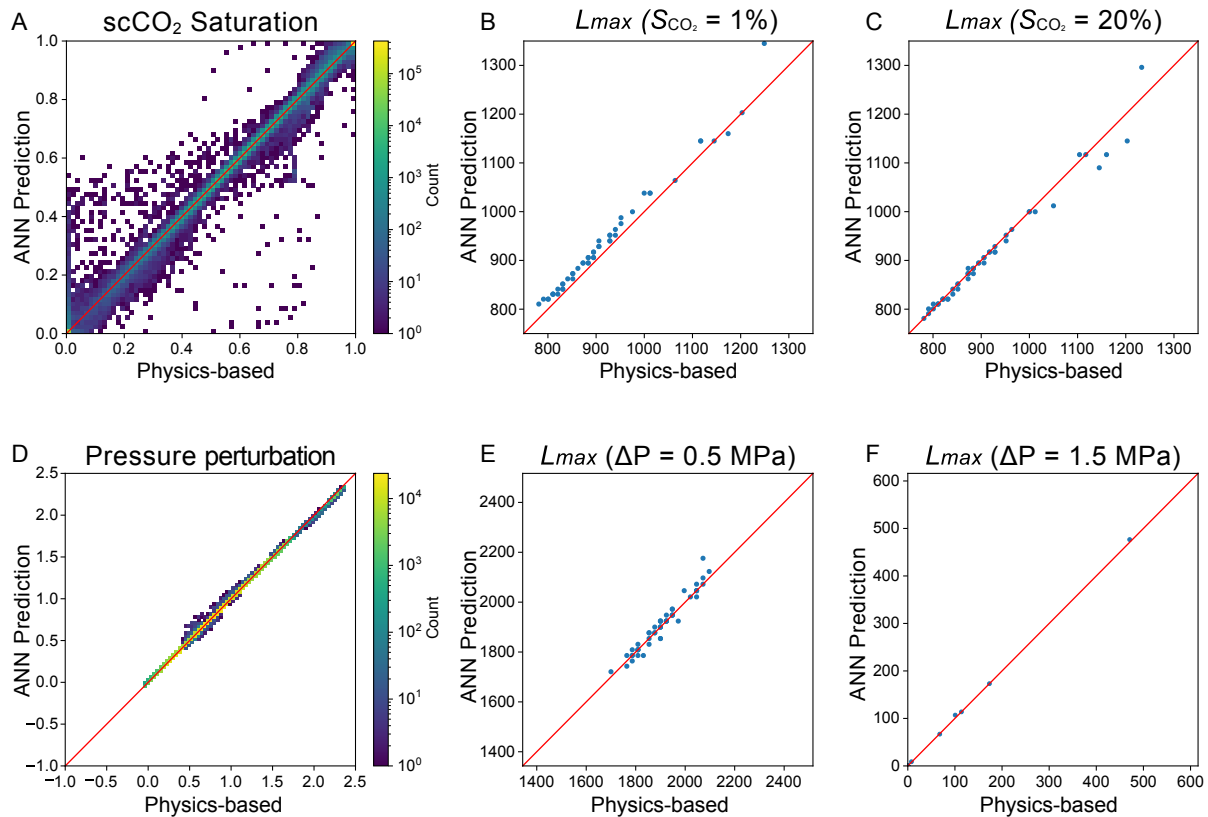


Figure 4.6: The evaluation of predicted results for CO<sub>2</sub> saturation and pressure accumulation across the reservoir. Figures A and D illustrate the counted distribution of all grid cells in the testing dataset with the comparison between physics-based simulation and ANN prediction results of the reservoir domain. Figures B and E indicate the comparison of the maximal plume length when sat = 1% and 20% of physics-based and ANN prediction results for the testing dataset, respectively. Figures E and F demonstrate the lengths of pressure perturbation distribution when  $\Delta P = 0.5$  MPa and 1.5 MPa for testing dataset, respectively.

The length of CO<sub>2</sub> saturation and pressure plume are of particular interest because they provide estimations for leakage observation and storage efficiency (Bromhal et al., 2014). Figure 4.6B presents the comparison between the physics-based and ANN prediction results for the testing dataset on the maximum length of the plume when CO<sub>2</sub> saturation is 0.01 (i.e., 1% free-phase CO<sub>2</sub>), which is considered as the boundary of the plume. In contrast, Figure 4.6C captures the plume migration maximal distance when CO<sub>2</sub> saturation is 0.2 (20% free-phase CO<sub>2</sub>). The testing performance for the 20% CO<sub>2</sub> contour is better than that of the 1%, as indicated by a higher

proportion of the 20% results falling on the diagonal. The reason for the performance difference lies in the smooth trend of ANN model at the plume boundary for 0.01 CO<sub>2</sub> saturation, which is harder to predict the steep drop of at the plume boundary for 0.01 CO<sub>2</sub> saturation. Similarly, Figure 4.6E and 4.6F demonstrate the maximum length of pressure perturbation distribution when  $\Delta P$  is 0.5 MPa and 1.5 MPa for testing dataset, respectively. The results imply that the trained ANN model performs well regarding pressure change. However, some physics-based simulations did not reach 1.5 MPa overpressure, resulting in fewer dots (counted grid cells with physics-ANN comparison) in Figure 4.6F.

The results over the testing dataset demonstrate ANN emulation methods provide excellent results for capturing the major distribution of both CO<sub>2</sub> saturation and fluid pressure change when trained on physics-based numerical simulations. This result is well-supported when comparing the pixel-by-pixel difference between the physics-based model and the ANN emulator (Fig. 4.5, third column). These results also show that much of the difference between the physics-based and ANN model occurs in predictions of CO<sub>2</sub> saturation at the leading edge of the plume, where the saturation gradient is the highest. In contrast, the differences in fluid pressure accumulation are more evenly distributed across the model. This disparity may be a result of the physical and chemical processes governing CO<sub>2</sub> migration and fluid pressure propagation. For example, fluid pressure propagation is governed by pressure diffusion, which is smoothly varying response to the pressure gradient. In contrast, CO<sub>2</sub> saturation at the leading edge of the plume is governed by complex interactions between multi-phase transport properties and fluid system thermodynamics, i.e., CO<sub>2</sub> dissolution (Jayne et al., 2019b). In aggregate, the individual results presented in Figure 4.5 suggest that ANN methods adequately capture the overall patterns for both CO<sub>2</sub> saturation and fluid pressure propagation, but subtle variations of interconnected physical and chemical process are subject to modest uncertainty.

## 4.3.2 Parametric Analysis of 3-D Parameter Space

The ability of the ANN model to emulate results of the physics-based model suggests that the ANN model is suitable for sampling the parameter space at higher resolution with much greater computational efficiency than the physics-based modeling approach. On this basis, the ANN network developed in Section 4.2.2 is used to generate CO<sub>2</sub> saturation and pressure propagation models across a finely discretized sampling of the parameter space comprising 2691 unique parameter combinations. These ANN models are then utilized to generate response surface mappings for analyzing systematic variations of CO<sub>2</sub> plume geometry and pressure accumulation across the complete 3-D parameter space. Figure 4.7A presents the complete response mapping for maximum lateral extent of 1% CO<sub>2</sub> saturation of ANN model. To more clearly identify patterns in the response mapping, Figure 4.7B presents isosurface of Figure 4.7A to illustrates the parameter combinations for which the maximum radial extent of 1% CO<sub>2</sub> saturation is 900 m. Similarly, Figure 4.8A shows the response surface mappings for the maximum lateral extent of 0.5 MPa fluid pressure for ANN model, while Figure 4.8B shows the isosurfaces within Figure 4.8A for which the maximum radial extent 0.5 MPa fluid pressure propagation is 2000 m.

The results of discrete analysis developed as part of the ANN testing procedure (Fig. 4.6A-C) illustrate the high efficiency of ANN predictions due to the comparison between physics-based results and ANN prediction results, and it provides support for detailed analysis of the ANN response and isosurface mappings across the completed 3-D parameter space. The prediction results provide a more comprehensive understanding of parameter effects analyses.

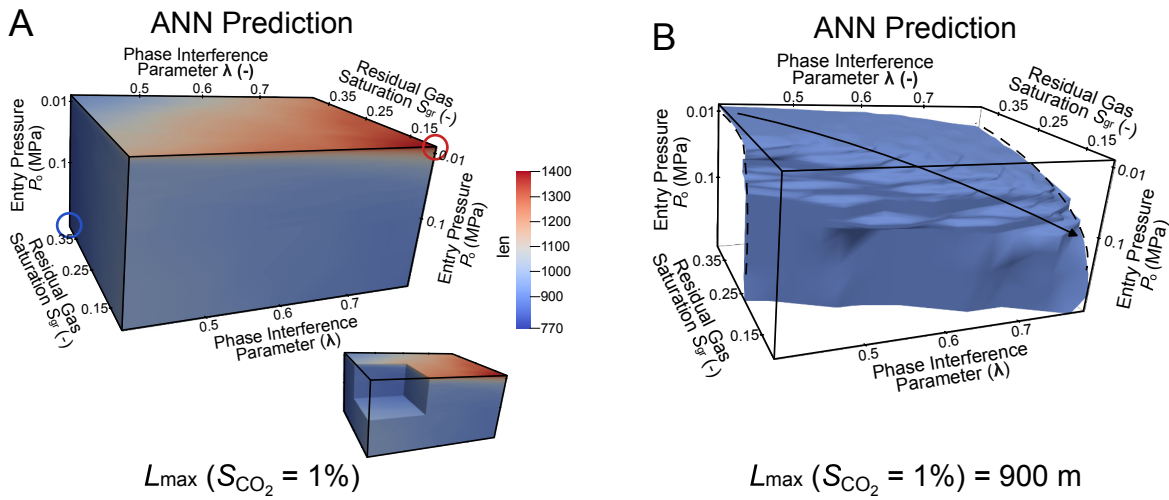


Figure 4.7: Figure A shows CO<sub>2</sub> saturation maximal expansion when sat = 1% over the 3-D parameter space for ANN prediction results. Inset illustrates cutaway for the interior structures of 3-D results. Figure B shows the furthest plume edge (isosurfaces) of CO<sub>2</sub> saturation at 900 m when sat = 1% for ANN prediction results.

The results presented in Figures 4.7 indicate that  $P_o$  imposes first-order control on the maximum extent of CO<sub>2</sub> migration. This is evident by the steep vertical gradient in the response mapping, particularly a low  $P_o$  (Fig. 4.7A), as well as the 900 m isosurface, which exhibits a systematic trend across the parameter space (Fig. 4.7B). This result suggests that capillary pressure effects are more important for lateral CO<sub>2</sub> migration than relative permeability effects. This result contradicts Pollyea (2016), which tested only the relative permeability parameter space found that CO<sub>2</sub> mobility, and thus plume extent, is governed by non-wetting phase relative permeability, which is largely controlled by residual gas saturation ( $S_{gr}$ ). However, the finding that low entry pressure results in larger CO<sub>2</sub> plumes is congruent with Wu et al. (2018), which tested parameter space for the capillary pressure model. This phenomenon occurs because small  $P_o$  encourages the migration of CO<sub>2</sub> saturation, however, the effects of  $S_{gr}$  and  $\lambda$  impose greater control on CO<sub>2</sub> plume extent as  $P_o$  increases. This can be seen in Figure 4.7B as the isosurface inclines from back top left to front bottom right, where large  $\lambda$  and small  $S_{gr}$  facilitate increasing

CO<sub>2</sub> mobility. These second order effects occur because phase interference ( $\lambda$ ) governs the curvature of the wetting phase relative permeability, so that large  $\lambda$  maintains greater wetting-phase relative permeability allowing (i) pore drainage to more readily occur and (ii) the CO<sub>2</sub> plume to migrate further from the injection well. In contrast, residual CO<sub>2</sub> saturation ( $S_{gr}$ ) controls the curvature of non-wetting phase relative permeability, where large  $S_{gr}$  results in dramatic changes to nonwetting-phase relative permeability for very small changes in wetting phase saturation. As a consequence,  $S_{gr}$  is an important factor on CO<sub>2</sub> mobility, and small  $S_{gr}$  maintains greater CO<sub>2</sub> mobility over a wider range of wetting phase saturation conditions. In aggregate, the black arrow (Fig. 4.7B) indicates the curving trend of the isosurface taking the three parameters into account, however, the length of the CO<sub>2</sub> plume is inversely proportional to the inclining trend of the isosurface. Generally, the length of the plume shows the largest values at low  $P_o$ , low  $S_{gr}$ , and high  $\lambda$  (Fig. 4.7A, red circle) and the smallest values at high  $P_o$ , high  $S_{gr}$ , and low  $\lambda$  (Fig. 4.7A, blue circle). To illustrate the variable effects of  $S_{gr}$  with decreasing  $\lambda$ , two black dashed lines are drawn Figure 4.7B to show how the 900 m isosurface dips gently in the upper left (low  $P_o$ , low  $\lambda$ , and high  $S_{gr}$ ), but the dips more steeply towards the lower right (high  $P_o$ , high  $\lambda$ , and low  $S_{gr}$ ).

As with the CO<sub>2</sub> plume extent,  $P_o$  is the dominant parameter for pressure perturbation, which is indicated by the almost horizontally distributed isosurfaces (Fig. 4.8B). Entry pressure is the largest control of CO<sub>2</sub> intrusion into pores media, and small  $P_o$  implies more CO<sub>2</sub> intrusion and father fluid pressure propagation. For high  $P_o$ , however, the effects of  $S_{gr}$  and  $\lambda$  are not uniform. In low  $\lambda$  and low  $S_{gr}$  area, their effect on fluid pressure propagation is limited, and  $P_o$  controls the migration of fluid pressure. In opposite, high  $\lambda$  and high  $S_{gr}$  encourage the migration of fluid pressure, supported by the inclining trend of isosurface as shown in black arrow (Fig. 4.8B). In addition,  $\lambda$  and  $S_{gr}$  show equally contribution in the increase of fluid pressure propagation, as indicated by the same slope of the two black dash lines (Fig. 4.8B). Specifically, there is a peak of fluid pressure propagation for high  $S_{gr}$  and low  $\lambda$ , and this suggests that  $S_{gr}$  is the second parameter encouraging pressure migration.  $S_{gr}$  governs the mobility of the non-wetting phase,

and high  $S_{gr}$  illustrates the slow CO<sub>2</sub> mobility increase as it enters pores, resulting in the fast accumulation of fluid pressure.

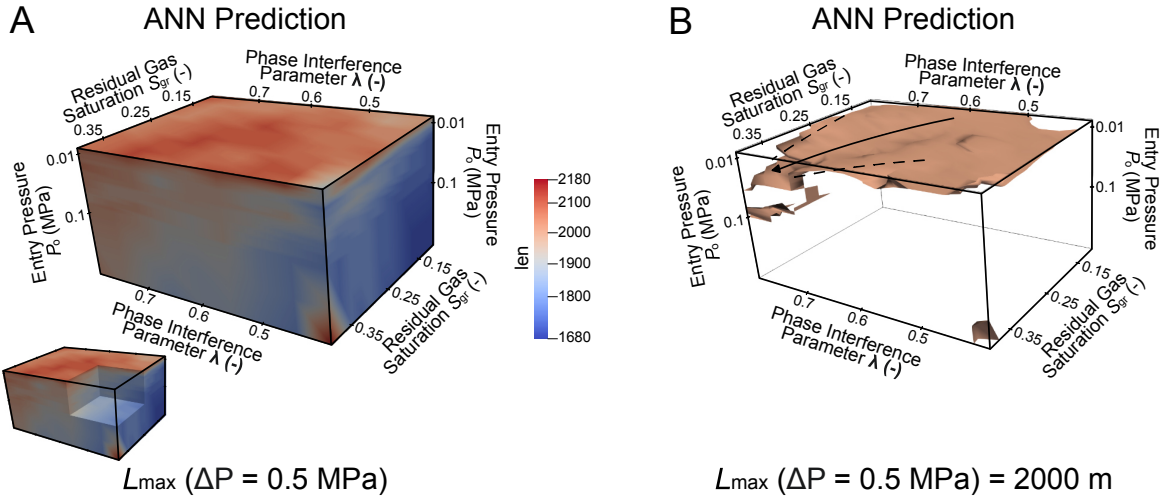


Figure 4.8: Figure A shows fluid pressure perturbation maximal expansion when  $\Delta P = 0.5 \text{ MPa}$  over the 3-D parameter space for ANN prediction results. Inset illustrates cutaway for the interior structures of 3-D results. The front side of the parameter domain in pressure is different from that in saturation figures (Fig. 4.7). Figure B shows the furthest plume edge (isosurfaces) of fluid pressure perturbation at 2000 m when  $\Delta P = 0.5 \text{ MPa}$  for ANN prediction results.

The predicted results based on the ANN model provide an understanding of the combining effects of capillary pressure and relative permeability to CO<sub>2</sub> saturation and fluid pressure migration in a sandstone reservoir during the CCS injection period. Three parameters  $P_o$ ,  $\lambda$ , and  $S_{gr}$  from different capillary pressure and relative permeability models are studied, and the response surface results of 3-D parameter space show that  $P_o$  is the dominant parameter controlling the migration of CO<sub>2</sub> saturation and fluid pressure accumulation, which further implies that capillary pressure effects are of greater importance for predicting both CO<sub>2</sub> plume geometry and fluid pressure accumulation. Small  $P_o$  encourages the migration of CO<sub>2</sub> saturation and fluid pressure accumulation, while large  $P_o$  inhibits the migration. In addition, the effect of  $\lambda$  and  $S_{gr}$  increase with increasing  $P_o$ . For CO<sub>2</sub> saturation, large  $\lambda$  and small  $S_{gr}$  encourages the migration

of CO<sub>2</sub> saturation, while the effect of  $S_{gr}$  increases for the low  $\lambda$  range. However, high  $S_{gr}$  encourages the migration of pressure to a large extent comparing to  $\lambda$ .

### 4.3.3 Applications of ML Methods in CCS

Results from this study demonstrate that the trained ML model offers an alternative method for simulating CO<sub>2</sub> saturation and fluid pressure migration features across a high-dimensional parameter space. Furthermore, the new ML model represents advantages in terms of computational efficiency and run-time acceleration. For example, the physics-based simulations developed for this study required over ~4000 hours (~6 months) CPU time to produce 460 CO<sub>2</sub> injection simulations using the TOUGH3 code. In contrast, it takes a few hours to train the ML model to this entire dataset, and a few minutes to make predictions about thousands of combinations of reservoir parameters. In general, the trained ANN model can accelerate the CO<sub>2</sub> saturation and pressure distribution prediction process without training by at least 25,000%. In addition, the Pytorch ML libraries (insert reference) have been shown here be result in a highly efficient workflow; the ANN model developed for this project comprises just a couple of hundred lines of python code (van Rossum and Drake, 1995).

In addition, the trained ML model provides an immense potential for predicting CO<sub>2</sub> migration results over an extended parameter range, which may prove beneficial for developing intuition about the outcomes of complex multi-phase flow and transport processes in the face of substantial parametric uncertainty. Moreover, the combination of ANN simulation methods and response surface analysis provides a framework for efficiently analyzing parametric uncertainty with increasingly higher dimensionality. More broadly, the trained ANN model performs well in capturing CO<sub>2</sub> saturation and pressure features during CCS and shows the capability in facilitating closer examination of larger parameter spaces with substantial gains of computational efficiency. As a result, the examination can contribute to deeper understanding in the underlying physical

fundamentals of CO<sub>2</sub> saturation and pressure perturbation mechanisms. The application of this modeling approach may also provide new avenues of support for in the siting CCS projects. Furthermore, the workflow developed here for ANN model development is applicable to numerous geoenery technologies, e.g., enhanced geothermal, oilfield wastewater disposal, subsurface hydrogen storage, and nuclear waste disposal.

## 4.5 Conclusion

An ANN model is trained through physics-based simulations to discover the combined effects of capillary pressure and relative permeability, which both have substantial variability, to scCO<sub>2</sub> saturation and pressure perturbation in a sandstone reservoir during CCS injection period. The trained ANN model provides efficient prediction over large parameter space with speedups of at least 25,000 times, in which the massive predictions can be generated in minutes comparing to several months which are typically required to run physics-based simulations with TOUGH3 codes. Once trained, the prediction results though the ANN model provides basic insights into CO<sub>2</sub> migration physics and phenomenology.

The analyses result on the effects of three parameters,  $P_o$ ,  $\lambda$ , and  $S_{gr}$  suggest that

- (1) Capillary entry pressure ( $P_o$ ) is the dominant parameter at the small  $P_o$  range. Small  $P_o$  encourages the migration of CO<sub>2</sub> saturation and fluid pressure accumulation, while large  $P_o$  inhibits the migration.
- (2) The effect of  $\lambda$  and  $S_{gr}$  increase along with the increase of  $P_o$ . Especially, for saturation, the effect of  $S_{gr}$  increases with decreasing  $\lambda$  for the large  $P_o$  range. Moreover, large  $\lambda$  and small  $S_{gr}$  encourages the migration of CO<sub>2</sub> saturation. In contrast, for pressure, the migration is encouraged by high  $S_{gr}$ .

The analyses of different parameters from capillary pressure and relative permeability model provide a more comprehensive understanding of the CO<sub>2</sub> saturation and pressure migration mechanisms. More broadly, this artificial neuron network approach could be applied to other geologic fluid systems to gain deeper insights into the complicated relationships between multi-phase fluid flow, thermodynamics, and fluid-rock interactions.

# Chapter 5

## Conclusion

This dissertation focuses on the studies about the CO<sub>2</sub> distribution, migration, and transportation during capillary trapping and mineral trapping in sandstone and fractured basalt reservoirs applying physics-based numerical simulations and machine learning methods. The conclusions from the last three chapters are summarized as:

- (1) The balance of buoyancy and capillary force strongly affects the vertical migration of CO<sub>2</sub> in sandstone reservoir during CO<sub>2</sub> injection. If buoyancy is larger than capillary force, CO<sub>2</sub> vertical migration is encouraged. In opposite, large capillary force inhibits the vertical migration of CO<sub>2</sub>. In addition, the large variability of capillary pressure plays an important role in CO<sub>2</sub> migration. The parameters  $P_o$ , and  $\lambda$  of van Genuchten capillary pressure model demonstrate different effects on CO<sub>2</sub> plume shape.
- (2) The application of machine learning to subsurface simulations provides large potential at computational efficiency improvement and reveals outstanding performance at the prediction of fluid flow mechanisms for the more realistic condition during CCS projects. The analyses of 3-D parameter variability effects from capillary pressure and relative permeability model on fluid flow migration and pressure distribution provide a better understanding of the relationship between reservoir uncertainties and fluid flow mechanisms.

(3) Carbon mineralization in basalt fracture system is largely controlled by multi-phase mobility, and secondary mineral precipitation focuses on the diffusion-controlled area. In addition, the mineral precipitation decreases fracture permeability and results in a self-sealing system which mitigates CO<sub>2</sub> upward leakage risk. As a result, it illustrates the important effect of fracture permeability alteration due to porosity-permeability coupling.

This study provides understanding about the role of capillary and mineral trapping mechanisms during industrial-scale CCS, while demonstrating the computational efficiency machine learning application. As a result, it opens up the possibility of studies about the effect of more complicated and more variable of reservoir properties on fluid dynamics during CCS projects with the application of machine learning. The deep exploration of the relationship between reservoir heterogeneity and fluid flow mechanisms reveals a board application in subsurface multi-component multi-phase fluid dynamics.

## Bibliography

- Adeoye, J.T., Menefee, A.H., Xiong, W., Wells, R.K., Skemer, P., Giammar, D.E. and Ellis, B.R., 2017. Effect of transport limitations and fluid properties on reaction products in fractures of unaltered and serpentinized basalt exposed to high  $P_{CO_2}$  fluids. *International Journal of Greenhouse Gas Control*, 63, pp.310–320.
- André, L., Peysson, Y. and Azaroual, M., 2014. Well injectivity during  $CO_2$  storage operations in deep saline aquifers—part 2: Numerical simulations of drying, salt deposit mechanisms and role of capillary forces. *International Journal of Greenhouse Gas Control*, 22, pp.301–312.
- Andreani, M., Luquot, L., Gouze, P., Godard, M., Hoise, E. and Gibert, B., 2009. Experimental study of carbon sequestration reactions controlled by the percolation of  $CO_2$ -rich brine through peridotites. *Environmental Science & Technology*, 43(4), pp.1226-1231.
- Aradóttir, E.S.P., Sonnenthal, E.L., Björnsson, G. and Jónsson, H., 2012. Multidimensional reactive transport modeling of  $CO_2$  mineral sequestration in basalts at the Hellisheidi geothermal field, Iceland. *International Journal of Greenhouse Gas Control*, 9, pp.24-40.
- Arns, J.Y., Arns, C.H., Sheppard, A.P., Sok, R.M., Knackstedt, M.A. and Pinczewski, W.V., 2003. Relative permeability from tomographic images; effect of correlated heterogeneity. *Journal of Petroleum Science and Engineering*, 39(3-4), pp.247–259.
- Ataie-Ashtiani, B., Hassanizadeh, S.M. and Celia, M.A., 2002. Effects of heterogeneities on capillary pressure–saturation–relative permeability relationships. *Journal of Contaminant Hydrology*, 56, pp.175–192.

## Bibliography

Bachu, S., 2000. Sequestration of CO<sub>2</sub> in geological media: criteria and approach for site selection in response to climate change. *Energy conversion and Management*, 41(9), pp. 953–970.

Bachu, S., 2003. Screening and ranking of sedimentary basins for sequestration of CO<sub>2</sub> in geological media in response to climate change. *Environ Geol*, 44, pp. 277–289.

Bachu, S. and Bennion, B., 2008. Effects of in-situ conditions on relative permeability characteristics of CO<sub>2</sub>-brine systems. *Environ Geol*, 54, pp. 1707–1722.

Bachu, S., Gunter, W.D. and Perkins, E.H., 1994. Aquifer disposal of CO<sub>2</sub>: hydrodynamic and mineral trapping. *Energy Convers Mgmt*, 35(4), pp.269–279.

Bennion, B. and Bachu, S., 2005. Relative permeability characteristics for supercritical CO<sub>2</sub> displacing water in a variety of potential sequestration zones in the western Canada sedimentary basin. In: *SPE Annual Technical Conference and Exhibition*. Society of Petroleum Engineers.

Bennion, D.B. and Bachu, S., 2006. Dependence on temperature, pressure, and salinity of the IFT and relative permeability displacement characteristics of CO<sub>2</sub> injected in deep saline aquifers. In: *2006 SPE Technical Conference and Exhibition*. Society of Petroleum Engineers, San Antonio, TX.

Benson, S.M. and Cole, D.R., 2008. CO<sub>2</sub> sequestration in deep sedimentary formations. *Elements*, 4, pp.325-331.

Benson, S., Tomutsa, L., Silin, D. and Kneafsy, T., 2006. Core scale and pore scale studies of carbon dioxide migration in saline formations. In: *8<sup>th</sup> International Conference on Greenhouse Gas Control Technologies (GHGT-8)*, Trondheim, Norway.

- Berg, S., Oedai, S. and Ott, H., 2013. Displacement and mass transfer between saturated and unsaturated CO<sub>2</sub>-brine systems in sandstone. *International Journal of Greenhouse Gas Control*, 12, pp.478–492.
- Bergen, K.J., Johnson, P.A., Maarten, V. and Beroza, G.C., 2019. Machine learning for data-driven discovery in solid earth geoscience. *Science*, 363, 1299.
- Bertels, S.P., DiCarlo, D.A. and Blunt, M.J., 2001. Measurement of aperture distribution, capillary pressure, relative permeability, and in situ saturation in a rock fracture using computed tomography scanning. *Water Resources Research*, 37(3), pp.649-662.
- Beucher, A., Österholm, P., Martinkauppi, A., Edén, P. and Fröjdö, S., 2013. Artificial neural network for acid sulfate soil mapping: Application to the Sirppujoki River catchment area, southwestern Finland. *Journal of Geochemical Exploration*, 125, pp.46-55.
- Bishop, C.M., 1995. Neural networks for pattern recognition. Oxford Univ. Press.
- Blanc, P., Lassin, A., Piantone, P., Azaroual, M., Jacquemet, N., Fabbri, A. and Gaucher, E.C., 2012. Thermoddem: A geochemical database focused on low temperature water/rock interactions and waste materials. *Applied geochemistry*, 27(10), pp.2107-2116.
- Bromhal, G.S., Birkholzer, J., Mohaghegh, S.D., Sahinidis, N., Wainwright, H., Zhang, Y., Amini, S., Gholami, V., Zhang, Y. and Shahkarami, A., 2014. Evaluation of rapid performance reservoir models for quantitative risk assessment. *Energy Procedia*, 63, pp.3425-3431.
- Brown, H.W., 1951. Capillary pressure investigations. *Journal of Petroleum Technology*, 192.
- Carpita, M., Giorgis, T. and Battistelli, A., 2006. Modeling CO<sub>2</sub> injection with halite precipitation using an extended verma & pruess porosity-permeability model. In: *Proceedings of the TOUGH2 Symposium*, Lawrence Berkeley National Laboratory, Berkeley, CA, USA.

## Bibliography

- Chaouche, M., Rakotomalala, N., Salin, D., Xu, B. and Yortsos, Y.C., 1994. Capillary effects in drainage in heterogeneous porous media: continuum modelling, experiments and pore network simulations. *Chemical Engineering Science*, 49(15), pp.2447–2466.
- Chen, B., Harp, D.R., Lin, Y., Keating, E.H. and Pawar, R.J., 2018. Geologic CO<sub>2</sub> sequestration monitoring design: a machine learning and uncertainty quantification based approach. *Applied energy*, 225, pp.332-345.
- Corey, A., 1954. The interrelation between gas and oil relative permeabilities. *Prod. Monthly*, 38-41.
- Dai, Z., Middleton, R., Viswanathan, H., Fessenden-Rahn, J., Bauman, J., Pawar, R., Lee, S. and McPherson, B., 2013. An integrated framework for optimizing CO<sub>2</sub> sequestration and enhanced oil recovery. *Environ Sci Technol Lett*, 1(1), pp.49-54.
- DeVries, P.M.R., Thompson, T.B. and Meade, B.J., 2017. Enabling large-scale viscoelastic calculations via neural network acceleration. *Geophysical research letters*, 44, pp.2662-2669.
- Dlugokencky, E. and Tans, P., 2018. Trends in atmospheric carbon dioxide, National Oceanic & Atmospheric Administration, Earth System Research laboratory (NOAA/ESRL), available at [http:// www.esrl.noaa.gov/gmd/ccgg/trends/global.html](http://www.esrl.noaa.gov/gmd/ccgg/trends/global.html), last access: 4 September 2018.
- Egermann, P., Chalbaud, C., Duquerroix, J.P. and Le Gallo, Y., 2006. An integrated approach to parameterize reservoir models for CO<sub>2</sub> injection in aquifers. In: *SPE Annual Technical Conference and Exhibition*. Society of Petroleum Engineers.
- EIA. U.S. Energy Information Administration (EIA). How much carbon dioxide is produced when different fuels are burned? [Accessed 4 May 2018] Available online at: <https://www.eia.gov/tools/faqs/faq.php?id=73&t=11>.

- Eldholm, O. and Coffin, M.F., 2000. Large igneous provinces and plate tectonics. *Geophysical Monograph-American Geophysical Union*, 121, pp.309-326.
- Enick, R.M. and Klara, S.M., 1990. CO<sub>2</sub> solubility in water and brine under reservoir conditions. *Chem. Eng. Comm*, 90, pp.23-33.
- Esposito, A. and Benson, S.M., 2011. Remediation of possible leakage from geologic CO<sub>2</sub> storage reservoirs into groundwater aquifers. *Energy Procedia*, 4, pp.3216–3223.
- Ferrand, L.A. and Celia, M.A., 1992. The effect of heterogeneity on the drainage capillary pressure-saturation relation. *Water Resources Research*, 28(3), pp.859–870.
- Gierzynski, A.O. and Pollyea, R.M., 2017. Three-phase CO<sub>2</sub> flow in a basalt fracture network. *Water Resources Research*, 53(11), pp.8980-8998.
- Gislason, S.R., Wolff-Boenisch, D., Stefansson, A., Oelkers, E.H., Gunnlaugsson, E., Sigurdardottir, H., Sigfusson, B., Broecker, W.S., Matter, J.M., Stute, M. and Axelsson, G., 2010. Mineral sequestration of carbon dioxide in basalt: A pre-injection overview of the CarbFix project. *International Journal of Greenhouse Gas Control*, 4(3), pp.537-545.
- Goldberg, D.S., Takahashi, T. and Slagle, A.L., 2008. Carbon dioxide sequestration in deep-sea basalt. *Proceedings of the National Academy of Sciences of the United States of America*, 105(29), pp.9920-9925.
- Gudbrandsson, S., Wolff-Boenisch, D., Gislason, S.R. and Oelkers, E.H., 2011. An experimental study of crystalline basalt dissolution from  $2 \leq \text{pH} \leq 11$  and temperatures from 5 to 75° C. *Geochimica et Cosmochimica Acta*, 75(19), pp.5496-5509.

## Bibliography

- Gysi, A.P. and Stefánsson, A., 2012. CO<sub>2</sub>-water–basalt interaction. Low temperature experiments and implications for CO<sub>2</sub> sequestration into basalts. *Geochimica et Cosmochimica Acta*, 81, pp.129-152.
- Han, W.S., Lee, S.Y., Lu, C. and McPherson, B.J., 2010. Effects of permeability on CO<sub>2</sub> trapping mechanisms and buoyancy-driven CO<sub>2</sub> migration in saline formations. *Water Resources Research*, 46, W07510.
- Herzog, H., Golomb, D. and Zemba, S., 1991. Feasibility, modeling and economics of sequestering power plant CO<sub>2</sub> emissions in the deep ocean. *Environ Prog Sustain Energy*, 10(1), pp.64-74.
- Hesse, M.A., Orr, Jr. F.M. and Tchalepi, H.A., 2008. Gravity currents with residual trapping. *J. Fluid Mech.*, 611, pp.35-60.
- Hinton, G.E. and Salakhutdinov, R.R., 2006. Reducing the dimensionality of data with neural networks. *Science*, 333, pp.504-507.
- Holloway, S., Garg, A., Kapshe, M., Deshpande, A., Pracha, A.S., Khan, S.R., Mahmood, M.A., Singh, T.N., Kirk, K.L. and Gale, J., 2009. An assessment of the CO<sub>2</sub> storage potential of the Indian subcontinent. *Energy Procedia*, 1(1), pp.2607-2613.
- Hövelmann, J., Austrheim, H. and Jamtveit, B., 2012. Microstructure and porosity evolution during experimental carbonation of a natural peridotite. *Chemical Geology*, 334, pp.254-265.
- Hunt, J.R., Sitar, N. and Udell, K.S., 1988. Nonaqueous phase liquid transport and cleanup: 1. Analysis of Mechanisms. *Water Resources Research*, 24(8), pp.1247-1258.
- Iglauer, S., Paluszny, A., Pentland, C.H. and Blunt, M.J., 2011. Residual CO<sub>2</sub> imaged with X-ray micro-tomography. *Geophysical Research Letters*, 38, L21403.

- Jayne, R.S., Wu, H. and Pollyea, R.M., 2019a. Geologic CO<sub>2</sub> sequestration and permeability uncertainty in a highly heterogeneous reservoir. *International Journal of Greenhouse Gas Control*, 83, pp.128-139.
- Jayne, R.S., Zhang, Y. and Pollyea, R.M., 2019b. Using heat as a predictor of CO<sub>2</sub> breakthrough in highly heterogeneous reservoirs. *Geophysical Research Letters*, 46(11), pp.5879-5888.
- Juanes, R., Spiteri, E.J., Orr, Jr. F.M. and Blunt, M.J., 2006. Impact of relative permeability hysteresis on geological CO<sub>2</sub> storage. *Water Resources Research*, 42, W12418.
- Jung, Y., Pau, G.S.H., Finsterle, S. and Pollyea, R.M., 2017. TOUGH3: A new efficient version of the TOUGH suite of multiphase flow and transport simulators. *Computers & Geosciences*, 108, pp.2-7.
- Karpatne, A., Ebert-Uphoff, I., Ravela, S., Babaie, H.A. and Kumar, V., 2019. Machine learning for the Geosciences challenges and opportunities *IEEE transactions on knowledge and data engineering*, 31(8).
- Karpatne, A., Jiang, Z., Vatsavai, R.R., Shekhar, S. and Kumar, V., 2016. Monitoring land-cover changes: A machine-learning perspective. *IEEE Geoscience and Remote Sensing Magazine*, 4(2), pp.8-21.
- Kingma, D.P. and Ba, J.L., 2015. ADAM: a method for stochastic optimization. *arXiv preprint arXiv:1412.6980*.
- Knauss, K.G., Nguyen, S.N. and Weed, H.C., 1993. Diopside dissolution kinetics as a function of pH, CO<sub>2</sub>, temperature, and time. *Geochimica et Cosmochimica Acta*, 57(2), pp.285-294.
- Krause, M., Perrin, J.C. and Benson, S.M., 2011. Modeling permeability distributions in a sandstone core for history matching coreflood experiments. In: *SPE International Conference*

## Bibliography

- on CO<sub>2</sub> Capture, Storage, and Utilization*. Society of Petroleum Engineers, San Diego, California.
- Krevor, S.C.M., Pini, R., Li, B. and Benson, S.M., 2011. Capillary heterogeneity trapping of CO<sub>2</sub> in a sandstone rock at reservoir conditions. *Geophysical Research Letters*, 38, L15401.
- Lary, D.J., Alavi, A.H., Gandomi, A.H. and Walker, A.L., 2016. Machine learning in geosciences and remote sensing. *Geoscience frontiers*, 7, pp.3-10.
- Lenormand, R., 1990. Liquids in porous media. *J. Phys.: Condens Matter*, 2: SA79–SA88.
- Lenormand, R., Touboul, E. and Zarcone, C., 1988. Numerical models and experiments on immiscible displacements in porous media. *J. Fluid mech*, 189, pp.165–187.
- Le Quéré, C., Andrew, R.M., Friedlingstein, P., Sitch, S., Hauck, J., Pongratz, J., Pickers, P.A., Korsbakken, J.I., Peters, G.P., Canadell, J.G. and Arneeth, A., 2018. Global carbon budget 2018. *Earth System Science Data* 10, 2141-2194.
- Løvoll, G., Méheust, Y., Måløy, K.J., Aker, E. and Schmittbuhl, J., 2005. Competition of gravity, capillary and viscous forces during drainage in a two-dimensional porous medium, a pore scale study. *Energy*, 30, pp.861–872.
- Luhmann, A.J., Tutolo, B.M., Bagley, B.C., Mildner, D.F., Seyfried Jr, W.E. and Saar, M.O., 2017a. Permeability, porosity, and mineral surface area changes in basalt cores induced by reactive transport of CO<sub>2</sub>-rich brine. *Water Resources Research*, 53(3), pp.1908-1927.
- Luhmann, A.J., Tutolo, B.M., Tan, C., Moskowitz, B.M., Saar, M.O. and Seyfried Jr, W.E., 2017b. Whole rock basalt alteration from CO<sub>2</sub>-rich brine during flow-through experiments at 150°C and 150 bar. *Chemical Geology*, 453, pp.92-110.

- Maniar, H., Ryali, S., Kulkarni, M.S. and Abubakar, A., 2018. Machine learning methods in geosciences. *SEG international exposition and 88<sup>th</sup> annual meeting*, Anaheim, California.
- Marjanović, M., Kovačević, M., Bajat, B. and Voženílek, V., 2011. Landslide susceptibility assessment using SVM machine learning algorithm. *Engineering Geology*, 123(3), pp.225-234.
- Matter, J.M., and Kelemen, P.B., 2009. Permanent storage of carbon dioxide in geological reservoirs by mineral carbonation. *Nature Geoscience*, 2(12), pp.837-841.
- Matter, J.M., Stute, M., Snæbjörnsdóttir, S.Ó., Oelkers, E.H., Gislason, S.R., Aradóttir, E.S., Sigfusson, B., Gunnarsson, I., Sigurdardóttir, H., Gunnlaugsson, E. and Axelsson, G., 2016. Rapid carbon mineralization for permanent disposal of anthropogenic carbon dioxide emissions. *Science*, 352(6291), pp.1312-1314.
- McGrail, B.P., Schaef, H.T., Ho, A.M., Chien, Y.J., Dooley, J.J. and Davidson, C.L., 2006. Potential for carbon dioxide sequestration in flood basalts. *Journal of Geophysical Research: Solid Earth*, 111(B12).
- McGrail, B.P., Schaef, H.T., Spane, F.A., Cliff, J.B., Qafoku, O., Horner, J.A., Thompson, C.J., Owen, A.T. and Sullivan, C.E., 2017. Field validation of supercritical CO<sub>2</sub> reactivity with basalts. *Environmental Science & Technology Letters*, 4(1), pp.6-10.
- MER. Monthly Energy Review (MER). U.S. Energy Information Administration. DOE/EIA-0035(2018/2), (2018).
- Metz, B., Davidson, O., de Coninck, H., Loos, M. and Meyer, L., 2005. IPCC(Intergovernmental Panel on Climate Change) special report on carbon dioxide capture and storage. Technical report, Cambridge University Press.

## Bibliography

- Michael, K., Golab, A., Shulakova, V., Ennis-King, J., Allinson, G., Sharma, S. and Aiken, T., 2010. Geological storage of CO<sub>2</sub> in saline aquifers—A review of the experience from existing storage operations. *International Journal of Greenhouse Gas Control*, 4, pp.659–667.
- Mito, S., Xue, Z. and Ohsumi, T., 2008. Case study of geochemical reactions at the Nagaoka CO<sub>2</sub> injection site, Japan. *International Journal of Greenhouse Gas Control*, 2, pp.309–318.
- Mudunuru, M.K., O'Malley, D., Srinivasan, S., Hyman, J.D., Sweeney, M.R., Frash, L., Carey, B., Gross, M.R., Welch, N.J., Karra, S., Vesselinov, V.V., Kang, Q., Xu, H., Pawar, R.J., Carr, T., Li, L., Guthrie, G.D. and Viswanathan, H.S., 2020. Physics-informed machine learning for real-time unconventional reservoir management. *Association for the Advancement of Artificial Intelligence*.
- Nara, Y., Meredith, P.G., Yoneda, T. and Kaneko, K., 2011. Influence of macro-fractures and micro-fractures on permeability and elastic wave velocities in basalt at elevated pressure. *Tectonophysics*, 503(1-2), pp.52-59.
- Neilsen, M.A., 2015. Neural networks and Deep Learning, Determination Press. [Available at <http://neuralnetworksanddeeplearning.com>.].
- Nicot, J.P., 2008. Evaluation of large-scale CO<sub>2</sub> storage on fresh-water sections of aquifers: An example from the Texas gulf coast basin. *International Journal of Greenhouse Gas Control*, 2, pp.582–593.
- Oelkers, E.H. and Gislason, S.R., 2001. The mechanism, rates and consequences of basaltic glass dissolution: I. An experimental study of the dissolution rates of basaltic glass as a function of aqueous Al, Si and oxalic acid concentration at 25°C and pH= 3 and 11. *Geochimica et Cosmochimica Acta*, 65(21), pp.3671-3681.

- Oelkers, E.H., Gislason, S.R. and Matter, J., 2008. Mineral carbonation of CO<sub>2</sub>. *Elements*, 4(5), pp.333-337.
- Oh, J., Kim, K.Y., Han, W.S., Kim, T., Kim, J.C. and Park, E., 2013. Experimental and numerical study on supercritical CO<sub>2</sub>/brine transport in a fractured rock: Implications of mass transfer, capillary pressure and storage capacity. *Advances in Water Resources*, 62, pp.442– 453.
- Palandri, J.L., Kharaka, Y.K., 2004. A compilation of rate parameters of water-mineral interaction kinetics for application to geochemical modeling. U.S. Geological Survey, Menlo Park, California, P.64.
- Paszke, A., Gross, S., Massa, F., Lerer, A., Bradbury, J., Chanan, G., Killeen, T., Lin, Z., Gimelshein, N., Antiga, L., Desmaison, A. et al., 2019. PyTorch: An Imperative style, High-performance deep learning library, *Advances in Neural Information Processing Systems*, 32, pp.8024-8035.
- Pawar R., Dilmore R., Chu S., Zhang Y., Oldenburg C., Stauffer P., Guthrie G. and Bromhal G., 2017. Informing geologic CO<sub>2</sub> storage site management decisions under uncertainty: demonstration of NRAP's integrated assessment model (NRAP-IAM-CS) application. *Energy Procedia*, 114, pp.4330-4337.
- Perrin, J.C., Krause, M., Kuo, C.W., Miljkovic, L., Charoba, E. and Benson, S.M., 2009. Core-scale experimental study of relative permeability properties of CO<sub>2</sub> and brine in reservoir rocks. *Energy Procedia*, 1, pp.3515–3522.
- Pini, R. and Benson, S.M., 2013. Characterization and scaling of mesoscale heterogeneities in sandstones. *Geophysical Research Letters*, 40, pp.3903-3908.

## Bibliography

- Pini, R., Krevor, S.C.M. and Benson, S.M., 2012. Capillary pressure and heterogeneity for the CO<sub>2</sub>/water system in sandstone rocks at reservoir conditions. *Advances in Water Resources*, 38, pp.48–59.
- Pollyea, R.M., 2016. Influence of relative permeability on injection pressure and plume configuration during CO<sub>2</sub> injections in a mafic reservoir. *International Journal of Greenhouse Gas Control*, 46, pp.7–17.
- Pollyea, R.M. and Fairley, J.P., 2012. Implications of spatial reservoir uncertainty for CO<sub>2</sub> sequestration in the east Snake River Plain, Idaho (USA). *Hydrogeology Journal*, 20 (4), pp.689-699.
- Pollyea, R.M., Fairley, J.P., Podgorney, R.K. and Mcling, T.L., 2014. Physical constraints on geologic CO<sub>2</sub> sequestration in low-volume basalt formations. *Bulletin*, 126 (3-4), pp.344-351.
- Pollyea, R.M. and Rimstidt, J.D., 2017. Rate equations for modeling carbon dioxide sequestration in basalt. *Applied geochemistry*, 81, pp.53-62.
- Poulton, M.M., 2002. Neural networks as an intelligence amplification tool: A review of applications. *Geophysics*, 67(3), pp.979-993.
- Pruess, K., 2005. ECO2N: A TOUGH2 Fluid Property Module for Mixtures of Water, NaCl, and CO<sub>2</sub>. Tech. rep. Lawrence Berkeley National Laboratory, 2005. LBNL-57952.
- Pruess, K. and García, J., 2002. Multiphase flow dynamics during CO<sub>2</sub> disposal into saline aquifers. *Environ Geol*, 42, pp.282–295.
- Pruess, K. and Spycher, N., 2007. ECO2N–A fluid property module for the TOUGH2 code for studies of CO<sub>2</sub> storage in saline aquifers. *Energy conversion and management*, 48(6), pp.1761-1767.

- Pruess, K., Oldenburg, C. and Moridis, G., 1999. TOUGH2 User's Guide, Version 2. Tech. rep. Lawrence Berkeley National Laboratory, 1999. LBNL-43134.
- Reidel, S.P., Spane, F.A. and Johnson, V.G., 2002. Natural gas storage in basalt aquifers of the Columbia basin, Pacific Northwest USA: A guide to site characterization (No. PNNL-13962). Technical report, Pacific Northwest National Lab (PNNL), Richland, WA (United States).
- Roels, S.M., Chatib, N.E.I., Nicolaides, C. and Zitha, P.L.J., 2016. Capillary-driven transport of dissolved salt to the drying zone during CO<sub>2</sub> injection in homogeneous and layered porous media. *Transp Porous Med*, 111, pp.411–424.
- Rouet-Leduc, B., Hulbert, C., Lubbers, N., Barros, K., Humphreys, C.J. and Johnson, P.A., 2017. Machine learning predicts laboratory earthquakes. *Geophysical research letters*, 44, pp. 9276-9282.
- Rosenbauer, R.J., Thomas, B., Bischoff, J.L. and Palandri, J., 2012. Carbon sequestration via reaction with basaltic rocks: Geochemical modeling and experimental results. *Geochimica et Cosmochimica Acta*, 89, pp.116-133.
- Sharma, S.S., 2011. Determinants of carbon dioxide emissions: empirical evidence from 69 countries. *Applied Energy*, 88, pp. 376-382.
- Shaffer, G., 2010. Long-term effectiveness and consequences of carbon dioxide sequestration. *Nature Geoscience*. 3, pp.464-467.
- Schaef, H.T., McGrail, B.P. and Owen, A.T., 2010. Carbonate mineralization of volcanic province basalts. *International Journal of Greenhouse Gas Control*, 4(2), pp.249-261.
- Schaef, H.T., McGrail, B.P. and Owen, A.T., 2011. Basalt reactivity variability with reservoir depth in supercritical CO<sub>2</sub> and aqueous phases. *Energy Procedia*, 4, pp.4977-4984.

## Bibliography

- Shearer, C., Fofrich, R. and Davis, S.J., 2017. Future CO<sub>2</sub> emissions and electricity generation from proposed coal-fired power plants in India. *Earth's Future*, 5(4), pp.408-416.
- Shi, J.Q., Xue, Z. and Durucan, S., 2011. Supercritical CO<sub>2</sub> core flooding and imbibition in Tako sandstone—Influence of sub-core scale heterogeneity. *International Journal of Greenhouse Gas Control*, 5, pp.75–87.
- Smith, J.S., Isayev, O. and Roitberg A.E., 2017. ANBI-1: an extensible neural network potential with DFT accuracy at force field computational cost. *Chem. Sci.*, 8, pp.3192.
- Srinivasan, S., Karra, S., Hyman, J., Viswanathan, H. and Srinivasan, G., 2019. Model reduction for fractured porous media: a machine learning approach for identifying main flow pathways. *Computational geosciences*, 23, pp.617-629.
- Stockmann, G., Wolff-Boenisch, D., Gislason, S.R. and Oelkers, E.H., 2008. Dissolution of diopside and basaltic glass: the effect of carbonate coating. *Mineralogical Magazine*, 72 (1), pp.135-139.
- Szulczewski, M.L., MacMinn, C.W., Herzog, H.J. and Juanes, R., 2012. Lifetime of carbon capture and storage as a climate-change mitigation technology. *Proceedings of the National Academy of Sciences*, 109(14), pp.5185–5189.
- Tiwari, V.M., Rao, M.V. and Mishra, D.C., 2001. Density inhomogeneities beneath Deccan Volcanic Province, India as derived from gravity data. *Journal of Geodynamics*, 31(1), pp.1-17.
- Valentine, A.P. and Woodhouse, J.H., 2010. Approaches to automated data selection for global seismic tomography. *Geophysical Journal International*, 182, pp.1001-1012.

- Valera, M., Guo, Z., Kelly, P., Matz, S., Cantu, V.A., Percus, A.G., Hyman, J.D., Srinivasan, G. and Viswanathan, H.S., 2018. Machine learning for graph-based representations of three-dimensional discrete fracture networks. *Computational geosciences*, 22, pp.695-710.
- van der Meer, L.G.H., 1992. Investigations regarding the storage of carbon dioxide in aquifers in the Netherlands. *Energy convers. Mgmt*, 33(5-8), pp.611-618.
- van Genuchten, M.T., 1980. A closed-form equation for predicting the hydraulic conductivity of unsaturated soils. *SOIL SCI. SOC. AM. J.*, 44(5), pp.892–898.
- Van Rossum, G., and Drake Jr, F.L., 1995. Python reference manual. Centrum voor Wiskunde en Informatica Amsterdam.
- Verma, A. and Pruess, K., 1988. Thermohydrological conditions and silica redistribution near high-level nuclear wastes emplaced in saturated geological formations. *Journal of Geophysical Research: Solid Earth*, 93(B2), pp.1159-1173.
- Viebahn, P., Vallentin, D. and Höller, S., 2014. Prospects of carbon capture and storage (CCS) in India's power sector – an integrated assessment. *Applied energy*, 117, pp.62-75.
- Viebahn, P., Vallentin, D. and Höller, S., 2015. Prospects of carbon capture and storage (CCS) in China's power sector – an integrated assessment. *Applied energy*, 157, pp.229-244.
- Walker, R.J., Holdsworth, R.E., Armitage, P.J. and Faulkner, D.R., 2013. Fault zone permeability structure evolution in basalts. *Geology*, 41(1), pp.59-62.
- Walker, R.J., Holdsworth, R.E., Imber, J., Faulkner, D.R. and Armitage, P.J., 2013. Fault zone architecture and fluid flow in interlayered basaltic volcanoclastic-crystalline sequences. *Journal of Structural Geology*, 51, pp.92-104.

## Bibliography

- Wang, F. and Giammar, D.E., 2013. Forsterite dissolution in saline water at elevated temperature and high CO<sub>2</sub> pressure. *Environmental science & technology*, 47(1), pp.168-173.
- Wells, R.K., Xiong, W., Giammar, D. and Skemer, P., 2017. Dissolution and surface roughening of Columbia River flood basalt at geologic carbon sequestration conditions. *Chemical Geology*, 467, pp.100-109.
- Wolff-Boenisch, D., Gislason, S.R. and Oelkers, E.H., 2006. The effect of crystallinity on dissolution rates and CO<sub>2</sub> consumption capacity of silicates. *Geochimica et Cosmochimica Acta*, 70(4), pp.858-870.
- Wu, H., Jayne, R.S. and Pollyea, R.M., 2018. A parametric analysis of capillary pressure effects during geologic carbon sequestration in a sandstone reservoir. *Greenhouse Gases: Science and Technology*, 8(6), pp.1039-1052.
- Xiong, W., Wells, R.K. and Giammar, D.E., 2017a. Carbon sequestration in olivine and basalt powder packed beds. *Environmental science & technology*, 51(4), pp.2105-2112.
- Xiong, W., Wells, R.K., Menefee, A.H., Skemer, P., Ellis, B.R. and Giammar, D.E., 2017b. CO<sub>2</sub> mineral trapping in fractured basalt. *International Journal of Greenhouse Gas Control*, 66, pp.204-217.
- Xu, T., Sonnenthal, E., Spycher, N. and Zheng, L., 2014. TOUGHREACT V3. 0-OMP reference manual: A parallel simulation program for non-isothermal multiphase geochemical reactive transport. Lawrence Berkeley National Laboratory, Berkeley, CA.
- Yang, Y.M., Dilmore, R., Mansoor, K., Carroll, S., Bromhal, G. and Small, M., 2017. Risk-based monitoring network design for geologic carbon storage sites. *Energy Procedia*, 114, pp.4345-4356.

Yu, S.Y., Akervoll, I., Torsaeter, O., Stensen, J.A., Kleppe, J. and Midtlyng, S.H., 1998. History matching gas injection processes with in-situ saturation measurements and process hysteresis. In: *SPE International Oil and Gas Conference and Exhibition in China*. Society of Petroleum Engineers.

Zhang, L., Dilmore, R., Namhata, A. and Bromhal, G., 2018. Feasibility of CO<sub>2</sub> migration detection using pressure and CO<sub>2</sub> saturation monitoring above an imperfect primary seal of a geologic CO<sub>2</sub> storage formation: a numerical investigation. *Computational Geosciences*, 22(3), pp.909-923.

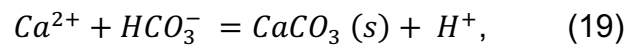
# Appendices

# Appendix A

## Mineral Precipitation

The dissolution of basalt is list in Equation 7. The precipitations of each alteration mineral are:

(1) calcite



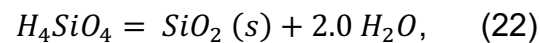
(2) magnesite



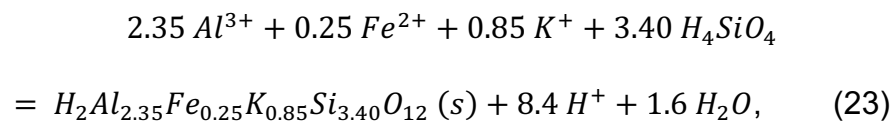
(3) siderite



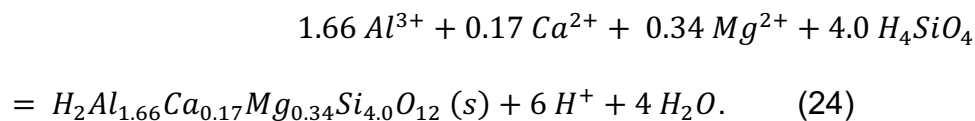
(4) Amorphous\_silica



(5) Illite(Fell)



(6) Montmorillonite (MgCa)



Appendix A

In Figure A1, it shows the volume fraction of magnesite, siderite, amorphous\_silica, and illite due to mineral precipitation.

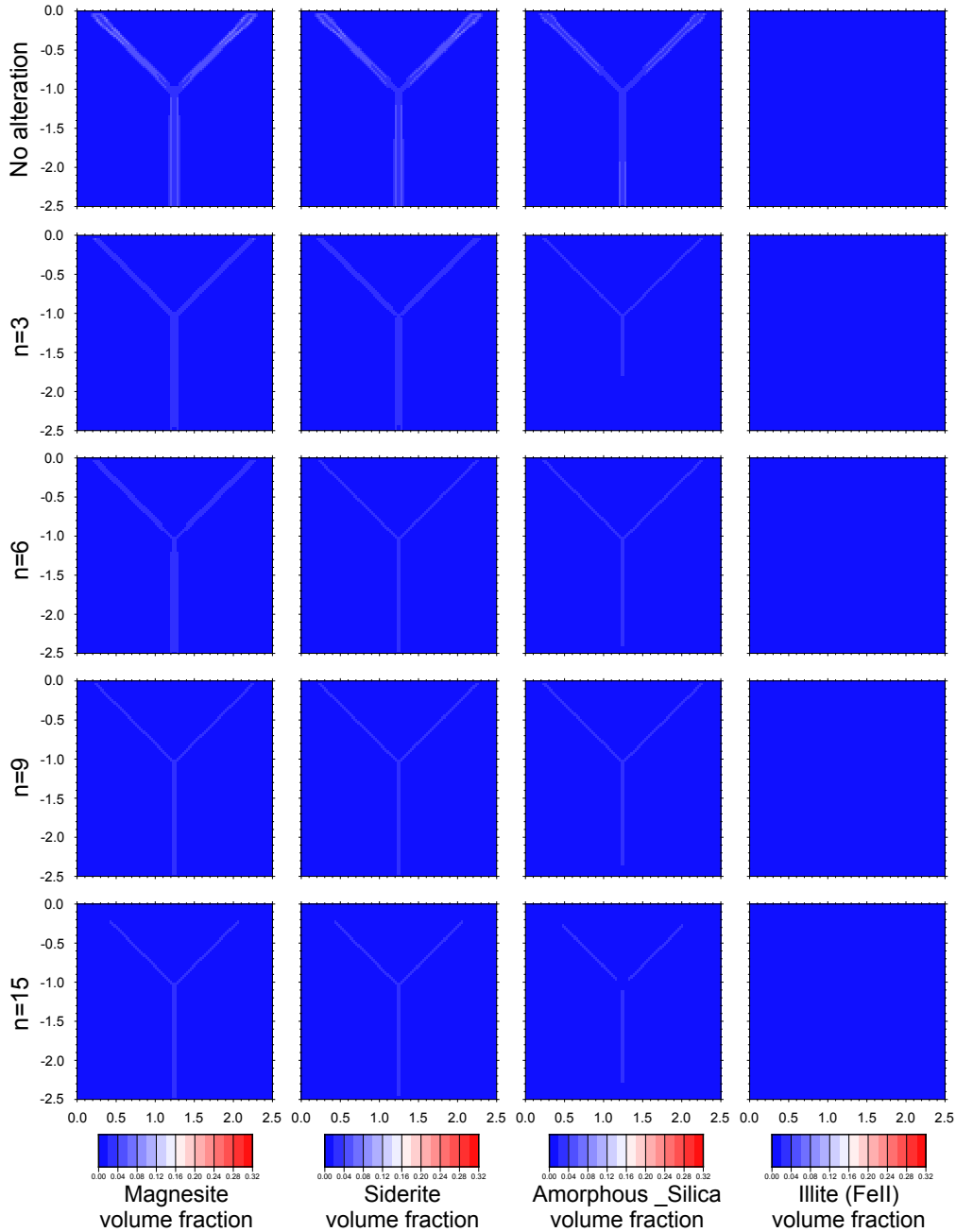


Figure A.1: Simulation results after 10 years of CO<sub>2</sub> leakage at 0.05 MPa overpressure. Columns from left to right show the volume fraction of magnesite, siderite, amorphous\_silica, and illite, respectively, that precipitate during the simulation. Each row corresponds with the strength of porosity-permeability coupling as described by the  $n$  exponent in Equation 12.

## Appendix B

### ANN Prediction for Testing Dataset

In Figures B1 and B2, prediction results analyses are shown of ten different parameter combinations of capillary pressure and relative permeability model for testing data set.

## Appendix B

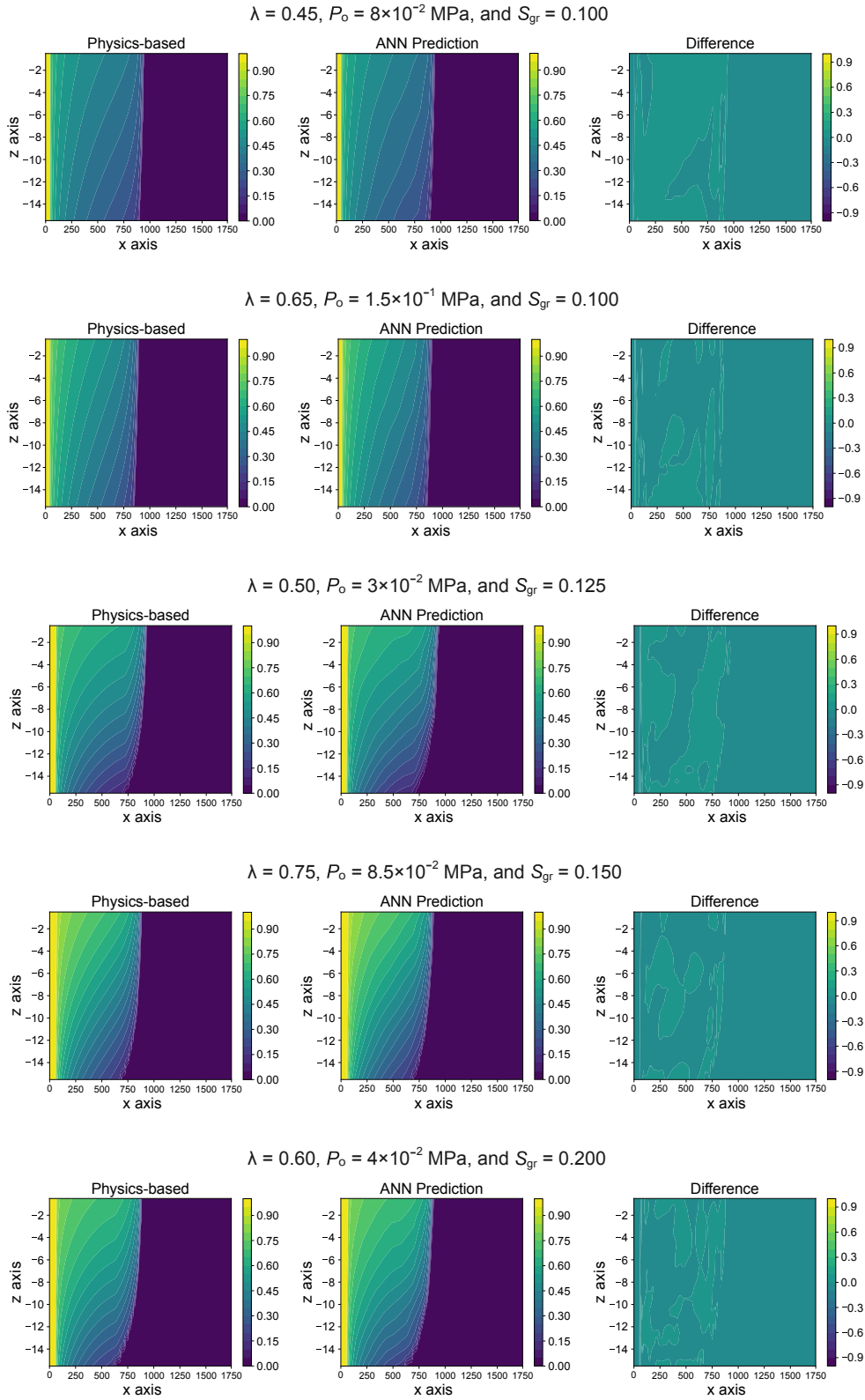


Figure B.1: Prediction results analyses of ten different parameter combinations of the machine learning model for CO<sub>2</sub> saturation. From left to right, the figures demonstrate the physics-based simulation results, ANN prediction results, and the difference between them.

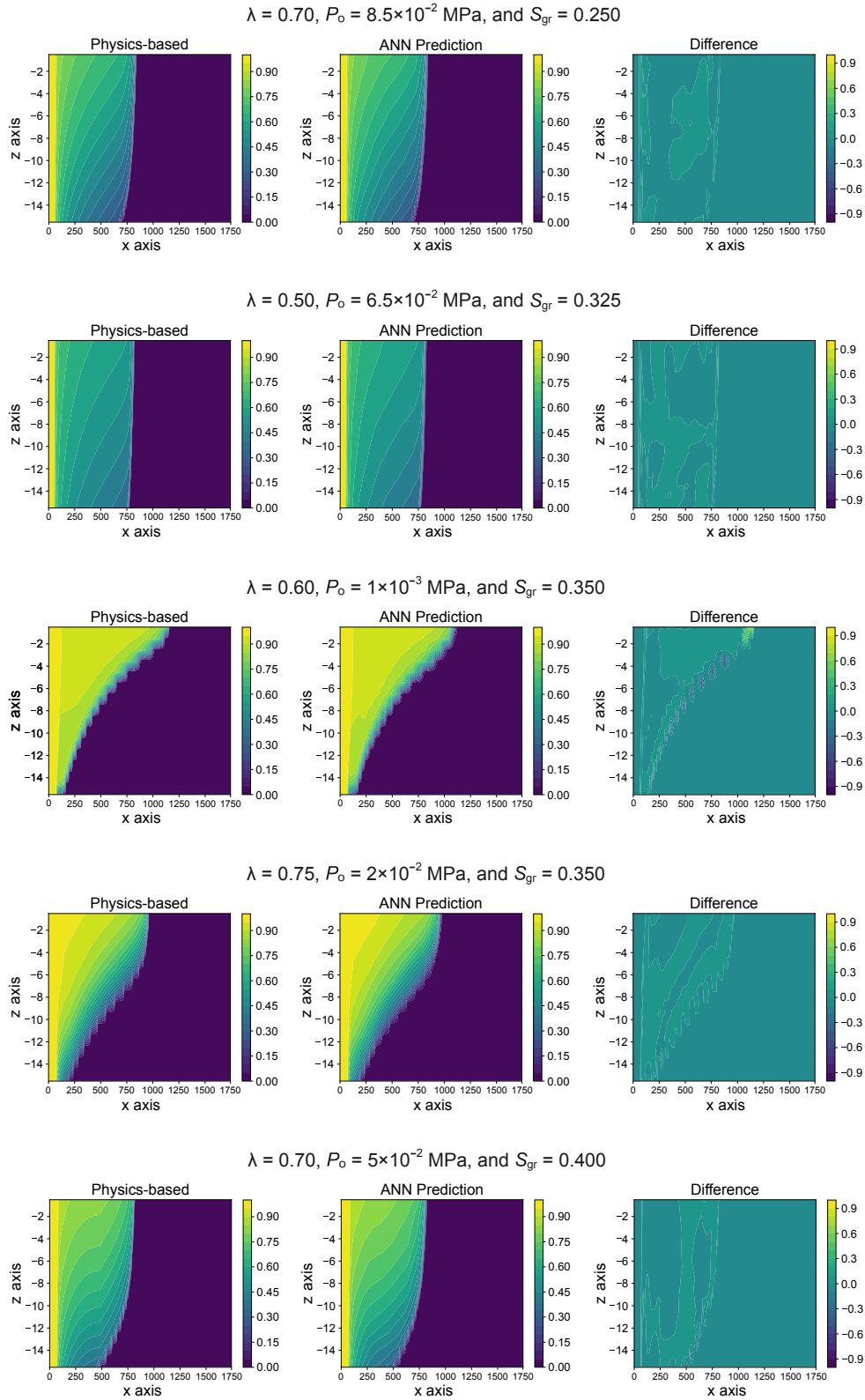


Figure B.1(continued): Prediction results analyses of ten different parameter combinations of the machine learning model for CO<sub>2</sub> saturation. From left to right, the figures demonstrate the physics-based simulation results, ANN prediction results, and the difference between them.

## Appendix B

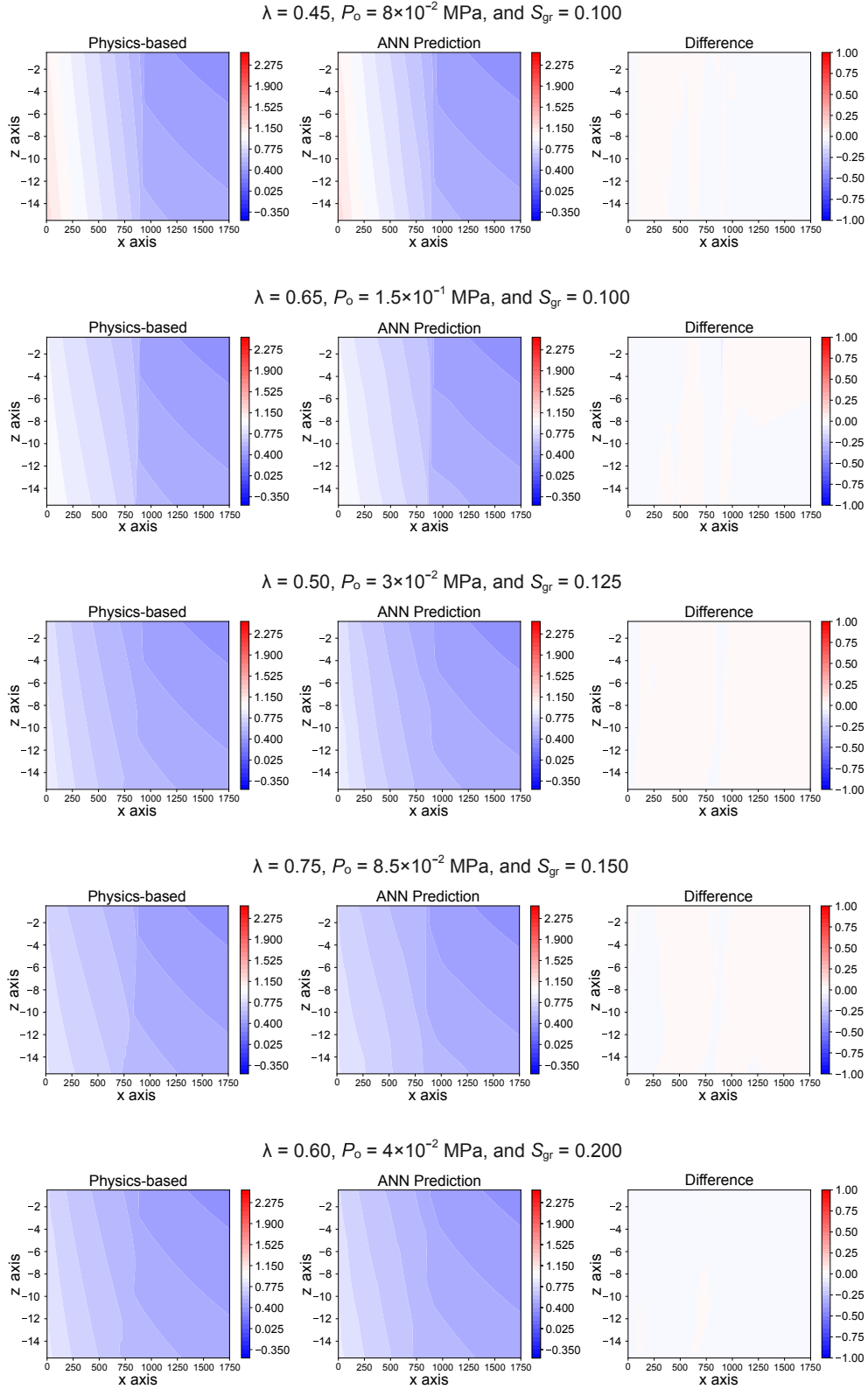


Figure B.2: Prediction results analyses of ten different parameter combinations of the machine learning model for pressure perturbation. From left to right, the figures demonstrate the physics-based simulation result, ANN prediction results, and the difference between them.

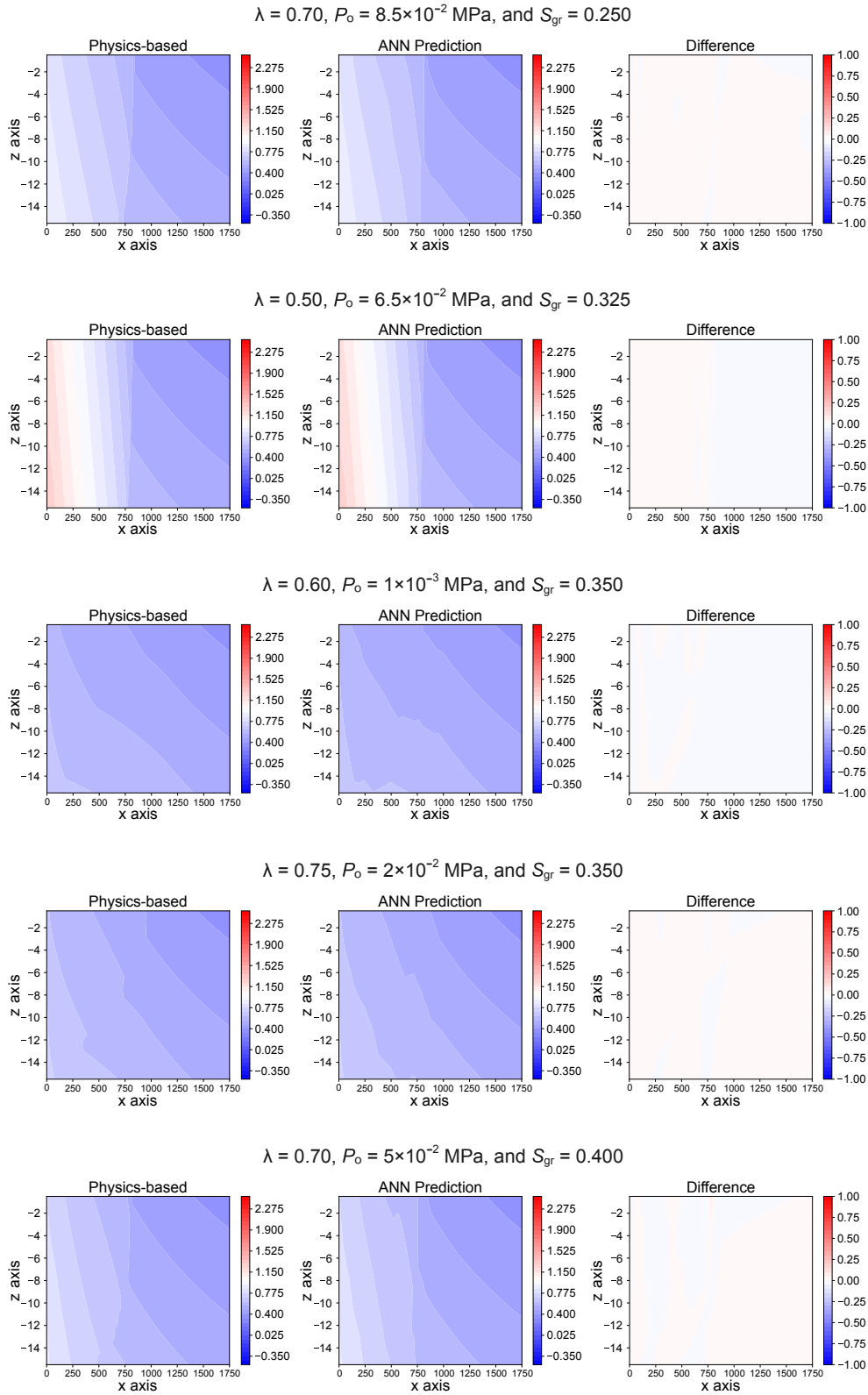


Figure B.2.(continued): Prediction results analyses of ten different parameter combinations of the machine learning model for pressure perturbation. From left to right, the figures demonstrate the physics-based simulation result, ANN prediction results, and the difference between them.